UNIVERSITY OF QUÉBEC AT CHICOUTIMI

A THESIS SUBMITTED TO

THE UNIVERSITY OF QUÉBEC AT CHICOUTIMI

IN PARTIAL FULFILMENT OF THE REQUIREMENTS

FOR THE DEGREE OF DOCTOR OF PHILOSOPHY

IN ENGINEERING

BY

YADIAN XIE

STUDY ON HIGH-PURITY ALUMINA PREPARATION AND ITS APPLICATIONS

JUNE 2017

UNIVERSITÉ DU QUÉBEC À CHICOUTIMI

THÈSE PRÉSENTÉE À

L'UNIVERSITÉ DU QUÉBEC À CHICOUTIMI

COMME EXIGENCE PARTIELLE

DU DOCTORAT EN INGÉNIERIE

PAR

YADIAN XIE

ÉTUDE SUR LA PRÉPARATION DE L'ALUMINE DE HAUTE PURETÉ ET SES APPLICATIONS

JUIN 2017

ABSTRACT

Wastewater from different aluminum processing plants contains different surface treatment liquids. These liquids are strictly prohibited from being discharged directly into the environment due to their high acidity. Different factories and enterprises add water to dilute them or neutralize them with alkali. These approaches not only cause a part of the aluminum ions being discharged, but also result in the release of a large number of harmful metal ions and heavy metal ions. In such cases, a large amount of water and alkali are consumed; at the same time, surface water, groundwater and soil become polluted by a large volume of wastewater and different metal ions.

The main objectives of the project are: 1) to extract ultra-pure aluminum ions from wastewater and to study the effect of different parameters on the efficiency of the process; 2) to produce ultra-pure nano-alumina from wastewater using an organic template and to study the effect of different parameters on the particle size distribution as well as on the morphology of the nanoparticles; 3) to explore the possibility of different applications for different types of alumina particles.

In this work, aluminum was extracted from the wastewater in the form of alum. This aluminum alum solution was later used to produce 99.999% pure (5N) nano-alumina particles. Two different methods, namely single and double template methods, were used to control the size and the nature of the alumina particles.

A single template method was used to produce 99.999% pure (5N) spherical alumina nanoparticles. The aluminum alum solution was hydrolyzed to produce boehmite which was used to produce the spherical alumina nanoparticles. Gum arabic and urea were used to produce the single template. These alumina nanoparticles were converted to alpha (α) form by heating. Then, the α-alumina particles were used to produce sapphire crystals.

An evaporation-induced synthesis approach with double template was used to produce spherical mesoporous nanoparticles of uniform size distribution. These particles were used for the photoacoustic tomography.

The originality of the project lies in the utilization of new sources of raw materials (wastewater from industries) and using chelating polymers as well as additives to develop a novel and environment friendly high purity alumina (HPA) production method. In addition, the alumina particle size and its distribution are controlled precisely, which is difficult to achieve with other alumina production methods.

RÉSUMÉ

Les eaux usées provenant des différentes usines de traitement de l'aluminium contiennent de différents liquides de traitement de surface. Ces liquides sont strictement interdits d'être déchargés directement à l'environnement en raison de leur forte acidité. Des différentes usines et entreprises ajoutent de l'eau pour les diluer ou les neutralisent avec l'alcali. Ces traitements provoquent non seulement la décharge d'une partie des ions d'aluminium, mais également la libération d'un grand nombre d'ions métalliques nocifs et d'ions de métaux lourds. Dans ces cas, des grandes quantités de l'eau et de l'alcali sont consommées; en même temps, les eaux de surface, les eaux souterraines et le sol sont pollués par un grand volume d'eaux usées et de différents ions métalliques.

Les objectifs principaux du projet sont : 1) d'extraire les ions d’aluminium ultra-purs des eaux usées et d'étudier l'effet de différents paramètres sur l'efficacité du procédé; 2) de produire la nano-alumine ultra-pure à partir des eaux usées en utilisant un modèle organique et d’étudier l'effet de différents paramètres sur la distribution granulométrique et la morphologie des nanoparticules; 3) d’explorer différentes applications des différents types des particules d'alumine.

Dans ce travail, l'aluminium a été extrait des eaux usées sous forme d'alun en utilisant un modèle simple. Cette solution d'alun a ensuite été utilisée pour produire des particules de nano-alumine pur à 99,999% (5N). La solution d'alun a été hydrolysée pour produire une bohémite qui a également été utilisée pour produire des nanoparticules d’alumine sphérique

pure à 99,999% (5N). Ces microparticules d'alumine ont été utilisées pour produire des cristaux de saphir.

Une approche basée sur la séparation induite par évaporation à double modèle a été utilisée pour produire des nanoparticules mésoporeuses sphériques avec une distribution de taille uniforme. Ces particules ont été utilisées pour la tomographie photoacoustique.

L’originalité du projet est l’utilisation de nouvelles sources des matières premières (l’eau usée des industries) et des polymères chélatants et des additives afin de développer une nouvelle méthode écologique pour la production de l’alumine de haute pureté. De plus, la taille des particules de l’alumine et sa granulométrie sont contrôlées précisément, ce qui est difficile à atteindre avec d’autres méthodes de la production de l’alumine.

ACKNOWLEDGEMENTS

This research would not have been possible without the guidance of my thesis director, Prof. Duygu Kocaefe, co-director Prof. Yasar Kocaefe, and Prof. Wei Liu. I would like to express my deepest respect and gratitude for their scientific guidance, their trust and support all along the path.

Many thanks to Prof. Dipankar Bhattacharyay for his insight, scientific discussions, and time. I especially thank Mr. Pascal Vandal, Mr. Patrice Paquette, and Mr. Dany Racine in Canada, and Mr. Lei Li, Mr. Gonglei Zhang, and Mr. Xin Nie in China for their assistance with the equipment handling, sample preparation, and data analysis.

Thanks also to all my friends I met in Chicoutimi for their encouragement and support. I would like to express my warm wishes to my parents and my whole family for their unending love and trust throughout my education. Finally, this thesis is dedicated to Yuanyuan Sun and Maple Xie for putting up with me and standing by my side all the time.

This research was supported by the University Research Centre on Aluminum (CURAL) of the University of Québec at Chicoutimi (UQAC), the Guizhou Normal University (GNU), and HTOT Optoelectronics Technology Cooperation and National Centre for Nano-Science and Technology.

TABLE OF CONTENTS

LIST OF FIGURES

LIST OF TABLES

LIST OF APPENDICES

Chapter 1

Introduction

1.1 Background

The surface of different products made of aluminum and aluminum alloys is treated to improve appearance, durability, and adhesion properties. The surface treatment includes numerous physical and chemical processes. Physical surface treatments produce solid wastes and oil-bound suspensions. The chemical treatment results in large volumes of wastewater with high acidity. These liquids are strictly prohibited from being discharged directly into the environment. Different factories and enterprises add water to dilute them or neutralize them with alkali. These treatments result in the release of a large number of harmful metal ions and heavy metal ions. Thus, large amounts of water and alkali are consumed, at the same time, surface water, groundwater, and soil get polluted by a large volume of wastewater and different metal ions.

Shi and Xia [1] extracted aluminum ion (Al^{3+}) from aluminum foil treatment wastewater to prepare polyaluminum chloride (PAC), which can be used in other wastewater treatment plants as flocculants. However, he could not address the issue of the presence of other metal cations such as calcium, iron, copper, sodium or even heavy metal cations. These impurities continue to exist in the flocculants and may cause secondary pollution.

In recent years, different methods have been developed to convert aluminum ion (Al^{3+}) in wastewater to a number of industrial products such as aluminum sulfate, aluminum carbonate, and polymeric ferric aluminum chloride. The intention is to do a resourceful recycling of the wastewater. The problem with these methods is that the products are mostly of low quality, and they are low value-added products. These products cannot be self-sufficient enough to support the cost of wastewater treatment; therefore, the recycling of wastewater cannot be effective and stable [2].

Some researchers proposed to treat wastewater by using ion exchange method such as the use of ion exchange resin for the recovery of aluminum ion (Al^{3+}). This method can partially remove the metal ions due the preferential adsorption of different ions by the ion exchange resin, but cannot completely purify the wastewater. Especially, the long adsorption time, unstable adsorption amounts, and the cost of ion exchange resin makes this choice economically unviable for the factories and the enterprises [3-6].

Ultra-high purity nano-alumina is a value-added product and has the advantages of high density, high melting point, high hardness, and good chemical stability. It is widely used in a variety of optical devices, window materials, and sapphire substrate materials in modern high-tech industries. Alumina powder is conventionally produced from the bauxite ore by the Bayer process. This process is simple, but requires extensive processing and consumes large amounts of energy. The purity of the alumina produced is around 98% - 99%. The particle size is usually bigger than 10 μm, and the particle size distribution is not uniform. Thus, the alumina produced by the Bayer process is mainly used for the

electrolytic production of primary aluminum. Based on the Bayer process, many methods have been developed. These methods include ammonium aluminum sulfate (aluminum alum), aluminum alkoxide, and flame sintering at high temperature. These methods require costly raw materials. The ammonium aluminum sulfate method needs high purity aluminum hydroxide; aluminum alkoxide method requires high purity aluminum block; high temperature sintering method utilizes high purity aluminum powder. At the same time, large amounts of harmful gases such as nitrogen oxides, sulfur monoxide, sulfur dioxide, hydrogen sulfide, and isopropanol, are released during the heat treatment of different chemicals. These methods generally have high raw material cost and can cause environmental pollution. Also, it is difficult to control the size of the alumina particles.

Alumina can be used in different high value-added products such as adsorbents [7], ceramics [8], catalysts and catalyst carriers [9], etc. These applications depend not only on the particle size, but also on the particle shape. Presently, the common shapes of aluminum oxide can be rod-like [10], fibrous [11], plate-like [12], spherical [13], etc. Seyed et al. [14] have successfully prepared γ-aluminum from kaolinite by the precipitation method combined with sulfuric acid leaching, and high temperature calcination. The alumina particles were large and the morphology was irregular. The particle sizes were between 0.5 μm and 0.9 μm. Dabbagh *et al.* [15] and Feng *et al.* [16] prepared rod-like, fibrous, and spherical alumina particles by using a single template method and separating nucleation and aging steps (SNAS). The morphology of the alumina particles was mostly irregular. The dispersibility of the alumina particles were poor, the processes were complex, costly, and hard to control. Lv *et al.* [17] prepared spherical alumina with high thermal stability,

high sphericity, and uniform particle size distribution by dropping a boehmite sol in an oil-ammonia column. The boehmite sol was the source of aluminum. However, the particle size of the prepared product was large, which limits its application area. Wu *et al.* [18] used aluminum isopropoxide precursor and polyethylene glycol - polypropelene glycol - polyethylene glycol (P123) block-copolymer template and synthesized organized mesoporous alumina with hierarchical structure.

Mesoporous materials have the characteristics of high specific surface area, organized pore structure, narrow pore size distribution, and continuous pore size; therefore, they play an important role in adsorption and separation, especially in catalytic reactions [19]. The spherical alumina has high fluidity, which means it does not easily agglomerate, and will enhance the catalytic activity [20]. The nano-scale spherical mesoporous alumina can improve its application in adsorption, separation and catalytic reactions.

Another important application of alumina is the production of sapphire crystals. Advances are made in the development of sapphire crystals in recent years because of its excellent optical, chemical, and other properties. It is the most common LED (Light-Emitting Diode) substrate material. In the global market of LED substrate, two-inch sapphire wafers are widely used. The heat exchange method is a crystal growth technique used for the production of large sapphires. In 1970, Schmid and Viechnicki [21] first grew sapphire crystals using the heat exchange method. A heat exchanger was used to remove heat, causing a longitudinal temperature gradient that is cold at the bottom and warm at the top of the crystal growth area. The temperature gradient was controlled by regulating the

rate of gas flow in the heat exchanger (helium gas) as well as the heating power. The pressed alumina blocks were melted in a crucible at around 2100 ºC, and the sapphire crystals were slowly solidified by cooling with a flow of helium gas. The heat exchange method requires high-quality raw materials in order to have a stable temperature field during the crystal growth process. The segregation coefficient of the impurities in the melted crystal is set to less than 1. Impurities are therefore continuously discharged into the melted crystal from the solid-liquid interface and distributed to the outer layer of the surface where the crystals and the crucible wall come in contact [22-25].

In this work, aluminum has been extracted from the wastewater in the form of aluminum alum (in the rest of the text, alum refers to the aluminum alum). This alum solution was later used to produce 99.999% pure (5N) nano-alumina particles. The alum solution was hydrolyzed to produce boehmite which was also used to produce 99.999% pure (5N) spherical alumina nanoparticles by the single template method. These alumina nanoparticles were used to produce sapphire crystal.

An evaporation-induced synthesis approach with double template was used to produce the spherical mesoporous nanoparticles of uniform size distribution. These particles were used for the photoacoustic tomography.

1.2 Statement of the Problem

It is important for the industry to develop methods to extract high purity alumina from wastewater produced by the chemical treatment of aluminum surfaces. The chemical

surface treatment methods conventionally used in the aluminum industry include chemical etching, electrochemical etching, chemical milling, dyeing, anodizing, etc. In these processes, large amounts of acids (such as sulfuric acid) are used. These surface treatment methods produce large volumes of wastewater with low pH. This type of wastewater also contains different metal ions. Depending on the purity and particle size, the alumina particles can be used in different fields. It is important to have a small average alumina particle size and a narrow particle size distribution in the range of 20 to 200 nm in order to control the quality (homogeneity) of the final product. It is necessary to explore different applications of alumina particles. The industry needs to find value-added products as well as novel applications which can increase the return and reduce environmental pollution.

1.3 Objectives

The main objectives of this study are:

1. to extract ultra-pure aluminum ions from wastewater and to study the effect of different parameters on the efficiency of the process.

2. to produce ultra-pure nano-alumina from wastewater using an organic template and to study the effect of different parameters on the particle size distribution and the morphology of nanoparticles.

3. to explore different applications of the different types of alumina particles.

1.4 Originality

1. Considering the increasing demand of high purity alumina (HPA) and the high cost, the novelty of this project is to test new sources of raw materials (wastewater from industries) and to develop a novel HPA production process. Nowadays, high purity raw materials are used to produce HPA. This project valorizes a wastewater effluent and not much research has taken place on the use of wastewater as raw material for HPA.

2. Most of the existing HPA production processes (such as the Bayer process, the use of alum, etc.) are not environment-friendly because of the emissions of harmful gases and wastes. The novelty of the current project lies in the production of good quality HPA from industrial wastes in an environment-friendly way.

3. Use of chelating polymers and additives has not been studied in detail in the production of HPA. Chelating compounds were used to reduce the trace element content in HPA during this study.

4. Presently, the commercial methods do not have enough control on the size distribution of HPA produced. In this project, methods were developed to produce not only HPA, but also to control the particle size and its distribution. The effect of pH, dilution of raw materials, rate of addition of reagents, heating conditions, etc. on the quality of HPA has not yet been studied systematically.

1.5 Methodology

Different wastewater samples were analyzed for aluminum and other metal ions and anions by ICP-OES, titration and liquid chromatography. The reagents used in this work were treated to improve their purity. The wastewater was treated with different chelate compounds under controlled pH conditions to remove different impurities. The effect of different parameters on the removal efficiency of the reagents was studied. Then, aluminum was extracted from the wastewater in the form of alum via the treatment with ammonia and sulfuric acid. This alum solution was later used to produce 99.999% pure (5N) nano-alumina particles. Two different methods, namely single and double template methods, were used to control the size and the nature of the alumina particles.

A single template method (using gum arabic and urea) was used to produce 99.999% pure (5N) spherical alumina nanoparticles. The template was removed by heating at 600ºC. These alumina nanoparticles were converted to alpha (α) form by heating at high temperature (1800ºC). Then, α-alumina particles were used to produce sapphire crystals.

An evaporation-induced synthesis approach with double template (using gum arabic, P-123, and urea) was used to produce spherical mesoporous nanoparticles with uniform size distribution. The particles were heated to 600ºC to remove the template. These particles were used for photoacoustic tomography.

1.6 Scope

In this thesis, the production of ultra-pure nano-alumina particles from wastewater has been studied. Two different methods, namely single and double template methods, have been used to synthesize nano-alumina particles. These nanoparticles were calcined at different temperatures and used in sapphire production and photoacoustic tomography. This thesis contains seven chapters.

Chapter 1 is the introduction. It presents the background, statement of the problem, objectives, originality, general methodology and the scope of the thesis.

Chapter 2 gives a comprehensive literature review which focuses on different methods of nanoparticle synthesis.

Chapter 3 describes the methodology. This includes the characterization of wastewater and the treatment of reagents. This chapter also describes the application of the treated reagents to prepare high purity alum from wastewater. The alum solution was used to prepare nano-alumina particles which were finally used for sapphire production and photoacoustic tomography.

Chapter 4 describes the results related to the preparation of high purity alum solution from wastewater. This chapter also includes the treatment and the characterization of the reagents to identify the conditions suitable for the purification of reagents.

Chapter 5 gives a detailed description of the production of 5N (99.999% pure) spherical alumina nanoparticles by single templating. The results of the characterization of nanoparticles and the effect of different parameters on nanoparticles have been presented.

Chapter 6 describes the production of 5N (99.999% pure) spherical mesoporous alumina nanoparticles by double templating. The results of the characterization of mesoporous nanoparticles and the effect of different parameters on the nanoparticles have been presented.

Chapter 7 presents the advanced application of 5N alumina nanoparticles in different fields. It includes the use of spherical alumina for sapphire growth using the heat exchange method and the application of mesoporous alumina nanoparticles in the photoacoustic tomography.

Conclusions and recommendations of the work are given in Chapter 8. This is followed by a list of references and three appendices which present published articles and patents.

Chapter 2

Literature review

Different materials are essential for the social development. Generally, certain material structure and morphology are required for their applications in a specific field. Inorganic materials are an important branch of materials, which promote development of science and technology. Alumina is an inexpensive and widely used inorganic material. It has a complex structure and many crystalline polymorphic phases such as α-Al_2O_3, β-Al_2O_3, γ-Al_2O_3, δ-Al_2O_3, θ-Al_2O_3, η-Al_2O_3, κ-Al_2O_3, χ-Al_2O_3, ρ-Al_2O_3, etc. The phase transition temperatures are different for different precursors during their calcination as shown in Figure 2.1 [26].

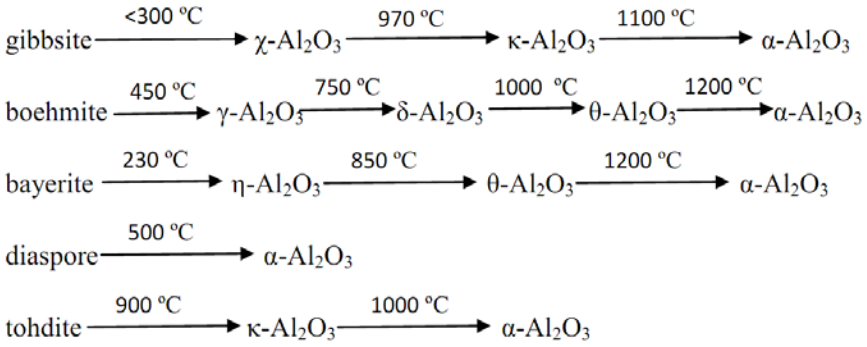

Figure 2.1: Phase transformation of alumina

The morphology, purity, surface acidity and hydrothermal stability, the pore structure and other properties restrict the application of alumina. The research is ongoing on the pore structure, surface acidity and hydrothermal stability [27]. Morphology, as one of the

important parameters of particle characterization, has a substantial effect on the properties and applications of the products. The morphology of particles is influenced and controlled by its crystallization habit during the preparation using liquid phase method [28, 29], which is restricted by the environment and the growth conditions.

There are some common liquid phase methods for synthesis of alumina, such as sol-gel method, hydrothermal method, template method, precipitation method, emulsion method or microemulsion method and electrolysis method, etc. Alumina with different morphologies can be obtained by using different synthesis methods and optimizing the reaction conditions.

2.1 Hydrothermal methods

Hydrothermal method is an approach where a solution of different species is poured into a sealed reactor and treated to produce a single crystal. Utilization of the relatively high temperature in the reactor and the high-pressure growth environment promotes the dissolution and recrystallization of poorly soluble or insoluble material. Hydrothermal methods include hydrothermal synthesis, hydrothermal treatment, hydrothermal reactions, etc. During the hydrothermal process, the crystal grows to its largest possible size under the non-restricted conditions and its characteristics (various shapes, high degree of crystallinity, small size, uniform distribution, less particle agglomeration, etc.) form [30, 31]. The development of crystal face and the morphology of the crystal formed by hydrothermal synthesis are closely related to the hydrothermal conditions such as water temperature, pressure and the permittivity, viscosity and diffusion coefficient of the solution, etc. The

same type of crystal can be produced with different morphology under different hydrothermal conditions [32].

Li *et al.* [33] mixed ammonium aluminum sulfate, dispersant PEG2000 and urea in deionized (DI) water and stirred them vigorously to form a solution. Then, the solution was poured into a stainless steel pressure reactor with a Teflon lining. By changing the temperature of the water, mesoporous alumina with different morphologies were obtained. In the course of the reaction, following reactions take place:

$$CO(NH_2)_2 + H_2O \longrightarrow CO_2 + 2NH_3 \quad (1)$$

$$NH_3 + H_2O \longrightarrow NH_4 + OH^- \quad (2)$$

$$Al^{3+} + 3OH^- \longrightarrow AlO(OH) + H_2O \quad (3)$$

As Figure 2.2 (a) shows, when the temperature is 90ºC, the particles obtained are spheres of different sizes. As it is shown in Figure 2.2 (b), at the temperature of 120ºC, the particles are superfine fiber-shaped. As Figure 2.2 (c) shows, massive fiber-shaped particles are obtained at the temperature of 150ºC. The crystal orientation is dependent on the temperature which affects the growth rate of the crystal face, consequently, the morphology can be controlled by regulating the temperature. These results indicate that the morphology of the particles substantially changes with the increasing water temperature.

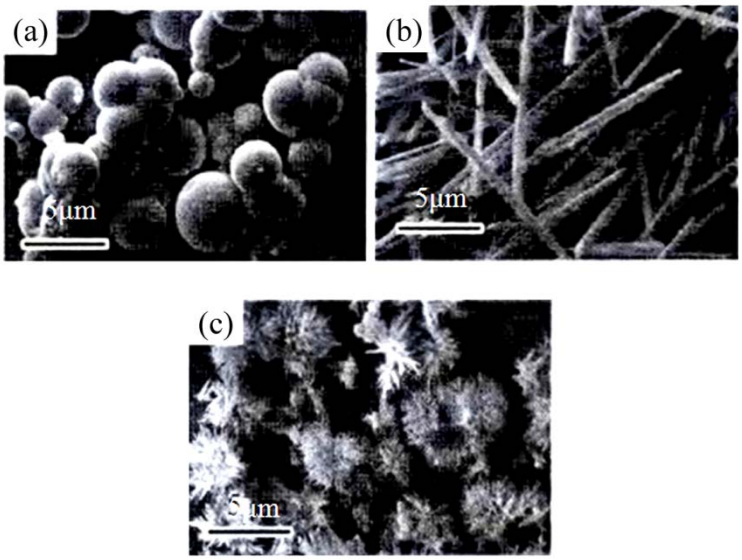

Figure 2.2: TEM images of alumina prepared under different temperatures.
(a) 90ºC, (b) 120ºC, (c) 150ºC [34]

Zhao *et al.* [34] prepared flat hexagonal-shaped nano-alumina by hydrothermal synthesis, using aluminum nitrate as aluminum source and sodium nitrate as additive. During the reaction, the Na^+ of sodium nitrate was adsorbed onto the alumina surface, which hindered the accumulation of Al^{3+} and OH^- ions. This affected the appearance of the particles. By changing the amount of sodium nitrate additive to control the growth of certain crystal face of alumina, hexagon-shaped alumina with different parameters was obtained. When the amount of sodium nitrate was 0.2 mol, the width of the particle was reduced and its length and thickness remained unchanged. When sodium nitrite was 0.4 mol and 0.6 mol, the thickness increased and the length and width remained unchanged. The hexagon-shaped particles were gradually transformed into thicker particles as the sodium nitrate concentration increased as shown in Figure 2.3.

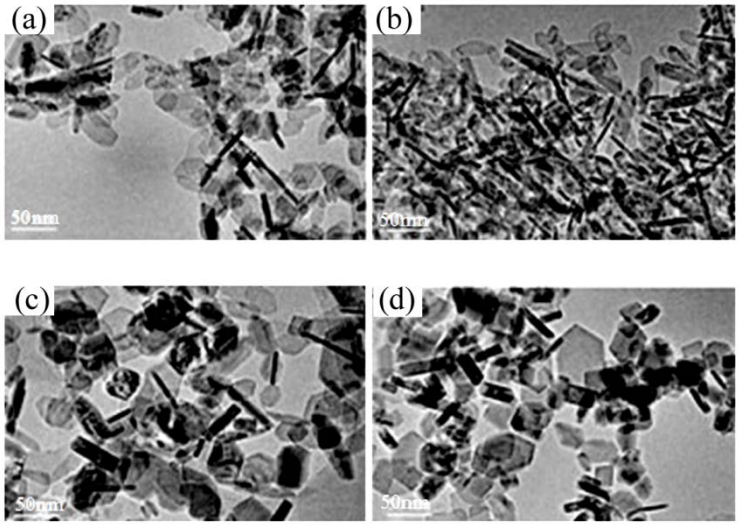

Figure 2.3: TEM images of nano-alumina with sodium nitrate concentration of (a) 0 mol, (b) 0.2 mol, (c) 0.4 mol, (d) 0.6 mol. [35]

Depending on different reaction systems, particles have accordingly different crystal habits. Pramod *et al.* and Shi *et al.* [36] synthesized needle-like and plate-like α-Al_2O_3, respectively, in water and alcohol-water reaction systems by hydrothermal treatment method using $Al(OH)_3$ colloid as precursor, as shown in Figure 2.4.

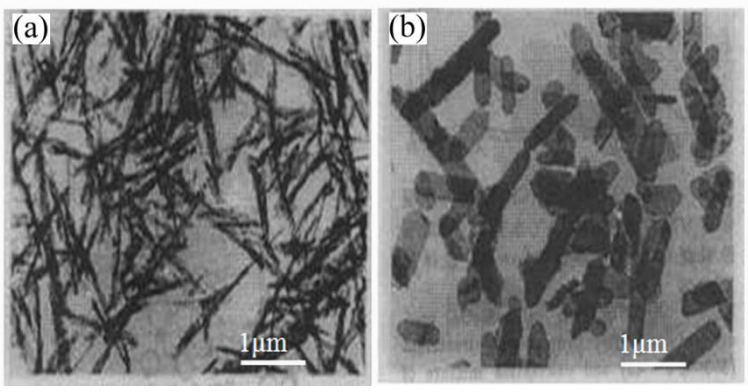

Figure 2.4: TEM images of α-Al_2O_3 (a) needle-like α-Al_2O_3, (b) plate-like α-Al_2O_3 [36-37]

Mikhailov *et al.* [38] prepared hexagonal flake-shaped γ-Al_2O_3 by hydrothermal method with $Al_2(SO_4)_3 \cdot 18H_2O$ and ammonia as raw materials. This study has shown that pH of solution has a significant impact on the morphology of precursor. Under acidic conditions, the H^+ in solution binds with the hydroxyl group, which is on the surface of the γ-AlO(OH) layered structure, thereby destroys this structure, eventually forms a rod-like nanostructure by rolling growth mechanism [39]. On the contrary, under alkaline conditions, it retains its layered structure, forming plate-shaped nanostructure. Figure 2.5 shows that when pH is 5, the product is rod-like; when pH is 7, the product is transformed from rod-like to plate-shaped nanostructure; when pH is 9, the product has hexagonal shape. Boehmite converts into a γ-Al_2O_3 during the firing process, but its shape and size do not change. Calcining the plate-like precursor at 600ºC for 4 hours, resulted in the original hexagonal γ-Al_2O_3 with basically same size.

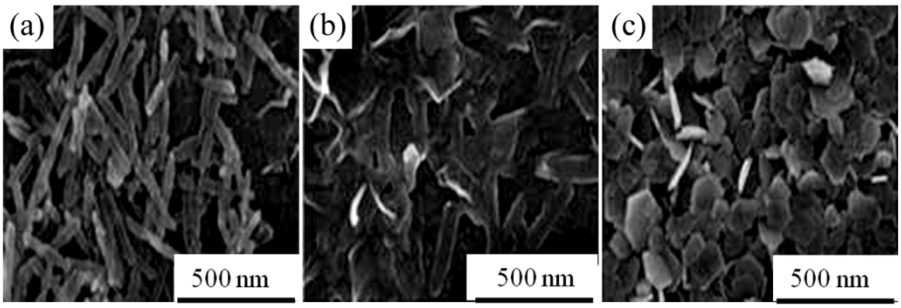

Figure 2.5: TEM images of γ-AlO(OH) prepared at (a) pH=5, (b) pH=7, (c) pH=9 [40-41]

2.2 Sol-gel method

The sol-gel method refers to inorganic or organic alkoxide dispersed in solution. Using the transparent sol formed by hydrolysis and condensation of the precursor, a gel with

certain structure is formed during the aging process by the aggregation of the gel particles. During the sol-gel process, the microstructure of the material is controlled and cut at the mesoscopic level by means of low temperature chemical method, which changes the morphology and structure of the particles [42, 43].

Ning *et al.* [44] using acetic acid (AcOH) as additive and adopting two-step alkoxide hydrolysis sol-gel method, synthesized spherical and fibrillar Al_2O_3 nano powder in organic phase. The results showed that the amount of AcOH has a decisive effect on the morphology of the particles. As the amount of AcOH increased with respect to aluminum isopropoxide [$Al(Opri)_3$], the shape of the particles gradually shifted from the fibrillar to the spherical shape, as shown in Figure 2.6. During the reaction, AcOH and other organic molecules containing functional groups N, O, S (ethylacetoacetate, polyamide, carboxylic acid salt) as additives coordinate with inorganic ion or are adsorbed onto the surface of crystal nucleus, which changes the growth rate of crystal face. This leads to the change in morphology of particles.

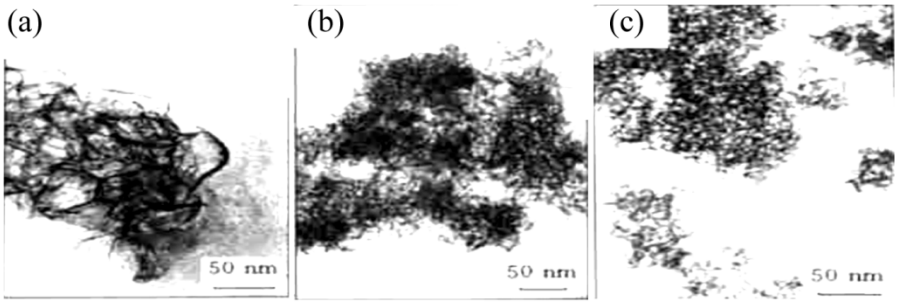

Figure 2.6: TEM images of alumina nanoparticles with different amount of AcOH
(a) No AcOH, (b) $m(AcOH)/m[Al(Opri)_3]<0.05$, (c) $m(AcOH)/m[Al(Opri)_3]\approx0.1$ [44]

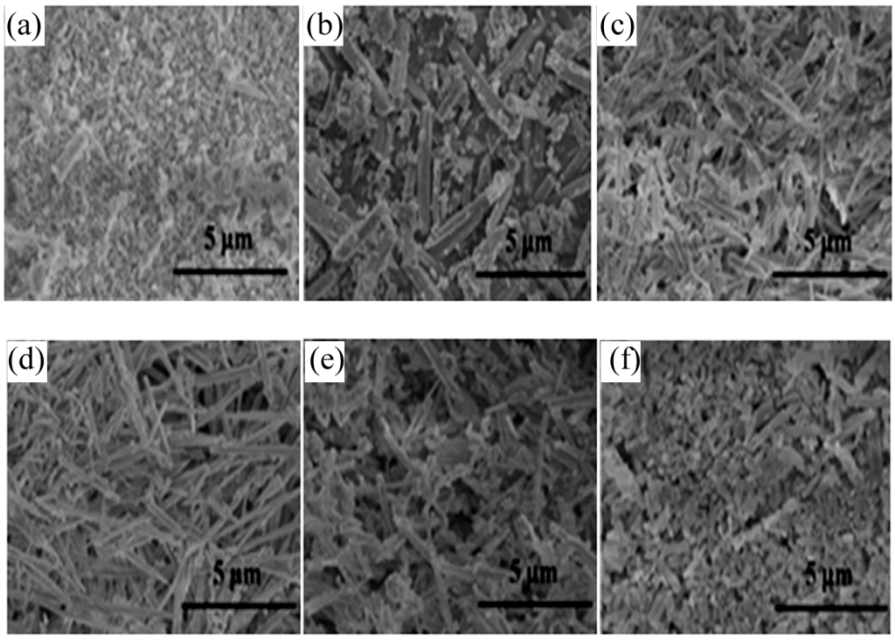

Figure 2.7: SEM images of alumina particles with different molar ratio of [Bmim] PF_6 and aluminum isopropoxide (a) Al_2O_3-0, (b) Al_2O_3-0.03, (c) Al_2O_3-0.12, (d) Al_2O_3-0.18, (e) Al_2O_3-0.24, (f) Al_2O_3-0.30 [45, 46]

Masouleh *et al.* and Ji *et al.* [45. 46] using aluminum isopropoxide [$Al(Opri)_3$] as aluminum source, [Bmim] PF6 (1-Butyl-3-methylimidazolium hexafluorophosphate) as ionic liquid and adopting sol-gel method to change the molar ratio of [Bmim] PF6 and aluminum isopropoxide, successfully synthesized uniform rod-like mesoporous γ-Al_2O_3. This study has shown that ionic liquid plays a very important role in the morphology of products. As it is shown in Figure 2.7, with the molar ratio of [Bmim] PF6, aluminum isopropoxide increases from 0 to 0.18, the morphology of the products has a highly homogeneous rod shape. When the molar ratio of [Bmim] PF6 and aluminum isopropoxide is 0.18, the morphology of the products with rod shape has the best homogeneity. If this ratio exceeds 0.18, it is not conducive enough to form the rod shape.

2.3 Template method

Template synthesis of nanomaterials is a cutting-edge technology developed since 1990s. It is also a very effective nanomaterials synthesis method that has been widely used in recent years. Early in 1999, South Korean scientists Kim *et al.* [47] took MCM-48 mesoporous silica as template and synthesized three-dimensional cubic mesoporous carbon CMK-1. In the same year, Japanese scientists Moriguchi *et al.* [48] used a cationic surfactant CTAB as template and synthesized disordered carbon materials by using phenolic resin as carbon source. Template method is not sensitive regarding the preparation conditions, easy to operate and implement, which controls the structure, morphology and particle size of nanomaterials through the template material (template). Template method is often divided into hard and soft template methods. Dong *et al.* [49] from Fudan University adopted hard template method. Through using mesoporous carbon pellets as a template, they have synthesized a variety of non-silicon-based mesoporous materials such as solid or hollow aluminum oxide, titanium oxide and aluminum phosphate microspheres. Firouzi *et al.* [50] and Huo *et al.* [51] from University of California used soft template method to explore a variety of different types of inorganic and organic combinations and proposed the general synthetic route to mesoporous materials.

Morphology is an important parameter for characterization of material properties, especially in the mesoporous material. Morphology, together with particle size, surface area, pore structure determines the property of mesoporous materials, consequently, pinpoints their applications [52, 53]. Among these, mesoporous thin films, as film-like material, have

an unparalleled advantage in adsorption and separation compared to the other nanomaterials with different shapes [54, 55].

The template method changes the morphology of products, mainly, by controlling the crystal nucleation and growth during nanomaterial preparation. Route of nanomaterial synthesis by using the template method is generally divided into three steps: First, the template is prepared. Second, some common synthetic approach such as hydrothermal method, precipitation and sol-gel method is used to synthesize the target product using the template. Finally, third step is the template removal. The choice of template for nanomaterial preparation is critical. Templates usually can be grouped in two major categories: natural substances (nanomineral, biological molecules, cells and tissues, etc.) and synthetic materials (surface active agents, porous materials and nanoparticles, etc.). In addition, the templates are generally divided into two groups (hard template and soft template) based on the difference in the template structure [56, 57].

Template removal is the last step in the synthesis of nanomaterials. The appropriate method of removal has to be chosen such that the physical and chemical properties of the product should not be affected. Common removal methods include physical and chemical methods, such as dissolution, sintering, etching, etc. The morphology of the nanomaterials can be controlled using different hard and soft templates.

2.3.1 Hard template

Hard template is a rigid material, whose stable structure directly determines the size and morphology of sample particle. A wide choice of hard templates is available, such as polymer microspheres, porous membrane, plastic foam, ion exchange resin, carbon fiber and porous anodic aluminum oxide (AAO), etc. [58, 59]. Because of their special structures and effect on particle size restriction, they play an important role in many fields.

a) Porous anodic aluminum oxide (AAO)

Porous anodic alumina has high pore density. The pores are evenly distributed and very thin. The pore size is adjustable in range of 50-200 nm and the pore density is between 1×10^{9} and 1×10^{12} cm^{-2} [60, 61]. It is widely used in the preparation of nano functional devices. For example, it is used in the deposition of metal, semiconductor, conductive polymer and other functional materials and has been successfully applied in fields of magnetic recording materials, optoelectronic components, electronics, etc. [62-69].

The preparation process of AAO has not been unified. Usually the high purity aluminum piece is placed into an acidic solution, and AAO is obtained by electrolysis by the anodic oxidation. By changing anode voltage and the composition, and concentration of electrolyte, the size and distribution of the pores are controlled. The structure diagram of AAO is shown in Figure 2.8. It can be seen from this figure that there is a dense alumina called the barrier layer between the non-oxidized aluminum matrix composite and the porous layer. Since the barrier layer hinders the contact between the electrolyte solution and

the electrode, this layer needs to be removed during the preparation of the sample by electrodeposition. The aluminum matrix composite also have to be removed in order to obtain the double pass AAO template.

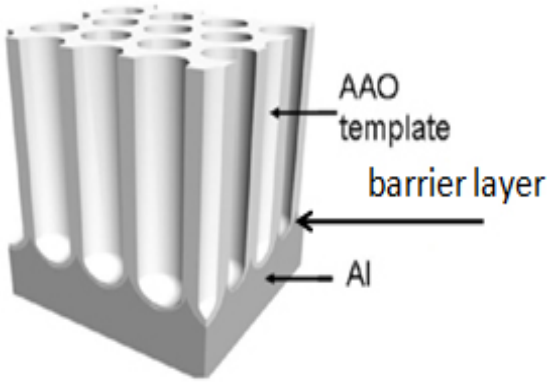

Figure 2.8: Structure diagram of AAO [70]

Porous anodic alumina is widely used in the preparation of nanomaterials because of the adjustability and quantum level of pore size, such as in the preparation of one-dimensional nanomaterials (nanowires, nanotubes), zero-dimensional materials (nanodots), mesoporous films, etc. The method of preparing nanomaterials by using porous anodic aluminum oxide as template is divided into two groups: one, electrochemical deposition; two, deposition without electrolysis. The precursor is deposited in the inner hole of the AAO template, and it controls the structure of the nanomaterial by guiding the spatial restriction of the cylindrical bore arranged in matrix. The morphology of the particle obtained during the present work is similar to that of the AAO template. Sun *et al.* [71] used AAO as the template and the electrochemical deposition method to prepare the ZnS nanowires with a diameter of 30 nm, as shown in Figure 2.9 (a). Lu *et al.* [72] synthesized

rod-like mesoporous silica by using polypropylene glycol and P123 as surfactant, silica as precursor in the AAO template, which is shown in Figure 2.9 (b). Forrer *et al.* [73] prepared gold nanowire arrays by using AAO template technique. The synthetic process schematically demonstrate how the AAO template produce gold nanowires which is given in Figure 2.9. Figure 2.10 (a) shows an AAO template with subsequent pores and Figure 2.10 (b) shows gold nanoparticles which were deposited in the pores by applying the AAO template potential in a gold bath. Figure 2.10 (c) shows that when the alumina and the aluminum base metal were removed with a NaOH solution, a free standing array of nanowires were exposed.

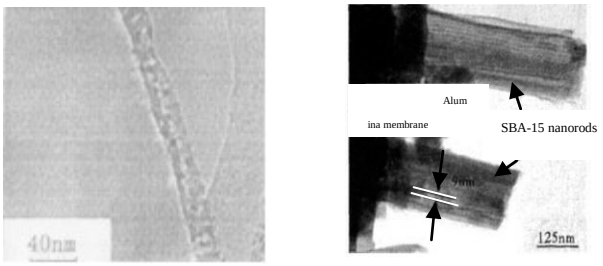

(a) (b)

Figure 2.9: TEM images of productions using fabricated by AAO template.
(a) ZnS nanowires, (b) rod-like silica [72]

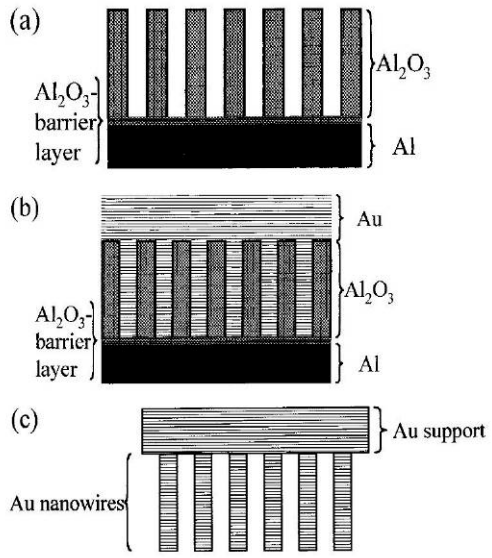

Figure 2.10: Synthesis of gold nanowires using porous aluminum oxide membrane template [73]

b) Mesoporous carbon

Mesoporous carbon is an important member of mesoporous materials. Its pore distribution is uniform and the pore diameter is generally between 2 nm and 50 nm. It has regular pore structure and high specific surface area. It is also thermally and chemically stable. Mesoporous carbon materials are widely used in many fields such as hydrogen storage, adsorption, catalysis, batteries, capacitors, etc. [74-80].

Synthesis methods of mesoporous carbon can be divided into catalytic activation, organic sol-gel method and template method, etc. Catalytic activation is used to synthesize mesoporous carbon through the catalytic effect of metals and their compounds, which act on carbon gasification [81, 82]. The activation reaction mainly occurs around the metal particles, which can inhibit the formation of micropores and increase the mesopores [83].

Organic sol-gel method was proposed by Pekala and Schaefer [84]. This method uses the gel formed by the polymerization of precursor as carbon source, and the mesoporous carbon is obtained by high-temperature carbonization. Rui *et al.* and Zhang *et al.* [85, 86] mixed melamine and formaldehyde with $NaCO_3$ as catalyst, and added mixed solution of phenol and formaldehyde, and finally phenolic resin to get organic moisture gel. Finally, mesoporous carbon is obtained by carbonization. The structure of mesoporous carbon is shown in Figure 2.11.

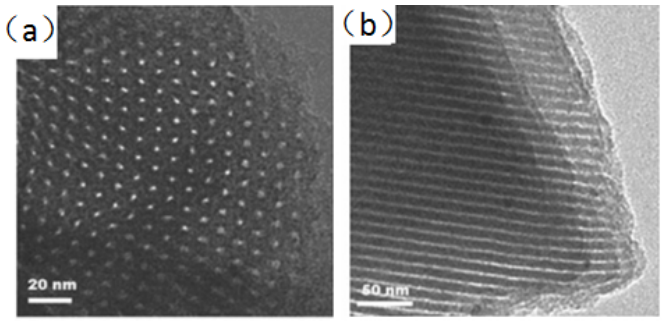

Figure 2.11: TEM images of mesoporous carbon structure (a) top view, (b) side view [87]

As the pore diameter of mesoporous carbon is even and the structure is ordered, it is often used as template to synthesize ordered mesoporous materials such as nano zeolite molecular sieve and mesoporous metal oxides, etc. In the synthesis of mesoporous materials, the mesoporous carbon pores are copied to a new mesoporous material by means of the nano replication technology, so the morphology and structure of the particles obtained by this method are similar to those of the mesoporous carbon. Roggenbuck and Tiemann [88], and Roggenbuck *et al.* [89] synthesized successfully the hexagonal ordered mesoporous MgO by using mesoporous carbon CMK-3 (manufactured by ACS Material,

Medford, MA) as the template, as shown in Figure 2.12 (a). Sakthivel *et al.* [90] used ordered mesoporous CMKs as the template to synthesize mesoporous zeolite molecular sieve. Yang *et al.* [91] synthesized the aluminosilicate molecular sieve RMM-1 with the cubic crystal system by CMK-1, which is shown in Figure 2.12 (b); aluminosilicate molecular sieve RMM-3 with the hexagonal crystal system by CMK-3, as shown in Figure 2.12 (c).

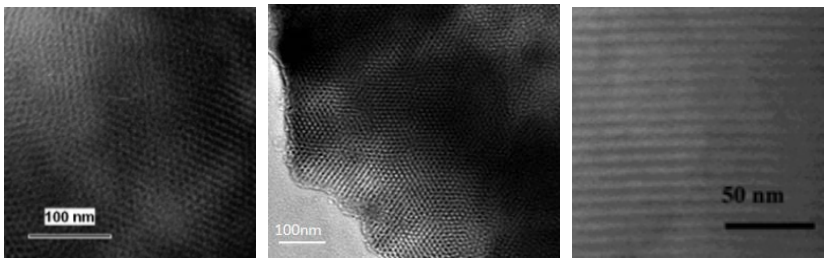

(a) (b) (c)

Figure 2.12: TEM images of particles prepared by CMKs-template (a) hexagonal mesoporous MgO, (b) RMM-1 with cubic crystal system, (c) RMM-3 with the hexagonal crystal system [91]

In the preparation of nanomaterials by using mesoporous carbon or other porous materials as the template, the precursor tends to crystallize inside the pores or deposit outside the pores. When the diameter of the pore is larger than that of the primary unit cell of the material, the space of the pore will accommodate the unit cell, forming a crystal material which has the similar structure as the pore. On the contrary, when the diameter of the pore is smaller than the primary unit cell unit, the crystal tends to form core and grow between the pores, and finally become irregular crystalline material.

c) Polymer microspheres

The methods of synthesizing polymer microspheres are methods such as emulsion polymerization, microemulsion polymerization, soap-free emulsion polymerization, suspension polymerization, dispersion polymerization, etc. By controlling the rate of polymerization, the particle size can be controlled. Zhang *et al.* [92] have studied the effects of various factors (such as dispersion stabilizer, monomer, initiator, reaction medium polarity, reaction temperature and agitation speed) on the particles, successfully synthesizing the polystyrene microspheres whose particle size is in the range of 1 μm to 10 μm.

The polymer microsphere has a good dispersivity and an easily adjustable particle size. It is usually used to synthesize the spherical-shaped particles or near-spherical core-shell and the hollow structure after modifying the surface of the particles. Lin *et al.* [93] synthesized the compound of PSA / ZnS / CdS core-shell structure by using homemade polystyrene - acrylic microspheres (PSA) as a template using the dip method. Then, the template PSA was removed with toluene solution, finally obtaining ZnS / CdS composite hollow microspheres, whose microsphere size can be regulated by the amount of emulsifier. Figure 2.13 shows the particle morphology during various preparation stages.

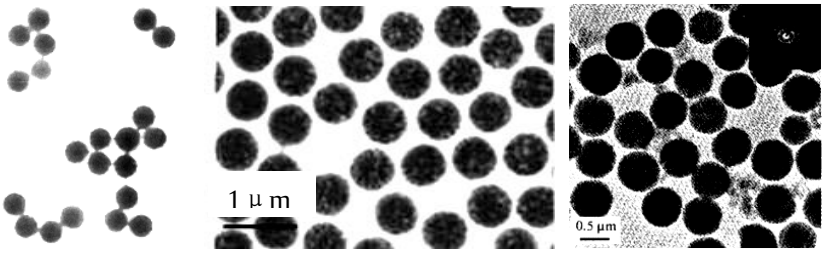

(a) (b) (c)

Figure 2.13: TEM images of ZnS/CdS composite hollow microspheres prepared by PSA (a) PSA, (b) PSA/ZnS/CdS, (c) ZnS/CdS

Hard template is a commonly used method for the synthesis of nanostructured materials such as nanoparticles, nanorods, nanowire, nanotubes, nanobelts and so on in recent years. Since the method is capable of preparing templates with different nano-hole size and structure under various requirements, using physical or chemical growth or deposition of nanomaterials in nanopores for nanomaterials fabrication, the dimensions and specifications of target production can be precisely controlled.

Because of the stability of hard template structure, it is often used as the "micro reactor" in synthesis, during which a precursor is filled into the pores of the hard template or absorbed at its surface by impregnation or chemical vapor deposition method. The special structure of the hard template restricts the crystallization or aggregation of the precursors, and a mesoscopic phase having a structure opposite to that of the template can be obtained with the removal of template material by the appropriate method. Particles with different morphologies can be obtained by choosing hard templates with different structures.

2.3.2 Soft template

The soft template does not have a fixed rigid structure. In the synthesis of nanoparticles, an aggregate with some certain structural features is formed by means of the intermolecular or intramolecular interaction force (hydrogen bonding, chemical bonding and static electricity). Inorganic species are deposited on the surface or the interior of these templates by means of electrochemical method, precipitation and other synthetic methods, forming particles with certain shape and size. Common soft template can be a surfactant, polymer and bio-polymer, etc. The soft template has broad prospects for development in the synthesis of nanomaterials because of its advantages such as its good repeatability, simplicity of the process and no requirement for the removal of silicon [94-98].

a) Surfactants

Surfactants are amphiphilic molecules, including ammonium salts, heterocyclic, carboxylic acid salts, sulfonate salts and other ionic or non-ionic surfactants. It is easy for the amphiphilic molecule groups to form a variety of ordered polymers in a solution, such as liquid crystals, vesicles, micelles, microemulsion, self-assembled film, etc. [99, 100].

From the perspective of material chemistry, it is generally thought that the interaction between liquid crystal phase of surfactants and organic - inorganic interface play a decisive role in the morphology of mesoporous materials [101, 102]. In the strongly acidic environment, the interaction between the organic - inorganic interface is weak hydrogen bonds, while in a strong alkaline environment, it is strong electrostatic attraction. Liquid

crystalline phases formed by surfactants in the solution have various structures, such as lamellar phase, cubic phase, hexagonal phase, etc. It is also easy to construct and adjust [103]. Therefore, it is an ideal reactor for synthesizing mesoporous materials. The lamellar, cubic, hexagonal structures are shown in Figure 2.14.

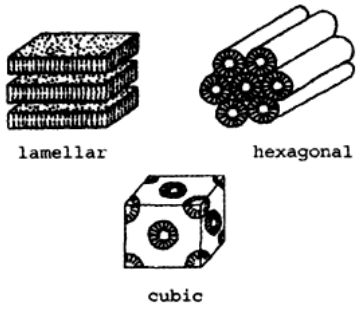

Figure 2.14: Structure of liquid crystals

It is relatively easy to control the hydrolysis and polymerization of silicon species. Moreover, mesoporous silica with fibrous, thin film, tubular, spherical and other different morphologies can be obtained by combining the collective effect of surfactants and the reaction environment. Zhang *et al.* [104] synthesized worm-like monodisperse mesoporous silica microspheres in neutral alcohol - water system by using laurylamine as surfactant, tetraethyl orthosilicate as silicon source. The silica microsphere is shown in Figure 2.15 (a). The pore diameter can be regulated and controlled by adjusting the molar ratio and the concentration of the reactants and the ratio of alcohol/water. Wang *et al.* [105] synthesized mesoporous silica thin film in an acidic environment, which is shown in Figure 2.15 (b),

using tetraethyl orthosilicate as silicon source, cationic surfactant cetyltrimethylammonium bromide as template.

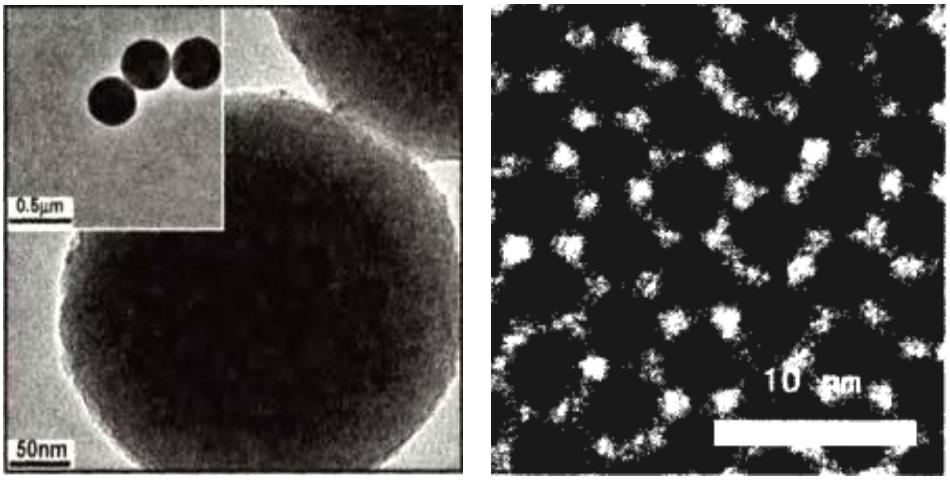

(a) (b)

Figure 2.15: TEM images of mesoporous silica (a) silica microsphere (b) mesoporous silica thin film [105]

b) High polymer

High polymer is often used as a template for the synthesis of mesoporous materials because of its large molecular weight, good stability and diversity of molecular structures. The pore structure and the morphology play a decisive role in the application of mesoporous materials. In recent years, researchers have emphasized the importance of controlling the morphology of mesoporous materials [106, 107], as different forms correspond to different application fields.

High polymer as a template and organic precursor form a certain liquid crystal structure by self-assembly method. In the fine crystal nucleation process, the selectivity of high polymers and certain crystal phase interact with each other, promoting or inhibiting the growth of crystal and thereby controlling and improving the morphology, size and distribution of particle. Li *et al.* [108] successfully synthesized cuprous oxide crystals, which is lamellar, urchin-like, one-dimensional line and acicular, in $CuSO_4$ and Na_2SO_3 system by using polyacrylamide (PAM) as template and adjusting the concentration of Cu^{2+}, PAM content and temperature. The lamellar, urchin-like and acicular cuprous oxides are shown in Figure 2.16.

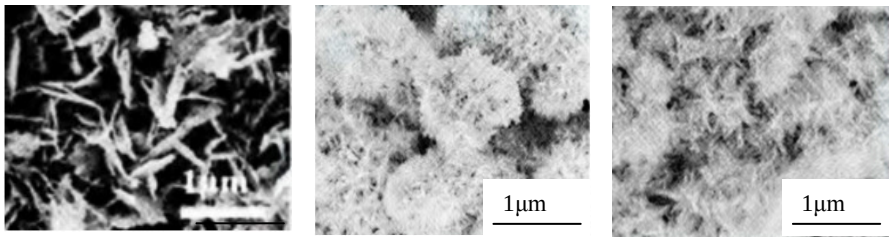

(a) (b) (c)

Figure 2.16: TEM images of cuprous oxide crystals (a) lamellar cuprous oxide crystal, (b) urchin-like cuprous oxide crystal, (c) acicular cuprous oxide crystal [108]

Block copolymer is one of the most important high polymers, which is connected by polymer chains with two or more different properties. During the process of synthesis of mesoporous materials, hydrogen bonding occurs as the hydrophilic segments and precursors interact with each other which results in the formation of the ordered mesoscopic phase. The pore diameter of the mesoscopic phase is determined by the

hydrophobic chain of the block copolymer. Therefore, the larger the molecular weight of hydrophobic segment is, the stronger the hydrophobic property is, and the larger the synthesized pore diameter is [109].

c) Biopolymer

Since biopolymer has the advantage of availability in wide variety of sources, its complex structure, non-toxicity and easy removal, etc., it has great potential to be used as a template in synthesis of other materials. By means of inducing the biomineralization of inorganic nanoparticles, biopolymer synthesizes nanomaterials can have certain structures.

Common biopolymers are DNA, proteins and polysaccharides, etc. Wang *et al.* [110] using linear DNA molecules of the same length as a template and controlling the synthesis of DNA sequences, synthesized petaloid and spherical gold nanoparticles. Zhang *et al.* [111] successfully synthesized hierarchical porous SnO_2 nanomaterials that have a structure of cotton fibers by using cotton as a template and respectively adopting solvothermal method, ultrasonic method and impregnation method.

Li and Zhao [112] schematically summarized two synthetic strategies of soft template method as shown in Figure 2.17. There are two common mechanisms of the soft template: inorganic species and surfactants directly have supramolecular self-assembly, forming organic-inorganic phase. The organic and the inorganic species can combine by electrostatic bonding, hydrogen bonding or covalent bonding. The interaction between

inorganic species and surfactants is weak. Hence it is necessary to add an intermediate phase as a link to connect them, forming a stable organic-inorganic phase.

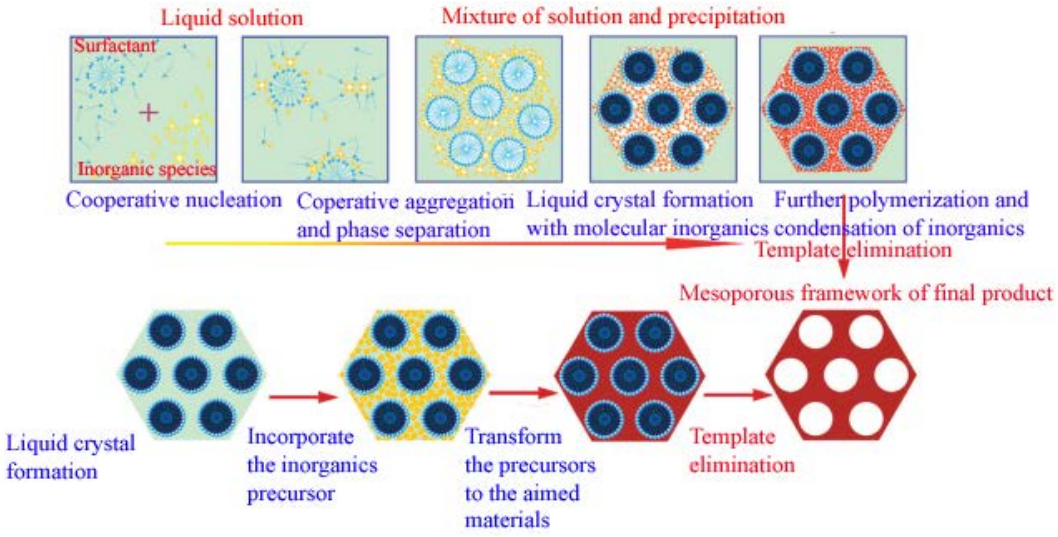

Figure 2.17: Mechanism of soft template method [112]

In the self-assembly process, inorganic species interact with surfactants driven by electrostatic force, covalent bond or hydrogen bond. The interaction of the organic (surfactants)/inorganic (inorganic species) interface is a weak hydrogen bond force in the strong acid environment while it is a strong electrostatic attraction force in the strong alkaline environment. Thus, inorganic species at the interface polymerize and crosslink, and assemble with surfactants [113, 114].

2.3.3 Comparison of hard and soft template

Hard template is mainly used for some previously prepared template material, such as AAO template, mesoporous carbon, polymer microsphere and so on. Hard template has

high reproducibility and stability, and it is mostly used for synthesis of arrays of nanomaterial. However, the separation of template and production may cause damage to the structure of nanotubes, nanowire or hollow balls.

On the other hand, soft template is mainly based on action of the micelle which form organic-inorganic phase between surfactant, high polymer and biopolymer, and target product. The aggregation by weak intermolecular or intramolecular interaction creates a certain structure of space. Such aggregates have significant structural interface. Soft template is formed during the reaction whereas hard template is prepared before the reaction. Hence, soft template is easier to build and remove than the hard template. It does not require complex equipment and strict production conditions and the reaction can easily be controlled. Soft template is mostly used to produce various size and sharp structure of nanomaterials.

2.4 The effect of calcination system on the morphology of alumina

The alumina calcination system is very important for obtaining nanoparticle powder with monodispersity and uniform morphology. Nano Al_2O_3 powder, which is composed of widely used α-Al_2O_3, γ-Al_2O_3 and amorphous Al_2O_3, is generally obtained from alumina precursor calcined at different temperatures. Therefore, the compaction among alumina particles of high activity is inevitable at high temperature. Thes results in severe particle agglomeration and resintering of individual particles with surrounding ones after melting with a formation of dendritic structure called "neck formation" of particle [115]. The result of the experiments showed that the calcination temperature, holding time and heating rate

have a significant effect on the morphology of alumina. While the temperature is less than 800ºC, alumina particles can continue to maintain their original morphology. If the temperature becomes higher than 800ºC, the activity of alumina particles is enhanced, and agglomeration begins to occur [116]. Ceresa *et al.* [117] first presented the relationship between temperature and phase transformation of alumina during the calcination process.

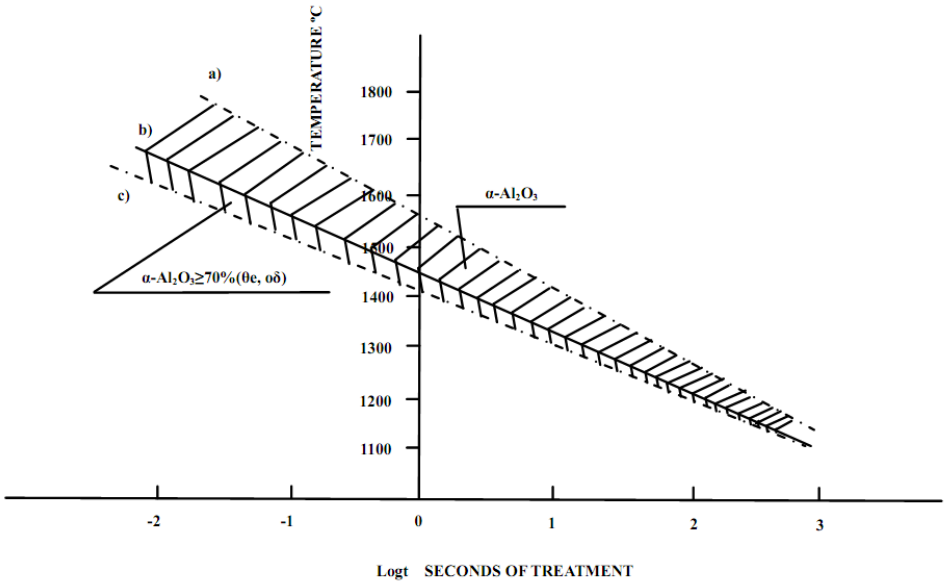

Figure 2.18: The relationship between temperature and phase transformation of alumina [118]

It can be seen from Figure 2.18 that the calcination temperature and time have a significant influence on the transformation of alumina (crystal type). When alumina particles calcined at the desired temperature in order to obtain certain crystal types, the calcination time depends on the size of the precursor. The smaller the particle size of precursor is, the shorter the time required for the calcination is and the higher the temperature of the heat treatment is, the shorter the time required for the calcination is. The

method of controlling the temperature and time during the calcination of Al_2O_3 is well-known. This method ensures that while the Al_2O_3 particles go through a complete phase change, their morphology remains unaffected and the dispersion of particles are reduced [118].

A significant amount of research is carried out in this area. Effective methods are proposed to control the morphology of alumina particles such as using DI water, alcohol and organic solvent mixtures to wash precursor before calcination in order to prevent agglomeration, enhance the dispersion, and increase the specific surface area of alumina [119]. In addition, the sintering properties of the powder can be improved with ultrasonic pretreatment, so that the neck formation created by agglomeration of the particles will not occur until 1400ºC [120]. The phase transformation temperature of γ-Al_2O_3 to α-Al_2O_3 can be decreased if sintering is carried out under the CO_2 or ethanol atmosphere, consequently, the well-crystalline spherical α-Al_2O_3 is eventually obtained [121].

Dispersants and surfactants also play an effective role in dispersion of particles and control of agglomeration. For example, using poly (methacrylic acid), organic acid, glucose, sucrose, inorganic salts, trimethylsilane and other additives [122], which results in a strong electrostatic repulsion among particles, eventually change the polarity of the particle surface from hydrophilic to hydrophobic (water-repellent). Polyacrylamide, silica gel and lignin and other polymer dispersants can form a protective layer with certain strength and thickness on the particle surface and prevent the agglomeration of the particles [123]. Surfactants can form a coating layer of several nanometers on the surface of the particles,

which can reduce the surface energy and effectively hinder the interactions among the particles [124].

Besides, by adding 5 wt% α-Al_2O_3 seed and 44% NH_4NO_3 during the calcination process, the phase transition temperature can be decreased from 1200ºC to 900ºC [125].

The amorphous Al_2O_3 particles obtained at 600ºC is light yellow while the additive is still present on the surface of the particles. This coating gradually disappears while 800ºC is reached. In addition, some additives can decrease the phase transition temperature of α-Al_2O_3 to 1000ºC. As the temperature increases, the grain size of Al_2O_3 will inevitably increase, meanwhile the agglomeration will start to occur. This is due to the fact that when Al_2O_3 is completely transformed to α phase, the spatial arrangement of the O_2 in α- Al_2O_3 occurs, which is the reconstruction of phase transition from face-centered cubic to hexagonal close packed lattice [126]. The effect of different parameters on the properties of alumina nanoparticles has been published and presented in Appendix I.

2.5 Summary

The production of Al_2O_3 can be influenced by various factors such as raw materials, concentration, different synthesis methods, additives, heat treatment system, etc. During the preparation of Al_2O_3, the morphology of the precursors and the protection of the particles during heat treatment play a decisive role in the final morphology of alumina. The morphology will not change during the low temperature heat treatment. However, when high temperature is reached, the diffusion of the powder particles accelerates. Thus, the

particles diffuse from the inside to the surface of the crystal lattice and spread to the surrounding resulting in the neck formation as well as the agglomeration of surrounded particles. The morphology of the particles changes accordingly. The use of various additives effectively reduces the calcination temperature; consequently, the problem of particle agglomeration can be solved. The utilization of template is a new research hotspot with the objective of improving the dispersibility of Al_2O_3 powder and controlling the shape of the sample particles.

Chapter 3

Methodology

3.1 Experimental

The schematic of the methodology is shown in Figure 3.1. It includes:

1. Characterization of the wastewater
2. Treatment of the reagents and improve the purity
3. Preparation of high purity alum solution from the wastewater
4. Production of 5N (99.999% pure) spherical alumina nanoparticles by single templating
5. Production of 5N (99.999% pure) spherical mesoporous alumina nanoparticles by double templating
6. Application of the 5N alumina nanoparticles in different fields:
   a. Preparation of sapphire crystal
   b. Photoacoustic tomography

Each step is presented in detail below.

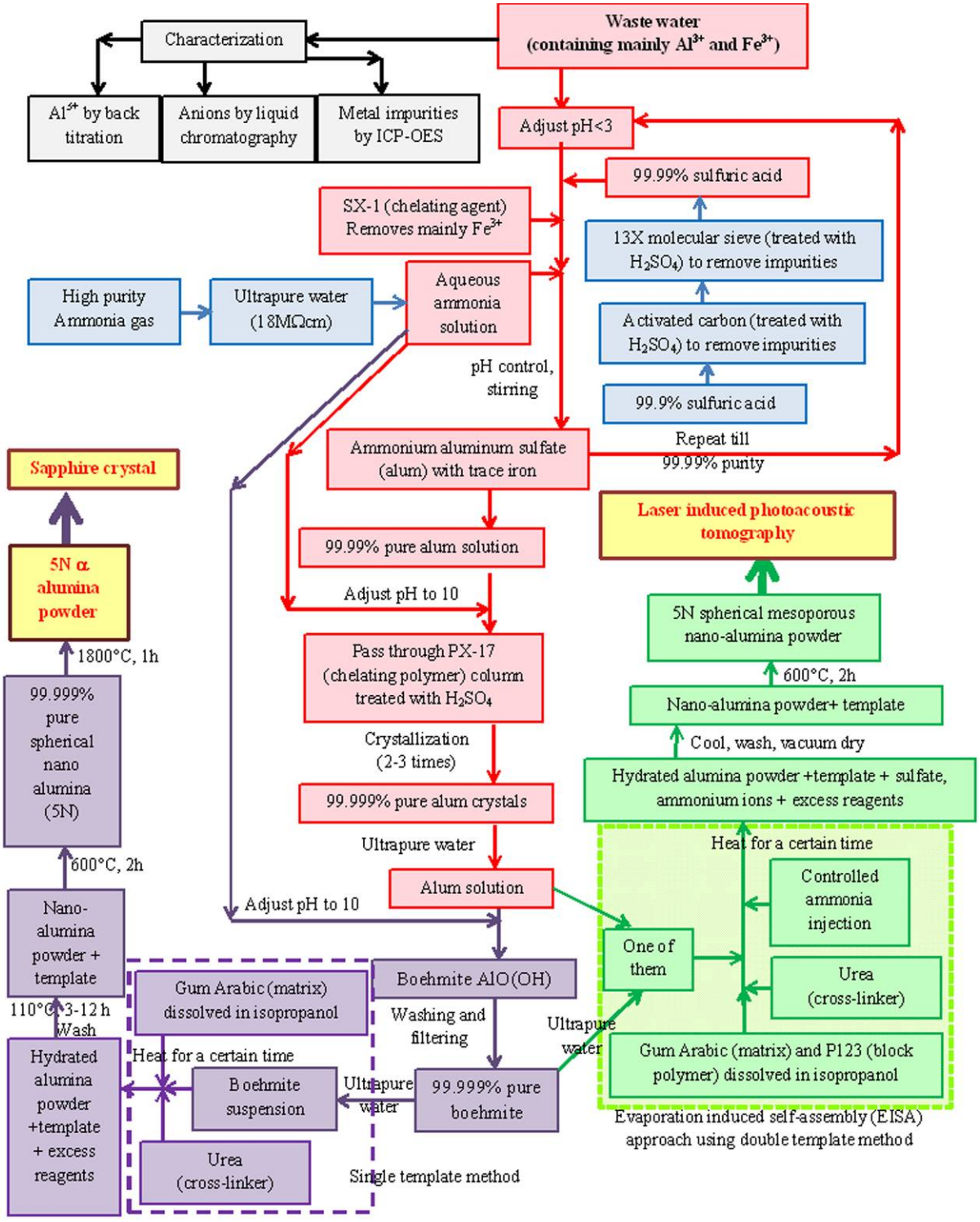

Figure 3.1: Schematic of the methodology

3.1.1 Characterization of the wastewater

The concentration of different metallic impurities in the wastewater sample was measured by ICP-OES (inductively coupled plasma-optical emission spectroscopy). The concentration of Al^{3+} in the wastewater was also measured by back titration method, and the results were compared. The back titration method, being less costly, can be used in the industry. Then the concentrations of the anions in the water sample were measured using LC (liquid chromatography).

a) Back-titration of Al^{3+}

The complexation reaction of aluminum with ethylene-diamine-tetra-acetic acid (EDTA) chelate is usually slow. The rate of reaction is relatively higher at high temperature when the pH of the solution is three. The pH 3 was maintained by acetic acid/sodium acetate (AcH/AcNa) buffer. Thus, measured amount of the AcH/AcNa buffer was added in measured quantity of the water sample. After, known amount of EDTA solution (of known concentration) was added and boiled. This helps all the Al^{3+} ions to form complex. Excess EDTA stays in the solution. Measurement of the excess EDTA can give an idea of the amount of aluminum in the solution. Determining the concentration of a solid by titrating an excess reagent with another reagent is called back-titration. It is helpful when the rate of reaction of the solid with an acid is too slow, in which case the application of the direct titration method is not suitable.

To do this the pH of the medium was changed to 4.5 by adding tetramethyline-triamine. An indicator xylenol orange was added to the solution. The indicator can bind with metal and change color. In the free-state, the color of the indicator is yellow. The color turns to red when it combines completely with a metal ion under acidic condition. Thus, xylenol orange indicator was added to the solution and the color of the solution became yellow. To know the amount of excess EDTA a solution of $ZnCl_2$ was used. $ZnCl_2$ solution was added dropwise. The Zn^{2+} made complex with the excess EDTA as the rate of reaction between Zn^{2+} and EDTA is faster than that between Zn^{2+} and the indicator. As soon as the all the excess EDTA made complex with Zn^{2+}, further addition of $ZnCl_2$ solution resulted in the reaction between the Zn^{2+} ion and the indicator. As the colors of the free and combined indicators are yellow and red respectively, the color of the indicator changed from yellow to orange (combination of yellow and red) and finally the indicator became red. Thus, the red color indicated the end of the titration. From the amount of $ZnCl_2$ solution, the amount of excess EDTA was calculated. This result was in turn used to calculate the concentration of aluminum in the water sample.

Figure 3.2 shows the changes in color (bright yellow → orange → red) of the solution during titration.

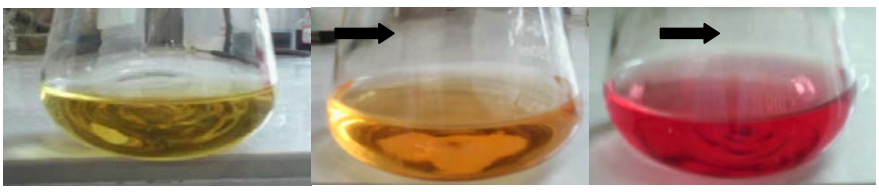

Figure 3.2: Change in color during titration by $ZnCl_2$ solution

3.1.2 Treatment of the reagents and improvement of the purity

At first, the trace elements of activated carbon powder and molecular sieve powder were measured by ICP-OES (inductively coupled plasma optical emission spectrometry). Sulfuric acid was diluted by ultrapure water to have different concentrations (mass fraction 0.98%, 3.87%, 7.61%, 11.22% and 14.65%). Activated carbon and molecular sieve 13X powder was added into sulfuric acid solutions and waited for 12 hours. After soaking, the powders were washed by ultrapure water for 3-5 times and the trace element contents were measured. Every experiment was repeated at least three times and the average of the results were reported. Finally, the removal efficiency of the trace elements for different mass fractions of sulfuric acid solutions were calculated and compared.

3.1.3 Preparation of high purity alum solution from the wastewater

The method is highlighted in red in Figure 3.1. The wastewater was treated with SX-1, sulfuric acid solution, and aqueous ammonia to produce ammonium aluminum sulfate (alum) under controlled pH of 3~3.5. This ammonium aluminum sulfate solution was treated repeatedly till 99.99% pure alum solution was obtained. The pH of the solution was then adjusted to 10, and the solution was passed through a column of PX-17 to remove most of the impurities. Alum crystals with 99.999% purity were produced after 2~3 times of recrystallization. The ultrapure crystals were dissolved in ultrapure water to get the alum solution. The laboratory scale experimental system is shown in Figure 3.3.

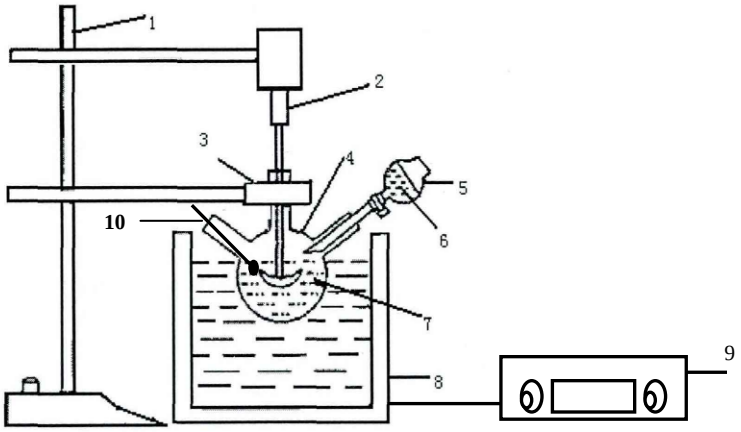

Figure 3.3: Laboratory scale experimental system to obtain high purity alum solution from wastewater

(1.Iron support, 2.High speed teflon stirrer, 3.lron clip, 4.Three necked flask, 5. Funnel 6. Dropper, 7. Reaction solution, 8. Glass water bath, 9. Temperature controller, 10. pH and temperature detector)

3.1.4 Production of 5N (99.999% pure) spherical alumina nanoparticles by single templating

Spherical alumina nanoparticles were synthesized with boehmite (AlO(OH)) as the precursor, gum arabic (GA) as the template, and urea as the precipitant/cross-linker. The details of the method are described in Section 5.2.

3.1.5 Production of 5N (99.999% pure) spherical mesoporous alumina nanoparticles by double templating

Spherical mesoporous alumina materials were synthesized using alum/boehmite (AlO(OH)) as precursor, gum arabic (GA) and P123 as double template, and urea as

precipitant/crosslinker by the evaporation induced self-assembly (EISA) approach. The details of the method are described in section 6.2.

3.1.6 Application of the 5N alumina nanoparticles in different fields

3.1.6.1 Preparation of sapphire crystal

The 99.999% pure spherical nano-alumina powder was heated at 1800°C for 1 h to convert it to α-alumina. In the crystal growth process, the powdered raw material 5N alumina particles need to be pressed into a bulk form to prevent the powdered raw material from being evacuated while exhausting air from the furnace; this process also causes the density of the raw material to increase. Before placing the crystal into the crystal furnace, the furnace must be cleaned and the air flow rate must be increased in order to eliminate excess particulate dust and gas in the furnace. The crucible containing the raw materials must be cleaned with ethanol and acetone before use. Seeds were then stuck to the bottom center of the furnace, with the crucible placed on top of the heat exchanger in the furnace so that their center of gravity will coincide. The bulk form of the raw materials produced by hot-pressing the ball milling mixture was placed into the crucible one by one, in order to avoid introducing impurities during this process. After the materials were placed into the furnace, the furnace was closed. The growth process program was turned on, the parameters were set, and crystal began to grow. Crystal growth using the heat exchange method was divided into the following stages:

(1) Heating and melting: The temperature was increased to 1800°C so that the raw material starts melting. During the process, the cooling helium gas flow rate was adjusted in the seed crystal spindle tube, ensuring that the seed at the bottom of the crucible does not completely melt.

(2) Crystal growth: Once the raw material was melted, the gas flow rate and the temperature gradient in the furnace were increased in order to promote melting. Crystals should grow bottom-up along the seed crystal orientation in the low temperature region.

(3) Annealing and cooling: After the sapphire crystal had reached its final size, the helium flow was reduced to lower the temperature gradient in the furnace, and reduce the thermal stress in the crystal to avoid cracking. At the same time, the heating power was slowly reduced to zero and the crystal began to cool to room temperature. Sapphire crystal samples must undergo several processes, such as orientation and slicing using crystal X-ray orientation instruments, cutting using a single wire-cutting machine, lapping and copper polishing using a grinding machine, and grinding and polishing using a fine-polishing grinding machine, in order to obtain a two-inch sapphire wafer.

During the experiments on sapphire crystal growth, alumina with different morphologies was used. For each case 10 sapphire crystals were produced. In this study, the average length of crystal rods produced were calculated, using the total length of crystal rods for each crystal as an index, to determine the influence of different intermediate Al_2O_3 morphologies on sapphire growth using the heat exchange method.

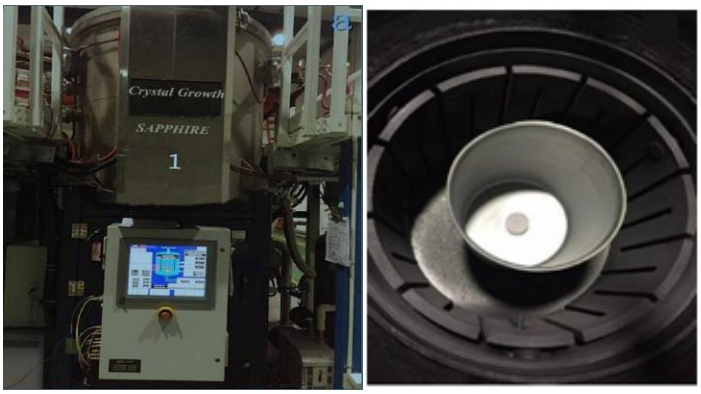

(a) (b)

Figure 3.4: Heat exchange method crystal growth equipment (a) outside view of the crystal growth furnace, (b) inside view of the crystal furnace.

3.1.6.2 Photoacoustic (PA) tomography

Optical imaging plays an important role in preclinical and clinical imaging. The major constraint of optical imaging is diffusion of light. This diffusion reduces the spatial resolution in deep-tissue imaging. Photoacoustic (PA) tomography is a new technique that can overcomes this challenge. In PA tomography absorbed optical energy is converted into acoustic energy. As acoustic waves scatter much less than optical waves in tissue, PA tomography can generate high-resolution images. In this method chromophores (such as haemoglobin present in blood) or optically active chemicals (such as gold nanoparticles injected in blood stream) are irradiated by short laser pulse. These chemicals are commonly known as target. The pulse energy is partially absorbed by the target and converted into heat, which generates a local transient temperature rise, followed by a local pressure rise through thermo-elastic expansion, and may cause cracks in the particles. The pressure and the cracks generate ultrasonic waves, which are detected by ultrasonic transducers placed

outside the tissue. A PA image is then formed by resolving the origins of the ultrasonic waves from their arrival times. Gold nanoparticles can act as the target material for PA tomography. In this thesis, some preliminary works were done on gold particles that can be used as target materials for PA tomography (see Appendix II). The response of gold nanoparticles can be increased if a cluster of gold nanoparticles (separate nanoparticles in a group) is present. This can be achieved by doping gold nanoparticles into mesoporous alumina matrix. The gold nanoparticles will be embedded in the pores of the alumina matrix. Thus, a number of studies have been done on the modification of alumina nanoparticles so that they can be used as matrix for gold nanoparticles in PA tomography.

3.2 Characterization of alumina samples

X ray diffraction (XRD, PANalytical X'Pert PRO, Almelo，Holland) and scanning electron microscope (SEM, KYKY-2800B) were used to study the crystallinity and morphology of prepared powders and sapphire wafers. Transmission electron microscopy (TEM) measurements were carried out using Tecnai G2 F20 operated at 200 kV. All samples were first dispersed in ethanol and then collected by using copper grid covered with carbon films for measurements. Nitrogen sorption isotherms were measured at 77 K on a Micromeritics Tristars 3000 analyzer. Before measurements, the samples were degassed in a vacuum at 180ºC for at least 6 h. The Brumauer-Emmett-Teller (BET) method was utilized to calculate the specific surface areas (SBET), using adsorption data in a relative pressure range from 0.04 to 0.2. The pore volume and pore size distributions derived from the adsorption branches of isotherms by using Barrett-Joyner-Halenda (BJH)

model. Transmissivity testing (UV-VIS-NIR) is a test method for characterizing the optical transmittance of crystals in the ultraviolet, visible, near-infrared bands, which is the main characterization method for the optical properties of crystal. The main principle of the test is the Beer-Lambert law. After a certain band of light is transmitted through the crystal materials, the light intensity remaining after absorption, scattering, reflection and the like is deducted. The transmittance of sapphire wafers at room temperature within 190~1100 nm was measured using the Cary60 type UV-VIS-NIR transmittance tester.

Chapter 4

Preparation of high purity alum solution from the wastewater

4.1 Introduction

Ultra-high purity nano-alumina is a value-added product that can be prepared from wastewater containing aluminum. Alumina powder is usually produced from bauxite ore by the Bayer process. However Bayer process, as it is, cannot control the size distribution of the nanoparticles. The quality of alumina nanoparticles improve significantly if the purity is 99.999% and the size distribution is uniform. The existing methods, which are variants of the Bayer process, are not capable of extracting high purity alumina with narrow size distribution from wastewater. Thus, developing a novel method not only to extract alumina with high purity (99.999%) from wastewater but also to produce alumina with specific average particle size and uniform size distribution has significant influence on the high value-added applications of alumina. Furthermore, when the value of these applications exceeds not only the cost of recycling of wastewater but also the cost of HPA production, wastewater treatment becomes sustainable.

In this chapter, the extraction of aluminum from the wastewater in the form of alum is explained. This alum solution was later used to produce 99.999% pure (5N) nano-alumina particles. The effects of synthesis conditions such as amount of additives, contact time and temperature on purity of alumina are discussed.

4.2 Results & Discussion

4.2.1 Characterization of the wastewater

The wastewater (W-AA) was analyzed initially by LC (for the anions) and ICP-OES (for the cations). Two typical test results for two water samples (W-AA1 and W-AA2) are given in Table 4.1.

As sodium and potassium salts are soluble in water and do not precipitate out during treatments with acids or alkalis, small concentrations of sodium and potassium are not a major concern. It is possible to remove iron selectively from the solution by SX-1 at pH less than 3. Thus, wastewater of the type W-AA-2, which contained only iron, sodium and potassium cations, is ideal for the method used in this work. However, wastewater of compositions similar to W-AA-1 was acceptable. The pH value of 0.5 showed that the water samples were highly acidic. The analysis by LC showed that both the water samples contained mainly sulfate anions.

Table 4.1 Impurity content of the wastewaters

Raw materials	pH	Element content (%)									
		Al	Fe	Pb	Cu	Si	Ca	Na	K	Mg	Ni
W-AA-1	0.5	1.6	0.0060	0.0030	0.0020	-	-	0.0020	0.0010	-	0.0010
W-AA-2	0.5	1.1	0.0003	-	-	-	-	0.0005	0.0001	-	-

4.2.2 Treatment of the reagents and improvement of the purity

As discussed in the methodology section, the different reagents/additives (activated carbon, 13X and PX-17), to be used in purification of H_2SO_4 and alum solution, were purified and tested. Table 4.2 shows the impurity content in the reagents before the treatment.

Table 4.2: Trace element content of additives before treatment

Additives (without treatment)	Trace elements (ppm)									
	Al	Fe	Pb	Cu	Si	Ca	Na	K	Mg	Ni
Activated carbon	-	-	-	-	630	112	580	400	307	-
Molecular sieve (13X)	-	-	-	-	-	21	30	27	-	-
PX-17	-	-	-	-	-	-	75	11	-	-

The reagents were treated with different dilutions of sulfuric acid of purity 99.9% in order to remove different impurities from the reagents. The treated additives were washed and the impurity contents were measured. Table 4.3 shows the removal efficiency for different impurities from the different reagents as a function of the dilution of the sulfuric acid. The focus is to remove Si, Ca, Na, K and Mg due to high impurity content of reagents and the results in Table 4.3 shows that the best removal efficiency (except for Si) was achieved with 14.65% sulfuric acid.

Table 4.3: Comparison of removal efficiency of diluted sulfuric acid solutions

Sulfuric acid mass fraction (%)	Removal efficiency of different elements (%)														
	Si			Ca			Na			K			Mg		
	C#	13X*	PX-17	C#	13X	PX-17	C#	13X	PX-17	C#	13X	PX-17	C#	13X	PX-17
0.98	2.0	-	-	38	8	-	24	30	36	28	35	45	41	-	-
3.87	2.2	-	-	43	10	-	30	32	49	30	47	53	52	-	-
7.61	2.5	-	-	50	12	-	48	49	55	58	60	66	60	-	-
11.22	3.3	-	-	67	17	-	62	71	73	70	76	79	74	-	-
14.65	5	-	-	82	21	-	80	83	89	78	89	91	87	-	-

*13X: molecular sieve 13X C#: Activated carbon

Table 4.4 shows that a substantial amount of the impurities were removed from the reagents. It may be noted that the activated carbon and molecular sieve still contained a large amount of impurities even after the treatment with sulfuric acid.

Table 4.4: The trace element content of additives after treatment

Treated additives	Trace elements (ppm)									
	Al	Fe	Pb	Cu	Si	Ca	Na	K	Mg	Ni
Activated carbon	-	-	-	-	580	20	120	85	40	-
Molecular sieve 13X	-	-	-	-	-	12	5	3	-	-
PX-17	-	-	-	-	-	-	7	2	-	-

4.2.3 Purification of H_2SO_4

Sulfuric acid of purity 99.9% was treated with activated carbon followed by molecular sieve 13X. This treatment increased the purity of the sulfuric acid to 99.99%. This sulfuric acid was later used for the treatment of wastewater.

4.2.4 Preparation of high purity alum solution from the wastewater

a) Effect of number of cycles for different reagents on the removal of impurities

Experiments were performed using measured amount of different reagents (3 g for activated carbon, 3 g for PX-17, 0.006 g of SX-1 and 0.3 g of molecular sieve 13X per 300 ml of wastewater). The temperature was set to 90°C, and the contact time was 180 min. In this study, the pH of the solutions of PX-17, SX-1 and molecular sieve 13X was set based on the manufacturer's document with a view to remove most of the iron impurities. The pH values set for PX-17, SX-1, and molecular sieve 13X were 10.0, 2.8 and 3.0, respectively. Tables 4.5 to 4.7 show the efficiency of the impurity removal at different cycles of treatment of wastewater. After each cycle, the alum was crystallized and analyzed for impurity content. The results show that activated carbon cannot remove the different metallic impurities from wastewater. Molecular sieve 13X has medium efficiency, whereas SX-1 and PX-17 have very high efficiency of impurity removal. It may be noted that PX-17 is costlier than SX-1. Thus, SX-1 was used to remove most of the impurities using three cycles. The remaining impurities were removed by one cycle of PX-17 since PX-17 can remove 88% of impurities in the first cycle.

Table 4.5: Total removal efficiency of the first crystallization

Additives	Total removal efficiency (%)	Trace element residuals in the first crystallization (ppm)								
		Fe	Pb	Cu	Si	Ca	Na	K	Mg	Ni
Activated carbon	0.0	35	20	12	50	11	10	8	10	8
Molecular sieve 13X	39.0	30	15	10	12	8	10	2	-	5
SX-1	66.7	15	14	8	1	-	8	1	-	3
PX-17	88.0	3	5	5	-	-	3	1	-	1

Table 4.6: Total removal efficiency of the second crystallization

Additives	Total removal efficiency (%)	Trace element residuals in the second recrystallization (ppm)								
		Fe	Pb	Cu	Si	Ca	Na	K	Mg	Ni
Activated carbon	0.0	20	16	9	43	10	5	3	-	5
Molecular sieve 13X	56.0	23	10	8	10	5	7	-	-	3
SX-1	92.0	2	3	2	-	-	4	1	-	-
PX-17	90.6	3	4	3	-	-	2	1	-	1

Table 4.7: Total removal efficiency of the third crystallization

Additives	Total removal efficiency (%)	Trace element residuals in the third recrystallization (ppm)								
		Fe	Pb	Cu	Si	Ca	Na	K	Mg	Ni
Activated carbon	0.0	20	13	8	30	5	2	-	-	-
Molecular sieve 13X	64.0	20	8	6	10	3	5	-	-	2
SX-1	92.7	2	2	2	1	-	3	1	-	-
PX-17	91.0	3	4	3	-	-	1	1	-	1

Figure 4.1 summarizes the purity of the alum crystals after different cycles of treatment for different reagents. PX-17 has the best removal efficiency in the first cycle. SX-1 reaches a similar efficiency only after the second cycle. Finally, both PX-17 and SX-1 have up to 91%~92% of total removal efficiency and the final purity of HPA reach as high as 99.9987% and ~99.9989%, respectively.

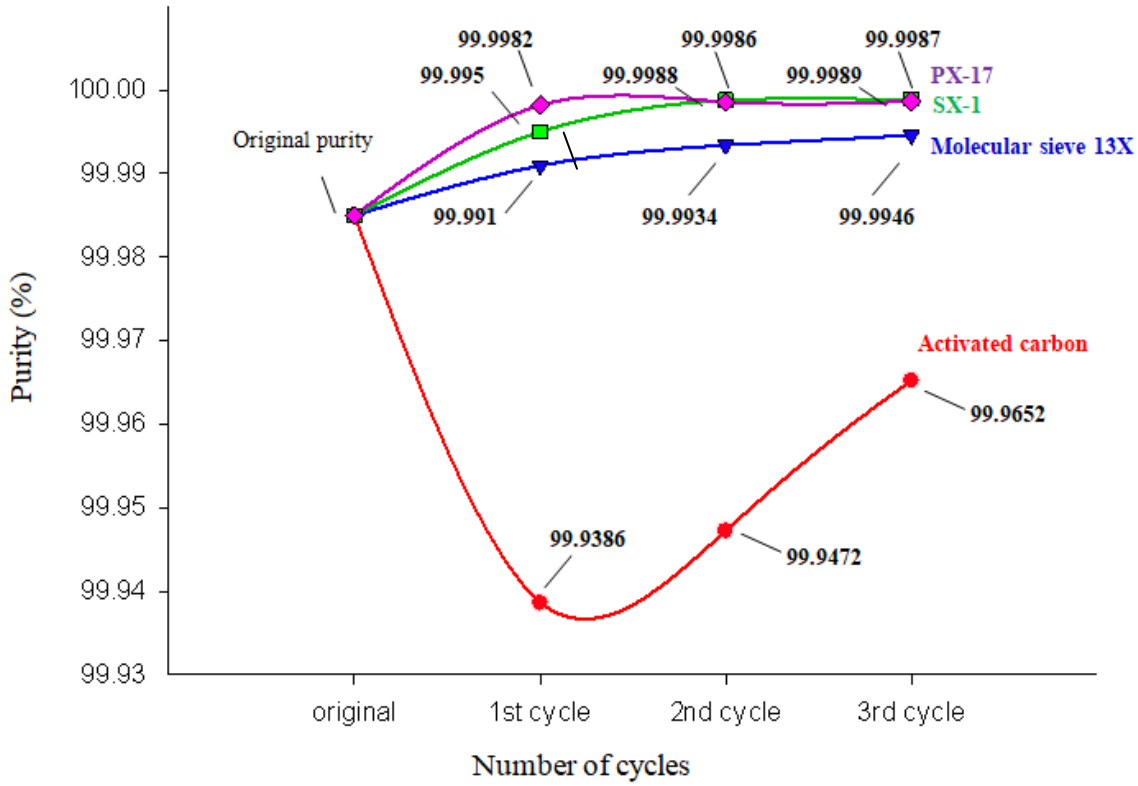

Figure 4.1: Comparison of the HPA purity and cycles of recrystallization by adding different additives (Based on the original purity of raw material as 99.85% and pH 0.5)

b) Effect of amount of reagents on total removal efficiency

In this study, the pH of the solutions to be purified with PX-17, SX-1 and molecular sieve 13X was set based on the information received from the manufacturer with an objective of removing most of the iron impurities. The pH values set for PX-17, SX-1, and molecular sieve 13X were 10, 2.8 and 3, respectively. The reaction temperature was 90°C, and the contact time was 180 min. For all the cases, the water samples were treated only once. Tables 4.8 to 4.10 show the impurity removal efficiency of different reagents. The amount of PX-17, which results in removal efficiency of 90 %, is around 10 g/L (3.0 g/300 ml). SX-1 has 87% of removal efficiency when amount of approximately 0.017 g/L (0.005

g/300 ml) is used. Molecular sieve 13X reaches 59 % of removal efficiency at amount of 1 g/L. Although PX-17 has excellent removal efficiency, it requires a large amount of reagents, and it is costly. Molecular sieve 13X has low removal efficiency of just 59% but the amount required is less than that of PX-17. Compared to others, SX-1 not only necessitates the utilization of a small amount reagent, but it also can reach to 87 % of removal efficiency. Thus, for the final treatment of the wastewater 0.005 g of SX-1 per 300 ml wastewater was used for three cycles. Then, 3 g of PX-17 per 300 ml of wastewater was used for one cycle.

Table 4.8: Relation between PX-17 amount and total removal efficiency

G (additives, g) / V(solution, ml)	Total removal efficiency of additives %
	PX-17 (pH=2~2.5)
0.5 / 300	38
1.0 / 300	45
1.5 / 300	60
2.0 / 300	72
2.5 / 300	88
3.0 / 300	90

Table 4.9: Relation between SX-1 amount and total removal efficiency

G(additives, g) / V(solution, ml)	Total removal efficiency of additives %
	SX-1 (pH=2.5~3)
0.001 / 300	30
0.002 / 300	67
0.003 / 300	78
0.004 / 300	86
0.005 / 300	87
0.006 / 300	87

Table 4.10: Relation between molecular sieve 13X amount and total removal efficiency

G(additives, g) / V(solution, ml)	Total removal efficiency of additives %
	13X (pH=2.5~3)
0.05 / 300	35
0.10 / 300	40
0.15 / 300	51
0.20 / 300	58
0.25 / 300	58
0.30 / 300	59

c) Effect of contact time on total removal efficiency

In this study the pH of the solutions to be purified with PX-17, SX-1 and molecular sieve 13X was set based on the information received from the manufacturer with an objective of removing most of the iron impurities. The pH values set for PX-17, SX-1, and molecular sieve 13X were 10.0, 2.8, and 3.0, respectively. The reaction temperature was 90°C, and the contact time was varied. For all the cases, the water samples were treated only once. Figure 4.2 presents the contact time as a function of total removal efficiency for three different reagents. The results show that PX-17 and molecular sieve 13X take more time to reach equilibrium than SX-1. The composition of PX-17 has porous structure combined with chelating cation exchange resin. Thus, first chelating reaction takes place between PX-17 and the cations in the solution. Then, its internal pores and channels strongly adsorp the cations to remove the metal impurities from the solution. 13X molecular sieve has a porous structure made of aluminum silicate and 13X zeolite, which is the major component. It has large amount of internal open pores and channels. 13X molecular sieve and PX-17 have a large specific surface area. The surface area controls the

time to reach equilibrium in the solution. SX-1 is a highly efficient agent. It rapidly reacts with the cations in different pH ranges. Removal does not depend on physical adsorption. Since the reaction is fast, SX-1 has shorter removal time compared to those for the 13X molecular sieve and PX-17. Based on this study, the contact times for SX-1 and PX-17 were set to 50 min and 150 min, respectively, for each cycle.

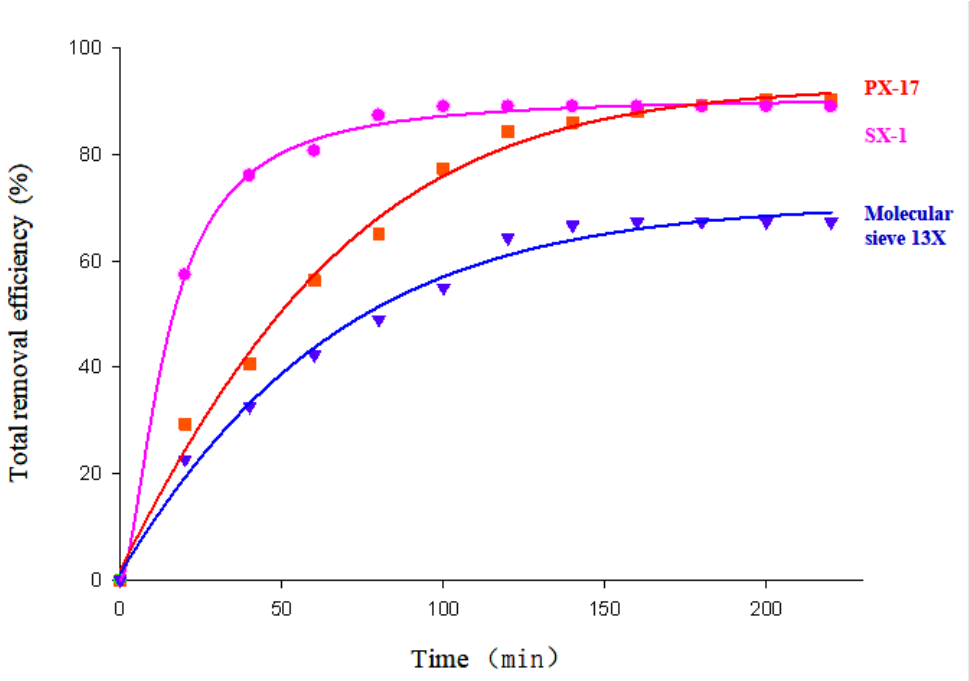

Figure 4.2: Total removal efficiency as a function of reaction time

d) Effect of reaction temperature on total removal efficiency

In this study the pH values set for the solutions purified with PX-17, SX-1, and molecular sieve 13X were 10, 2.8 and 3, respectively. The reaction temperature was varied, and the contact time was set to 50 min. For all the cases, the water samples were treated only once. Figure 4.3 shows the efficiency of impurity removal as a function of reaction

temperature. The figure indicates that the total removal efficiency increases with increasing reaction temperature for PX-17 and molecular sieve 13X. SX-1 shows that it reaches equilibrium at around 40°C. Above this temperature, there is much less influence of temperature on the removal of impurities. On the contrary, total removal efficiency of PX-17 and molecular sieve 13X rapidly increases with increasing temperature because adsorption process of both PX-17 and molecular sieve 13X is endothermic. Temperature increase is conducive to the adsorption, thus, adsorption capacity increased with increase in temperature. Based on the results, for the production of pure alum from wastewater, the reaction temperature for SX-1 was set to the 30°C, and that for PX-17 was set to 90°C.

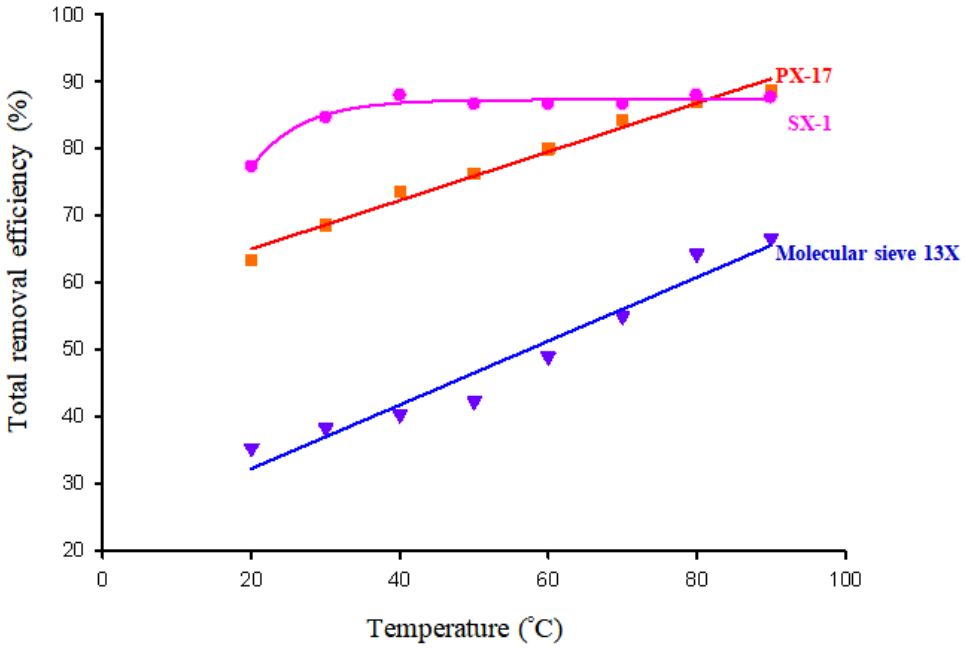

Figure 4.3: Total removal efficiency as a function of temperature

Based on the results discussed in the sections 4.3.1 to 4.3.4, the wastewater was first treated with SX-1 (0.005 g/300 ml wastewater, pH 2.8) at 30°C for 3 cycles (150 min per

cycle). Then, the purified water was treated with PX-17 (3.0 g/300 ml wastewater, pH 10) at 90°C for 1 cycle (50 min). It was possible to extract 99.999% pure alum from the waste-water using this method. Two patent applications were filed for the method of extracting ultrapure alumina. The copies of the applications are given in Appendix III.

Chapter 5

Production of 5N (99.999% pure) spherical alumina nanoparticles by single templating

5.1 Introduction

5N (99.999% pure) spherical alumina nanoparticles were prepared using 5N Alum as the aluminum source, urea ($(NH_2)_2CO$) as the precipitant/cross-linker, and gum arabic (GA) as the template followed by heating at 600ºC. The structure and morphology of the alumina nanoparticles were characterized using X-ray diffraction (XRD), scanning electron microscopy (SEM), and BET equipment. Gum arabic powder is a natural, non-toxic, water-soluble polymer. The steric effect of its long chain structure effectively prevents particles from aggregating, so it is often used in the preparation of silver. The gum arabic/urea weight ratio was adjusted to obtain spherical alumina nanoscale particles. Also the effect of synthesis temperature, time, and template amount on product morphology was studied. The detailed methodology and the results are presented in this chapter.

5.2 Production of 5N (99.999% pure) spherical alumina nanoparticles by single templating

Spherical alumina nanoparticles were synthesized with boehmite (AlO(OH)) as the precursor, gum arabic (GA) as the template, and urea as the precipitant/cross-linker. The boehmite solution was prepared from the 99.999% alum solution (Figure 3.1). The effect of

different reaction temperatures, reaction times, and GA/urea ratios were investigated in order to understand their effect on the properties of the alumina nanoparticles. Table 5.1 shows the different process parameters.

Table 5.1: Process parameters for alumina prepared under different conditions

Sample Number	Weight Ratio (GA/Urea)	Temperature (°C)	Time (h)
A	1.250	120	3
B	1.250	140	3
C	1.250	160	3
D	1.250	180	3
E	1.250	140	9
F	1.250	140	15
G	0.000	140	3
H	0.625	140	3
I	1.250	140	3
J	2.500	140	3

The synthesis process was as follows. Firstly, alum was dissolved in the ultrapure water (resistivity = 18 MΩ*cm) to prepare 0.4 mol/L of alum solution. The GA was dissolved in isopropanol; urea was added and the GA/urea weight ratio was maintained at the desired value. The GA/urea mixture was then stirred and dissolved in a solution. The prepared additive solution was added to the alum solution, and stirred in the autoclave for different times at different temperatures (Table 5.1). The solution was then rapidly cooled to room temperature in a cooling bath. The precursor was cleaned with ultrapure water three to five times and dried for 3-12 h at 110°C. After drying, the white spherical alumina nanoparticles were obtained.

5.3 Results

5.3.1 The Effect of Synthesis Conditions on Spherical Alumina Morphology

Boehmite samples A-F (Table 5.1) obtained by different contact times and temperatures were analyzed by XRD. The XRD patterns under different synthesis times and temperatures (Figure 5.1) indicate that when the synthesis temperature was 120°C and 140°C, and the synthesis time was 3 h, the prepared precursors were mainly amorphous products A and B. When the synthesis temperature was increased to 160°C and 180°C, precursors C and D began to crystallize and produced AlO(OH). Based on these results, it can be concluded that the system does not have enough energy to crystallize and promote migration when the solution temperature is low and the contact time is short (3 h or less), in which case the samples tend to become amorphous. However, when the solution temperature was increased, different diffraction peaks emerged, and their intensity and width increased with increasing temperature indicating that the crystallinity of the particles had increased. The reaction system also had enough energy to crystallize when the precursors E and F were synthesized at 140°C for a longer period of time, between 9 and 15 h. Compared with precursors C and D, which were obtained at higher temperature, the intensity and width of the diffraction peaks of precursors E and F, which were obtained using longer reaction times, were smaller. This indicates that the crystallinity of the particles was weaker if the reaction time was long at lower temperature compared to the case where reaction temperature was higher but reaction time was shorter. The morphology

and crystal structure of the products were mainly controlled by regulating the average crystal growth rate.

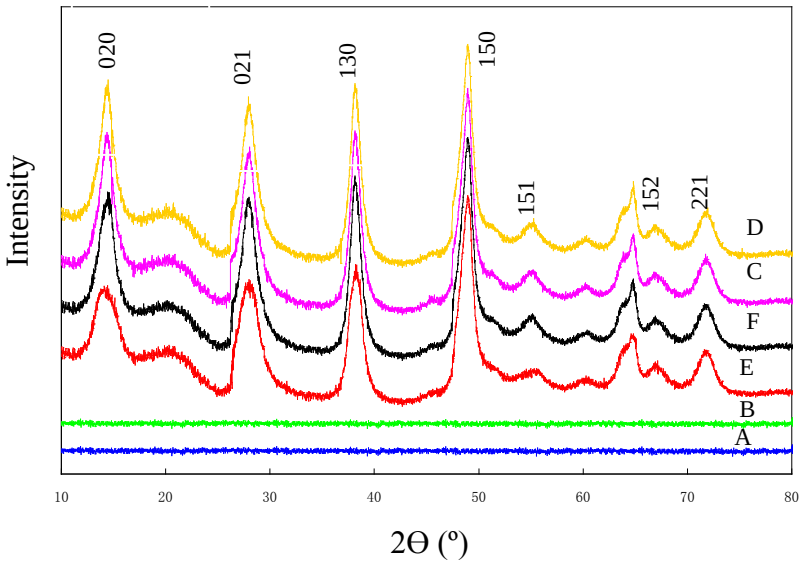

Figure 5.1: XRD patterns for the precursor under different synthesis conditions (A) Amorphous-120°C-3 h; (B) Amorphous (140°C-3 h); (C)AlO(OH) (160°C-3 h); (D) AlO(OH) (180°C-3 h); (E) AlO(OH) (140°C-9 h); (F) AlO(OH) (140°C-15 h).

Figure 5.2 shows the XRD pattern for the spherical alumina after calcination at 600°C. Samples A and B were both transformed into γ-Al_2O_3 by amorphous precursors. Samples C, D, E, and F were all crystalline γ-Al_2O_3 (Joint Committee on Powder Diffraction Standards (JCPDS) No. 10-0425). The diffraction peak position of the crystalline γ-Al_2O_3 did not change with change in temperature or time, but the intensity and width of the diffraction peak were larger. This means that the amorphous precursor prepared under a lower synthesis temperature required more energy to promote grain crystallization and transformation into γ-Al_2O_3.

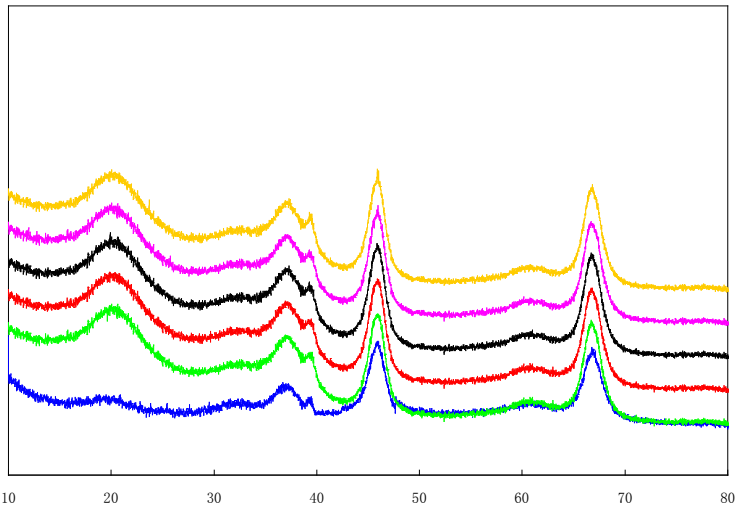

Figure 5.2: XRD patterns for spherical alumina under different synthesis conditions at 600°C (A) Al_2O_3 (120°C-3 h); (B) Al_2O_3 (140°C-3 h); (C) Al_2O_3 (160°C-3 h); (D) Al_2O_3 (180°C-3 h); (E) Al_2O_3 (140°C-9 h); (F) Al_2O_3 (140°C-15 h).

Figure 5.3 shows the SEM images of spherical alumina samples at different synthesis times and temperatures. The image demonstrates that temperature has a great influence on the shape of the sample, and the temperature of 140°C facilitates the formation of spherical particles. When the temperature was 120°C, the produced sample particles were mainly lamellar, spherical, and massive (Figure 5.3 (a)); when the temperature reached 140°C, the shape of the sample particles was regular and spherical with a smooth surface, and the particle size was between 100–300 nm (Figure 5.3 (b)). As the temperature continued to increase, many particles crystallized and became fixed crystals. They can be completely transformed into γ-Al_2O_3 by calcining at 600°C, but the amorphous precursors need more energy to promote the phase transformation, and the crystallization and transformation process was relatively slower to form γ-Al_2O_3 at this temperature. This mechanism was conducive to the formation of spherical alumina (Figures 5.1, 5.2, and 5.3).

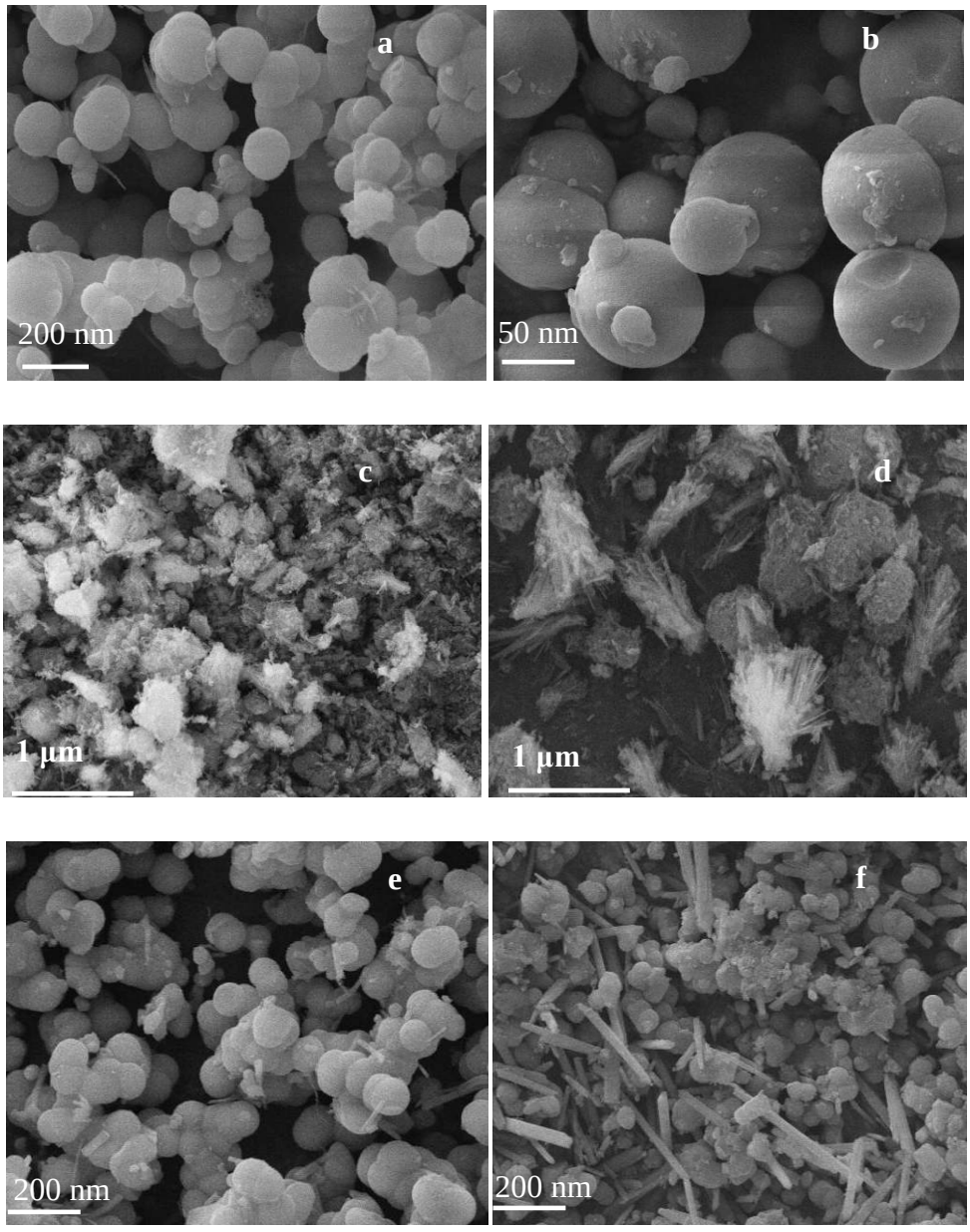

Figure 5.3 SEM images of spherical alumina samples (heated at 600ºC) under different synthesis conditions

(a) Al_2O_3 (120°C-3 h); (b) Al_2O_3 (140°C-3 h); (c) Al_2O_3 (160°C-3 h); (d) Al_2O_3 (180°C-3 h); (e) Al_2O_3 (140°C-9 h); (f) Al_2O_3 (140°C-15 h).

In addition, carbonization tended to occur when the gum arabic powder synthesized under high temperatures and lost some of its template effect, which was not conducive to the development and formation of spherical particles. The samples therefore became irregular floccus aggregating together (Figures 5.3 (c), 5.3 (d)). A long synthesis time was also not conducive to the development of spherical alumina particles (Figures 5.3 (e) and 5.3 (f)) and tended to develop flocculent, strip, and irregular particles, which affected the normal development and growth of spherical particles.

5.3.2 The Effect of Gum Arabic (GA)/Urea Weight Ratio on Spherical Alumina Morphology

In the synthesis process, the template quality has a great influence on the morphology of the samples.

Table 5.2 Morphology of alumina (calcined at 600ºC) with different GA/urea weight ratios

Sample Number	Weight Ratio （GA/Urea）	Intermediate Al_2O_3 particle size (nm)	Intermediate Al_2O_3 Shape	Density of Crystal Growth Raw Material Al_2O_3 (g/cm^3)	Figure
G	0	1500~2000	Strip, irregular rectangle	3.52	5.4 (a)
H	0.625	500~1000	Strip, partially spherical	3.66	5.4 (b)
I	1.250	50~300	Spherical	3.85	5.4 (c)
J	2.500	＞500	Irregular massive, partially spherical	3.81	5.4 (d)

Table 5.2 shows the test results for different weight ratios of GA/urea used in the preparation of spherical alumina. Table 5.2 and Figure 5.4 show that when the GA/urea

weight ratio was zero, the intermediate Al_2O_3 particles were strips and irregular rectangles with random distribution and accumulation after calcination at 600ºC.

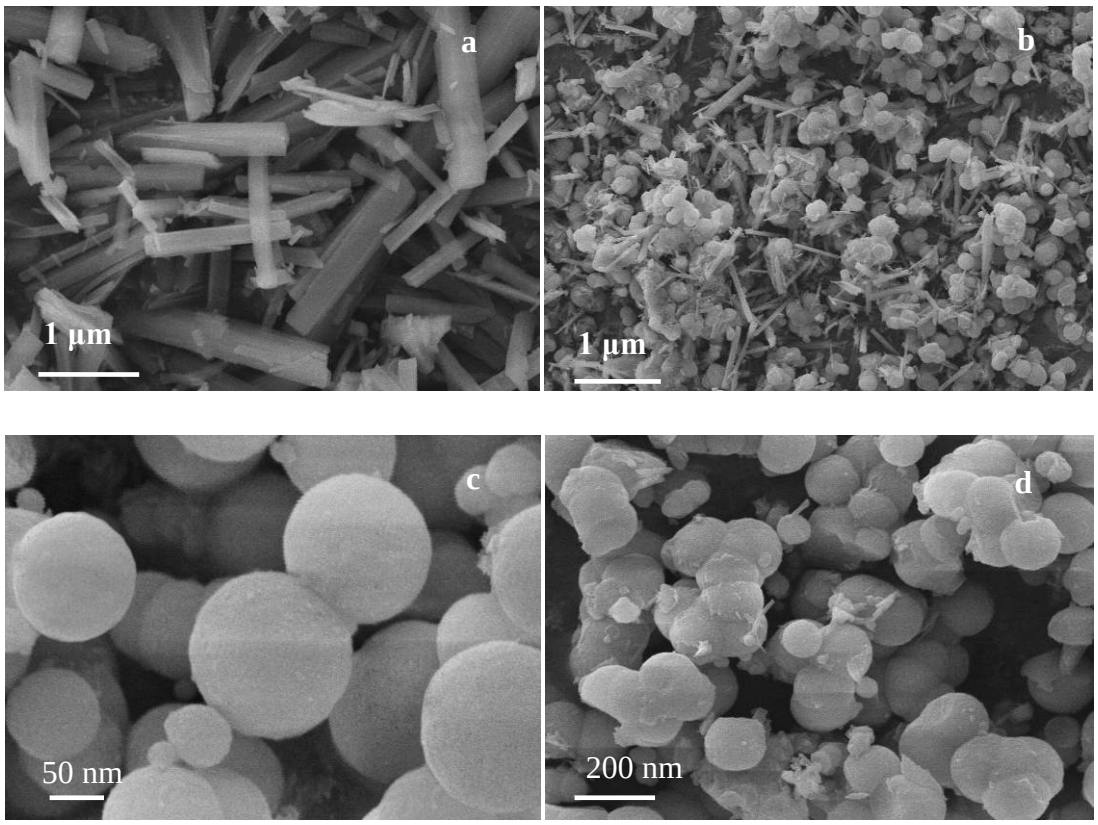

Figure 5.4: The SEM images of intermediate Al_2O_3 (calcined at 600ºC) prepared according to different GA/urea weight ratios (a) Al_2O_3-0; (b) Al_2O_3-0.625; (c) Al_2O_3-1.25; (d) Al_2O_3-2.5.

The particle sizes were between 1000 and 2000 nm. The density of Al_2O_3 raw material was 3.52 g/cm^3 after calcination at 600ºC. When the GA/urea weight ratio was gradually increased, the shape of the intermediate Al_2O_3 particles became spherical, the particle size decreased, and the density gradually increased. Finally, when the GA/urea weight ratio was 1.25, the intermediate Al_2O_3 particles became regularly spherical, the particle size was

within the range of 50 nm to 300 nm, and the density increased to 3.85 g/cm^3. However, if the weight ratio continued to increase, the excess GA increased the viscosity in the synthesis, resulting in a weakened template steric effect and a reduced homogeneous nucleation. In this case, the particles were not conducive to dispersal. The experimental results showed that the intermediate particle size and shape have a direct impact on the density of Al_2O_3 raw material. This indicates that high temperature calcination and spherical intermediate Al_2O_3 with particle sizes of 50 nm to 300 nm can significantly increase the density of Al_2O_3 raw material.

Chapter 6

Production of 5N (99.999% pure) spherical mesoporous alumina nanoparticles by double templating

6.1 Introduction

This chapter describes the preparation and characterization of nanoscale – spherical mesoporous alumina, using 5N alum as aluminum source, urea ($(NH_2)_2CO$) as precipitant/cross-linker, gum arabic (GA) and PEO-PPO-PEO (Pluronic P123) as mixed templates followed by heating at 600ºC. The structure and morphology of the products were characterized by XRD, SEM, TEM and NH_3-TPD (temperature programmed desorption). The effects of reaction temperature, time and the addition of mixed template on the phase structure, micromorphology, optical absorption, and other properties of the samples were studied. The experimental results show that the low temperature and short reaction time facilitate to the formation of nanoscale - spherical mesoporous alumina.

Gum arabic powder is a natural non-toxic water-soluble polymer. Because the steric hindrance effect of its long chain structure can effectively prevent particle aggregation, it is often used in the preparation of metallic silver. P123 is a nonionic block copolymer, often used as a crystal structure modifier in the preparation of mesoporous materials. During this study, nanoscale-spherical mesoporous alumina has been successfully prepared. The evaporation induced self-assembly (EISA) approach was used and double template ratio was adjusted between 0 and 4. The effect of synthesis temperature, time and the addition of

mixed template on the structure and morphology of the product were investigated. The detailed methodology and the results are presented in this chapter.

6.2 Production of 5N (99.999% pure) spherical mesoporous alumina nanoparticles by double templating:

Spherical mesoporous alumina materials were synthesized using alum/boemite (AlO(OH)) as precursor, gum arabic (GA) and P123 as double template, and urea as precipitant/cross-linker by the evaporation induced self-assembly (EISA) approach. Different reaction temperatures (120°C, 140°C, 160°C, and 180°C), reaction times (3h, 9h, and 15h) were tested. The GA/P123 weight ratios were maintained in the range of 0-4, and the GA/urea weight ratio was set to 1.25.

Table 6.1 shows the different process parameters. The effect of reaction temperature and time on the morphology of the alumina particles were studied using samples I to VI. The effect of GA/P123 ratio on the nature of the alumina particles were studied with samples VII to XI.

Table 6.1 Process parameters for alumina preparation under different conditions

Sample Number	Weight Ratio (GA/Urea)	Weight Ratio GA/P123	Temperature (°C)	Time (h)
I	1.25	0.625	120	3
II	1.25	0.625	140	3
III	1.25	0.625	160	3
IV	1.25	0.625	180	3
V	1.25	0.625	140	9
VI	1.25	0.625	140	15
VII	1.25	0.000	140	3
VIII	1.25	1.000	140	3
IX	1.25	2.000	140	3
X	1.25	3.000	140	3
XI	1.25	4.000	140	3

Alum/boehmite was dissolved in ultrapure water (resistivity=18MΩcm) to prepare a solution. Measured quantities of GA and P123 were dissolved in isopropanol, then urea was added, and stirred. Afterwards, the alum solution was added, and this solution was kept in an autoclave at a desired temperature for a certain time. After the reaction, the solution was rapidly cooled to room temperature, then washed with ultrapure water and ethanol 3-5 times, and dried under vacuum at 80°C. The alumina particles were calcined at 600°C for 2 h to obtain the white spherical mesoporous alumina powder.

X-ray diffraction (PANalytical X'Pert PRO) and scanning electron microscope (KYKY-2800B) were used to study the crystallinity and morphology of prepared powders. Transmission electron microscopy (TEM) measurements were carried out on Tecnai G2 F20 operated at 200 kV. All samples were first dispersed in ethanol and then collected by using copper grid covered with carbon films for measurements. Nitrogen sorption isotherms were measured at 77 K with Micromeritics Tristars 3000 analyzer. Before

measurements, the samples were degassed in a vacuum at 180°C for at least 6 h. The Brumauer-Emmett-Teller (BET) method was utilized to calculate the specific surface areas (SBET) using adsorption data in a relative pressure range of 0.04 to 0.2. The pore volume and pore size distributions were derived from the adsorption branches of isotherms by using the Barrett-Joyner-Halenda (BJH) model.

6.3 Results

6.3.1 The effect of synthesis temperature and time on the morphology of spherical mesoporous alumina

The precursor of different synthesis temperature and synthesis time, and XRD pattern (Figure 6.1) showed that the precursor prepared under synthesis temperature of 120°C and 140°C were mainly amorphous products I and II when the reaction time was 3 h. When the temperature increased to 160°C and 180°C and reaction time was kept at 3h, precursor III and IV began to crystallize and became AlO(OH). The results indicate that the synthesis temperature has significant effect on the crystallization of precursor, as under a lower solution temperature, the system energy is too low to promote the formation and transformation of crystals. Therefore, the samples tend to become amorphous. As the solution temperature increased, diffraction peaks were produced, and the intensity and the width of diffraction peaks became larger, which indicates the crystallinity of the particles becomes stronger. At the temperature 140°C, with synthesis time greater than 3 h, (precursor V and VI) crystallization starts. At these reaction times, when the synthesis temperature increases, the average crystalline length increases (III and IV). Reaction at

lower temperature reduced the size of the crystals. By controlling the synthesis temperature and time, it was possible to control the morphology and crystal structure of products.

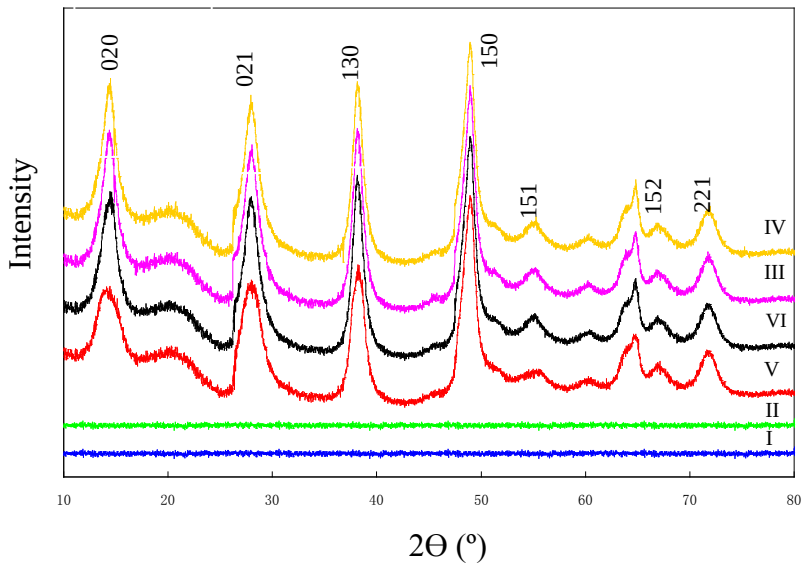

Figure 6.1: Precursor XRD patterns under different synthesis conditions
(I) Amorphous (120°C-3 h), (II) Amorphous (140°C-3 h), (III) AlO(OH) (160°C-3 h), (IV) AlO(OH) (180°C-3 h), (V) AlO(OH) (140°C-9 h), (VI) AlO(OH) (140°C-15 h).

Figure 6.2 shows the mesoporous alumina XRD pattern after calcination at 600°C. Sample I and II are both amorphous alumina. The amorphous precursor I and II prepared at a lower synthesis temperature transform into γ-Al_2O_3 under calcination at 600ºC, sample III, IV, V and VI are γ-Al_2O_3. With the increase of solution temperature, the position of each diffraction peak does not change, but the intensity and width of the diffraction peak become larger, which means that the crystallinity of particle becomes stronger gradually.

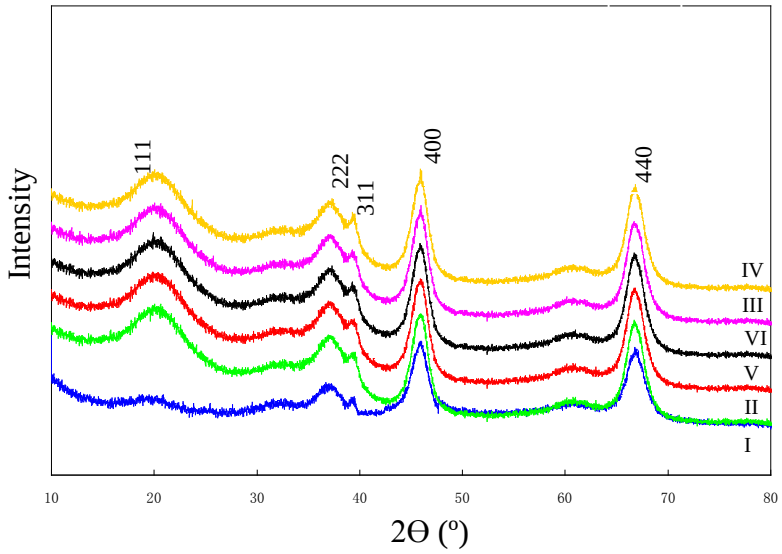

Figure 6.2: Mesoporous Alumina XRD patterns under different synthesis conditions after calcination at 600°C (I) Al_2O_3(120°C-3 h), (II) Al_2O_3 (140°C-3 h), (III) Al_2O_3 (160°C-3 h), (IV) Al_2O_3 (180°C-3 h), (V) Al_2O_3 (140°C-9 h), (VI) Al_2O_3 (140°C-15 h).

Figure 6.3 shows the SEM images of mesoporous alumina samples (calcined at 600ºC) prepared under different synthesis conditions. It can be seen from the figure that the synthesis temperature has a great effect on the shape of the sample, and spherical particle formed at 140ºC. When the temperature was 120ºC, the sample particles were spherical and massive (Figure 6.3 (a)); when the temperature reached 140ºC, the sample particles were regular spherical with smooth surface, and the particle size was between 50 nm and 200 nm (Figure 6.3 (b)). With the increase of synthesis temperature, a lot of particles began to crystallize and formed crystalline solids. They completely transformed into γ-Al_2O_3 when they are calcined at 600ºC, but the amorphous precursor required more energy to promote a phase transformation at 600ºC, thus, crystallization was relatively slow. Besides, when the synthesis temperature was high, gum arabic powder carbonized partly, a section of the

template was lost. This was not favorable for the development and shaping of spherical particles.

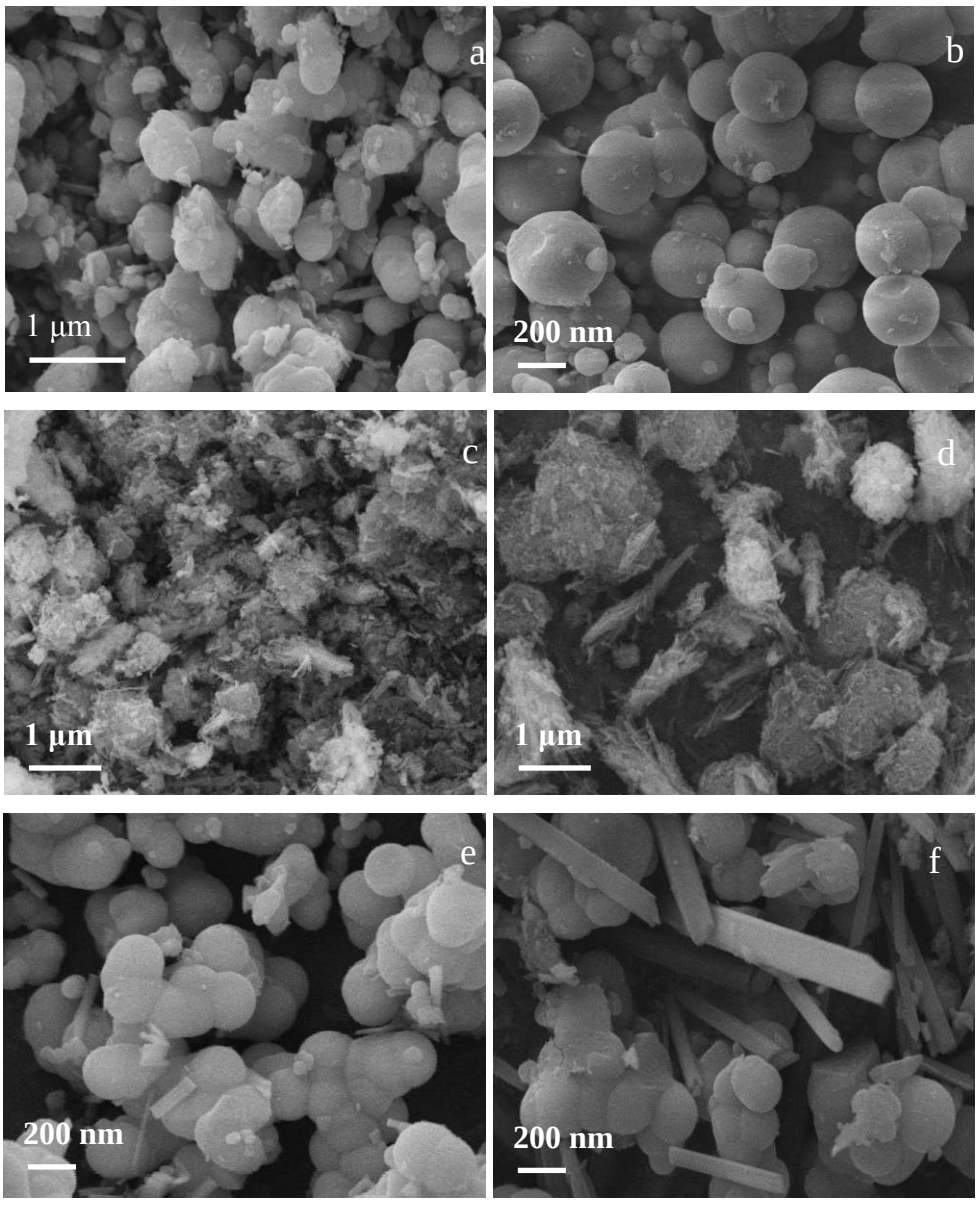

Figure 6.3: SEM images of mesoporous alumina samples (calcined at 600ºC) prepared under different synthesis conditions (a) Al_2O_3 (120°C-3 h), (b) Al_2O_3 (140°C-3 h), (c) Al_2O_3 (160°C-3 h), (d) Al_2O_3 (180°C-3 h), (e) Al_2O_3 (140°C-9 h), (f) Al_2O_3 (140°C-15 h).

In this case, the sample transformed into irregular and flocculent particles, gathering together (Figure 6.3 (c)-(d)). Longer synthesis time is also not conducive to the development of spherical alumina particles (Figure 6.3 (e)-(f)), because it is easy to develop flocculent, strip and irregular particles, affecting the normal development and growth of spherical particles. The results showed that 140°C reaction temperature and 3 h contact time was suitable to produce spherical mesoporous nano-alumina particles.

6.3.2 The Effect of GA/P123 Weight Ratio on of Spherical Morphology

During the synthesis, the amount of the additive has a very important influence on the morphology and structure of the sample. Table 6.1 shows the test results of spherical mesoporous alumina prepared by different GA/P123 weight ratio (samples VII-XI). Figure 6.4 shows the pore size distribution and the SEM images for the different alumina samples (VII - XI).

Table 6.1: Textural properties of mesoporous alumina with different GA/P123 weight ratio

Sample number	Weight ratio （GA/P123）	Pore size (nm)	Pore volume (cm^3/g)	BET surface area (m^2/g)
VII	0	7.0	0.04	99
VIII	1	7.6	0.17	143
IX	2	7.6	0.30	159
X	3	8.6	0.30	184
XI	4	5.1	0.23	138

The GA/urea was maintained at 1.25 based on the study on the single template. The results showed that the average pore size, pore volume as well as BET surface area were the maximum for GA/P123 ratio of 3 (sample X). The major criteria for the mesoporous

alumina are high pore size, pore volume and surface area. Thus, it was possible to produce good quality mesoporous alumina with GA/P123 ratio of 3.

When GA/P123 weight ratio is 0, the samples were strips and heaped up irregularly and had an extremely small number of mesoporous structure. In addition, the major pore types were of inkbottle type with large opening and small diameter, and uneven crack-like pores. The average pore size was around 7 nm.

As the weight ratio gradually increased (1 to 3), average pore size increased from 7.6 to 8.6 nm and pore volume increased from 0.17 to 0.3 cm^3/g. When the weight ratio reached 3, the sample formed regular, uniform and monodisperse microspheres. The pore structure is mainly regular cylindrical with uniform size and shape, and pore sizes are mostly distributed between 7 nm and 9 nm. The average pore size increased to 8.6 nm and pore volume increased to 0.3 cm^3/g and BET surface area increased to 184 m^2 /g.

As the weight ratio increased to 4, the spherical particles started agglomerating. The average pore size decreased to 5.1 nm, the pore volume decreased to 0.23 cm^3/g, and the BET surface area dropped to 138 m^2/g. The main reason is that with the increase of the weight ratio, the viscosity of the solution also increased. When the viscosity is too high, it will weaken the homogeneous nucleation leading to agglomeration at different sites. Based on the results, the GA/P123 ratio was used as 3 to produce spherical mesoporous alumina nanoparticles.

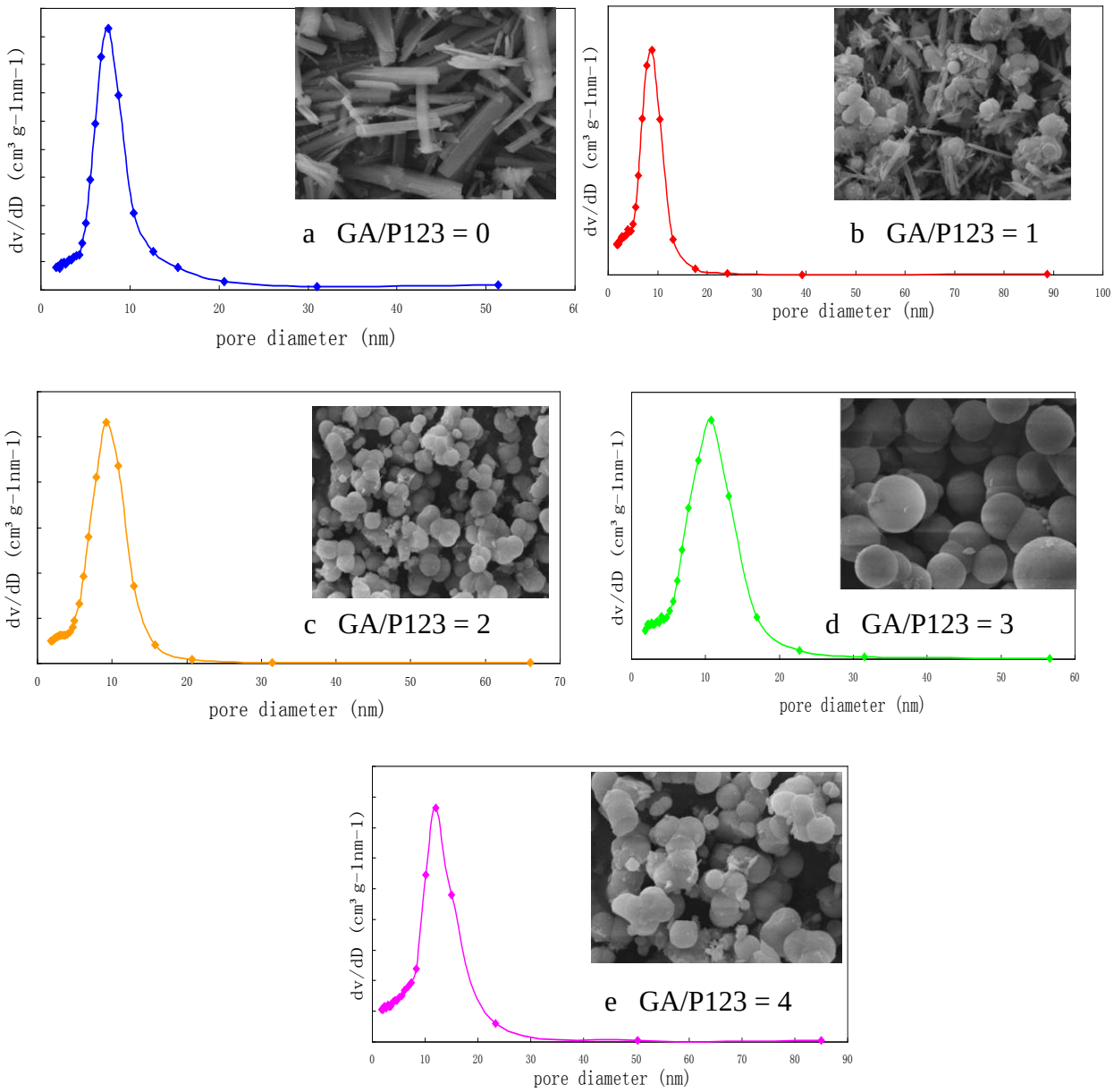

Figure 6.4: Pore size distributions and corresponding SEM images of the alumina particles (samples VII-XI) with different GA/P123 weight ratios

Based on the results, it was found that temperature of 140°C, contact time of 3h, GA/P123 ratio of 3 and GA/urea ratio of 1.25 were suitable to produce spherical mesoporous alumina nanoparticles by the double template method. The alumina particles

obtained by the double template method was calcined at 600°C for 2 h to remove the template and produce the spherical mesoporous alumina nanoparticles.

6.3.3 Spherical Mesoporous Alumina

Adapting the double template method, with GA/P123 weight ratio being 3, the spherical mesoporous alumina was successfully prepared with identical morphology, good dispersion and uniform pore size. In the synthesis of the precursor, the amorphous precursor can be prepared under a lower temperature of 140ºC and shorter contact time of 3 h. When this kind of precursor calcines at 600°C, it is easier for inorganic Al^{3+} to slowly interact with and then connect to interface of organic micelles through electrostatic interactions. It covers the whole surface of the aluminum ions, so the growth rate of the various surfaces become consistent, and homogeneous nucleation forms spherical particles. At the same time, uniform mesoporous layer forms at the particle surface completely transferring it into spherical mesoporous Al_2O_3, as shown in Figure 6.5.

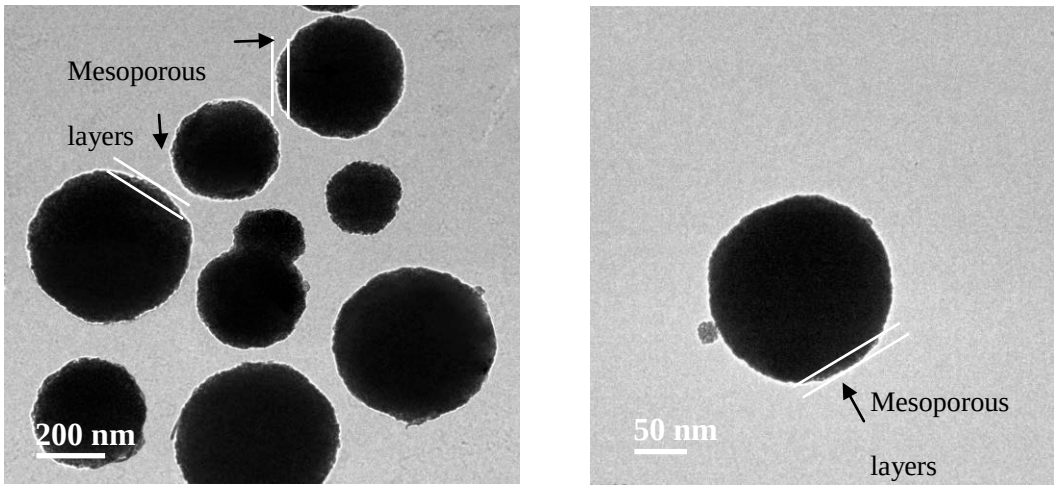

Figure 6.5: TEM images of the spherical mesoporous alumina materials

Figure 6.5 shows the TEM images of spherical mesoporous alumina particles. It can be seen in this figure that the alumina particles have regular spherical form and good dispersion. There is a 10 nm mesoporous layer on alumina particle surface. The mesopore size is identical, uniform covering the surface of the alumina particles.

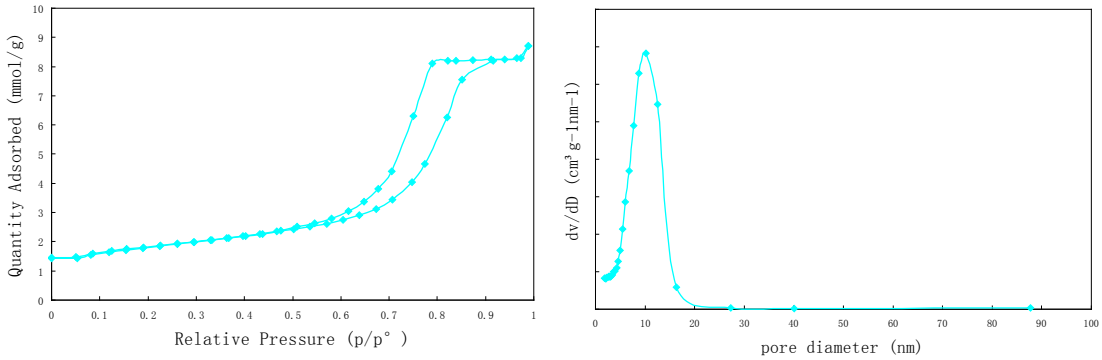

Figure 6.6: Nitrogen sorption isotherms and corresponding pore size distribution of the spherical mesoporous alumina materials

The results of nitrogen sorption isotherms and corresponding pore size distributions of the spherical mesoporous alumina materials (GA/P123=3) are shown in Figure 6.6. The nitrogen sorption isotherms are typical type IV curves and have H1 hysteresis loop. This is a signature for mesoporous materials and the reason for this hysteresis is the capillary condensation. Nitrogen molecules are adsorbed on the surface of the particles because of the force exerted on them by the walls of the pores. In mesoporous materials, nitrogen molecules are adsorbed layer by layer. They fill the higher energy sites near pore walls and then low energy sites away from walls. When molecules accumulate on two opposing walls, they get close enough to each other and collapse into a thermodynamically lower energy state. This process is called capillary condensation. When the pressure is reduced during

desorption, the molecules at low energy do not try to leave their place, so they need higher gradient of chemical potential (or pressure drop) to pull the adsorbed molecules out of their sites. Hence, the same molecules desorb at lower pressure. This gap between equilibrium adsorption and desorption pressures is the cause of hysteresis, and indicates that the alumina particles are mesoporous. The size, shape and thickness are uniform, pore diameter is mainly in the range of 9-11 nm; average pore size has increased 10 nm, and pore volume has increased to 0.5 cm^3/g; BET surface has larger area of 257 m^2/g.

Chapter 7

Advanced applications of the 5N alumina nanoparticles in different fields

7.1 Introduction

Currently the most commonly used LED substrate material, sapphire crystal has developed rapidly in recent years because of its excellent optical, chemical, and other properties. In the global market of LED substrate, two-inch sapphire wafers are widely used. The heat exchange method is a crystal growth technique used for large sapphires. In 1970, Schmid and Viechnicki [21] first grew sapphire crystals using the heat exchange method. The heat exchanger is used to remove heat, causing a longitudinal temperature gradient since the temperature is cold at the bottom and warm at the top of the crystal growth area. The temperature gradient is controlled by regulating the rate of gas flow in the heat exchanger (helium gas used as cooling source), as well as the heating power level. In this manner, the pressed alumina bulks are melted in the crucible at around 1800^{o}C and the sapphire crystal is slowly solidified by helium gas, which removes the heat from the crystal. The heat exchange method requires high-quality raw materials in order to form a stable temperature field during the crystal growth process. The segregation coefficient of the impurities in the melted crystal is controlled to be less than 1. Impurities will therefore be continuously discharged into the melted crystal from the solid-liquid interface and distributed to the outer layer of the surface where the crystals come into contact with the crucible wall.

Preparation of Al_2O_3 sapphire crystals using spherical as well as other morphologies of nano-Al_2O_3 particles with high level of purity (5N) are presented in this chapter. Ten sapphire crystals were produced for the each intermediate Al_2O_3 with a particular morphology. The average length of crystal rods produced was calculated using the total length of crystal rods obtained from each crystal. This is used to determine the influence of different intermediate Al_2O_3 morphologies on sapphire growth carried out with the heat exchange method.

7.2 Preparation of alumina particles as a precursor for sapphire crystal growth

The spherical alumina nanoparticles, obtained by the single template method for different reaction temperatures and contact time, were calcined to 1800ºC. As Figure 7.1 shows, after calcination at 1800ºC, the diffraction peak was sharp and regular. This indicates that the α-alumina had a single crystal phase, crystal growth was highly ordered, and crystallinity was good. All the samples were transformed into α-phase alumina. The α-alumina (of different morphologies, see Figure 5.3), obtained after calcination at 1800ºC, was used as the raw material in the sapphire growth process using the heat exchange method. The performance and yield of the sapphire will be presented in Section of 7.3.

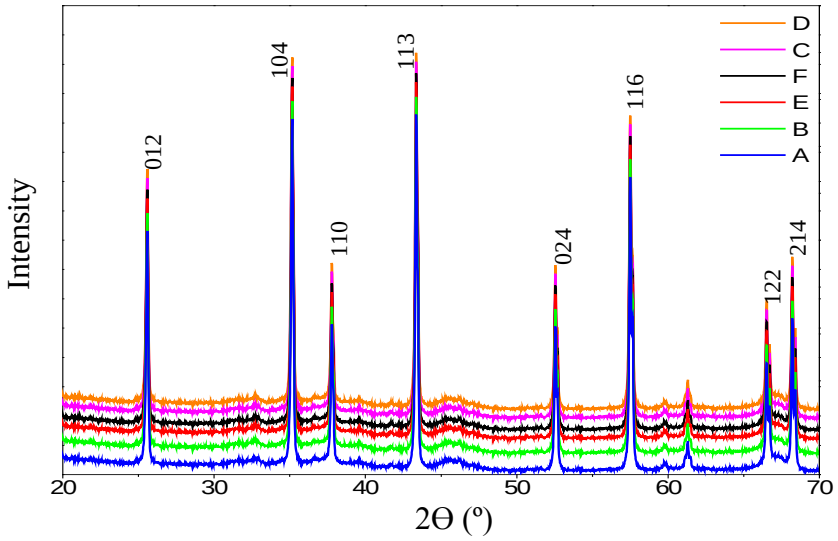

Figure 7.1: XRD patterns of alumina used as sapphire crystal raw material under different synthesis conditions after calcination at 1800°C (A) Al_2O_3-120°C-3 h, (B) Al_2O_3-140°C-3 h, (C) Al_2O_3-160°C-3 h, (D) Al_2O_3-180°C-3 h, (E) Al_2O_3-140°C-9 h, (F) Al_2O_3-140°C-15 h.

7.3 Application of Spherical Alumina on Sapphire Growth Using the Heat Exchange Method

As described earlier, Al_2O_3 raw material was produced using nano-alumina powder (by single template method using different reaction temperatures and contact time followed by heating at 600ºC). The Al_2O_3 particles had the same purity but different morphologies (samples A-F) after calcination at 1800°C (Figure 7.2). The calcined alumina (at 1800ºC) was used as the raw material for sapphire growth using the heat exchange method. A single crystal often consists of a distribution of regions which are highly oriented. The polycrystalline material consists of single crystals described above but of very small sizes

of the order of micrometers but randomly distributed when there is no preferred orientation. The scattering of X-rays by atoms is the point to be considered in that case. When there is periodic arrangement of atoms the X-rays (single crystals) will be scattered only in certain directions when they hit the formed lattice planes (formed by atoms). This will cause high intensity peaks (the width of the peaks is small for single crystals but also depends on other variables). For polycrystalline materials X-rays will be scattered in many directions leading to a large bump distributed in a wide range (2Θ) instead of high intensity narrower peaks.

Figure 7.2 shows the effect of intermediate Al_2O_3 with different shapes on the total length of sapphire crystal rods. The results indicated that the length of crystal rods produced by rod-like, rod-like and partially spherical, or partially massive and partially spherical intermediates was relatively short. The average length was about 3200 nm to 3800 mm. As it can be seen from this figure, there was a large standard deviation in the length of crystal rods, which means that the length of crystal rods varies significantly. However, the length of the crystal rods produced using the spherical intermediate was relatively stable at around 4000 mm. From the experimental results, it was found that for the same purity, the morphology of the raw materials had a significant influence on the total length and the length stability of sapphire crystal rods produced using the heat exchange method. The sapphire crystal rods and wafers were tested to evaluate their quality (refractive index, crystal defect, and impurity content).

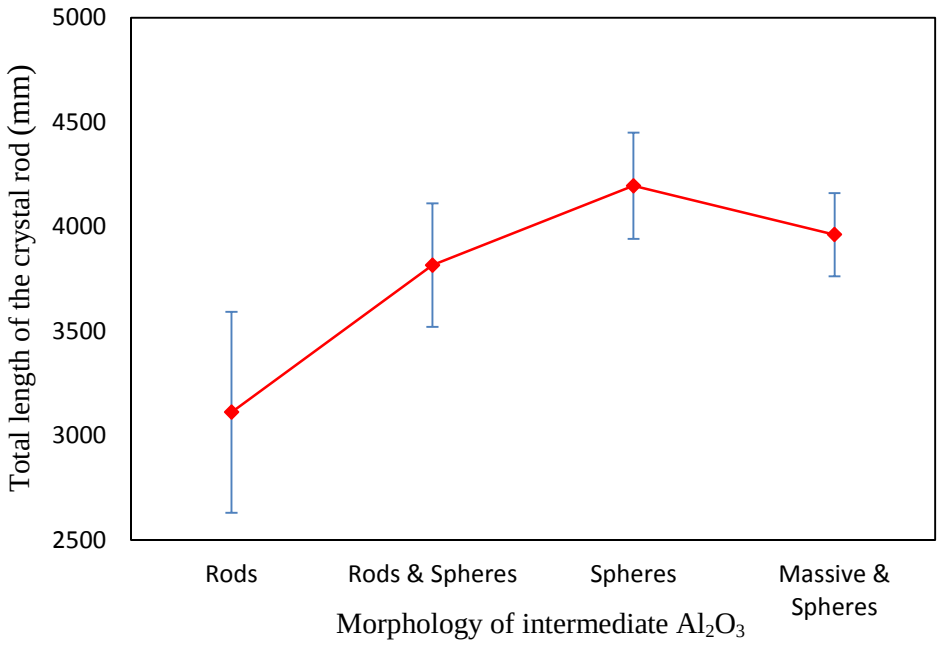

Figure 7.2: Relationship between the intermediate Al_2O_3 with different shapes and the total length of sapphire crystal rods

(a) (b) (c)

Figure 7.3: (a) Sapphire crystal (115 kg， diameter=380 mm, height=245 mm), (b) Sapphire crystal rods (Φ34), (c) Sapphire wafers (2 inches).

Figure 7.3 shows the sapphire crystals, sapphire crystal rods, and wafers produced during the experiment.

As it can be seen from Figure 7.4, the XRD test results show that the c-plane (0001) sapphire crystal wafer had a steep diffraction peak value when the 2ɵ angle was 41.6623°, indicating that the crystal rod had a complete sapphire crystal structure.

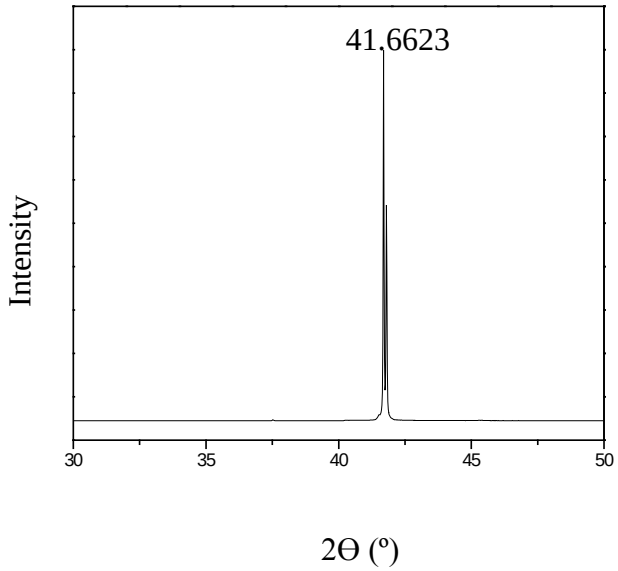

Figure 7.4: XRD pattern of sapphire c-plane (0001) crystal rods

Figure 7.5 shows the transmission spectrum for sapphire c-plane (0001) wafers. The transmittance of wafer through 300-400 nm, the ultraviolet range, was more than 80%; transmittance through 500-1000 nm was over 85%. These results indicate that by using the spherical alumina nanoparticles prepared using the gum arabic (GA) template as the raw material for sapphire growth and using the heat exchange method, sapphire crystal products of high quality and stable rod length can be produced. Similar peaks were observed by other researchers [127, 128].

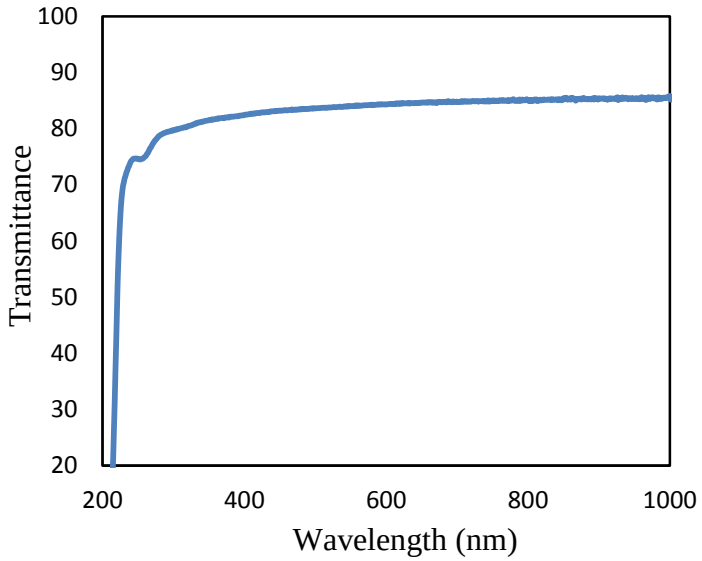

Figure 7.5: Sapphire c-plane (0001) wafer transmission spectrum

7.4 Photoacoustic (PA) tomography

Photoacoustic imaging as a novel non-invasive imaging technique provides convenience for studying real-time semi-quantitative pharmacokinetic and biodistribution profiles of drugs or probes to determine whether they can reach the target areas and their metabolic pathways. Nano-gold particles absorb light energy and convert it to acoustic energy. Thus, chitosan-capped star (AuNS) and rod shaped (AuNR) gold nanoparticles and multispectral optoacoustic tomography (MSOT) (Figure 7.6) were used to visualize the AuNS in the blood vessels, liver, spleen and kidneys of a mouse in real time. The successful application of the gold nanoparticles in PA tomography was published (Appendix III). The efficiency of the gold nanoparticles can be enhanced by embedding the gold nanoparticles in a mesoporous alumina matrix. Thus, further studies

were done on the production of gold doped mesoporous alumina. Future studies are required on the application of those doped mesoporous alumina in PA tomography.

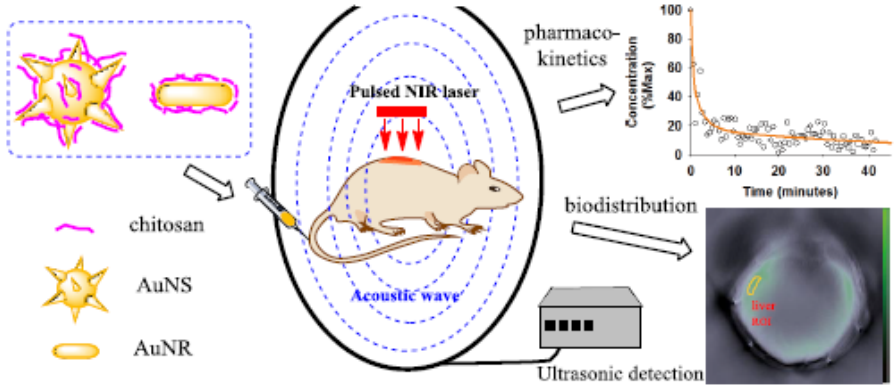

Figure 7.6: Schematic illustration of pharmacokinetic and biodistribution analysis of chitosan-capped gold nanoparticles by MSOT

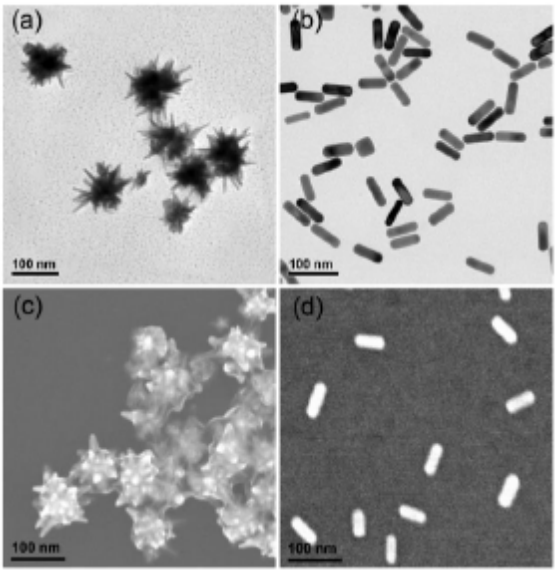

Figure 7.7: TEM and SEM images of AuNS and AuNR particles

Figure 7.7 shows the TEM and SEM images of AuNS and AuNR particles. A preliminary study was performed using gold nanoparticles. The results of the study were published (see Appendix II). The synthesis of the gold nanoparticles has been described in Appendix III. The same method was followed to prepared gold doped mesoporous alumina particles. In this method the reaction was performed in the mesoporous matrix of the alumina particles. Figure 7.8 shows the TEM pictures of modified alumina nanoparticles doped with gold nanoparticles. These particles can be used for PA tomography. The matrix in the picture shows the mesoporous alumina particles. The black structures represent star shaped gold nanoparticles.

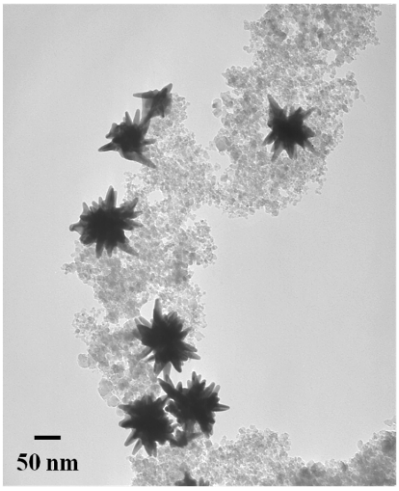

Figure 7.8: TEM micrograph of modified alumina nanoparticles doped with gold nanoparticles

Chapter 8

Conclusions and Recommendations

8.1 Conclusions

High purity alumina (HPA) is becoming an important inorganic raw material which finds applications in different fields. In this work, ultra-pure spherical and mesoporous spherical nano-sized alumina particles have been produced from wastewater. The method is "green and environment-friendly" as aluminum (in the form of alumina) from wastewater is recovered.

The efficiency of chelating reagents such as PX-17, SX-1, and 13X molecular sieve for removing impurities from wastewater under different pH have been studied. Based on the efficiency of the different reagents, an alum solution of 99.999% purity was produced from wastewater using PX-17 and SX-1. This alum solution was converted to boehmite solution using ammonia solution. In this study, the focus was not only on removing the impurities from wastewater, but also on producing high-purity alumina powder with desired particle size and uniform the particle size distribution.

The boehmite solution was used to produce 99.999% pure spherical nano-alumina particles by the single template method. Spherical nano-scale alumina particles of 50 nm to 300 nm size with good dispersion and uniform morphology were obtained with a 1.25 gum arabic/urea weight ratio. It was noted that the precursor prepared at a lower temperature of

140^{o}C for a shorter period of time (3 h), compared to other temperatures and times used, in the synthesis had a better morphology for forming spherical particles. When this type of precursor calcined at 600^{o}C, the inorganic Al^{3+} was more likely to interact and connect with the organic micelle interface through electrostatic interactions, covering the entire surface of aluminum ions so that all surfaces had the same growth speed. Homogeneous nucleation occurred and spherical particles were prepared. These alumina particles were converted to α-alumina particles and used to produce sapphire crystals. The experimental results also showed that the different morphologies of the raw materials had a major influence on the yield and quality of sapphire crystal rods. Spherical alumina nanoparticles prepared using this method could produce sapphire crystal rods with a total length between 4000 mm and 4500 mm and a high transmittance rate of 85%. The method developed and the results obtained have led to the development of a new template method for controlling the morphology of sapphire crystal materials, and more importantly, they have opened a new avenue for research on raw materials for use in growing sapphire crystals.

Using gum arabic and P123 as double template, nano-scale spherical mesoporous alumina has been successfully synthesized using the alum/boehmite solution. The mesoporous alumina produced has good thermal stability (treated under 700ºC), a high specific surface area of 257 m^2/g, a large pore size of 10 nm, and a pore volume of 0.5 cm^3/g. In the synthesis, temperature, time, and weight ratio of additives have a significant influence on the morphology of the samples. It was noted that using the lower synthesis temperature of 140ºC, the short reaction time of 3 h, and the template weight ratio of 3 facilitates the formation of monodisperse particles with spherical shape (150 nm - 400 nm)

and uniform mesoporous structure. The results of this method and the research not only contributed to the development of mesoporous alumina, but also provided a new double templating method for a better control of pore size and structure. These mesoporous nano-alumina particles were doped with gold nanoparticles to produce particles that can be used as the target material for photoacoustic tomography. The study on the use of gold nanoparticles as the target material for photoacoustic tomography has already been published (Appendix II).

8.2 Recommendations

The work should be continued on the advanced applications of different morphologies of alumina nanoparticles in order to further develop alumina-based high value-added products.

The spherical mesoporous alumina prepared through double template method presents new possibilities for application in the field of macromolecular transport, catalysis, adsorption, and so on, which enriches the diversity in solution phase synthetic bio-chemistry. These applications should also be explored.

REFERENCES

1. Shi, H., & Xia, S. (2007). Preparation of PAC from Aluminum Foil Pickling Waste Liquid and Its Application. *Chinese Journal of Environmental Science and Technology,* 30 (3), 22-23.

2. Rajendran, S. (1994). Production of ultrafine alpha alumina powders and fabrication of fine grained strong ceramics. *Journal of Materials Science*, 29(21), 5664-5672.

3. Krell, A., & Ma, H. (1999). Nanocorundum-advanced synthesis and processing. *Nanostructured Materials*, 11(8), 1141-1153.

4. Ma, H. W., & Krell, A. (2002). Synthesis and processing of nano-α- Al_2O_3 powders. *Key Engineering Materials*, 206-213, 43-46.

5. Krell, A., & Ma, H. (2003). Performance of alumina membranes from new nanosynthesis in ultrafiltration and nanofiltration. *Journal of the American Ceramic Society*, 86(2), 241-246.

6. Bagwell, R. B., Messing, G. L., & Howell, P. R. (2001). The formation of α- Al_2O_3 from θ- Al_2O_3: the relevance of a "critical size" and: diffusional nucleation or "synchro-shear"?. *Journal of Materials Science*, 36(7), 1833-1841.

7. Zhang, H., Shan, G., Liu, H., & Xing, J. (2007). Preparation of (Ni/W)-γ- Al_2O_3 microspheres and their application in adsorption desulfurization for model gasoline. *Chemical Engineering Communications*, 194(7), 938-945.

8. Bartsch, M., Saruhan, B., Schmücker, M., & Schneider, H. (1999). Novel low-temperature processing route of dense mullite ceramics by reaction sintering of amorphous SiO_2-coated γ-Al_2O_3 particle nanocomposites. *Cheminform*, 82(6), 1388-1392.

9. Lietti, L., Forzatti, P., Nova, I., & Tronconi, E. (2001). NOx storage reduction over Pt-Ba/γ- Al_2O_3 catalyst. *Journal of Catalysis*, 204(17), 175-191.

10. Kim, S. M., Lee, Y. J., Bae, J. W., Potdar, H. S., & Jun, K. W. (2008). Synthesis and characterization of a highly active alumina catalyst for methanol dehydration to dimethyl ether. *Applied Catalysis A General*, 348(1), 113-120.

11. Seri, O., & Kamazawa, R. (2012). Preparation of flake alumina by corrosion of aluminum in methanol. *Journal of the Japan Society of Powder & Powder Metallurgy*, 59(6), 307-310.

12. Kim, K. T., Dao, T. D., Han, M. J., Anjanapura, R. V., & Aminabhavi, T. M. (2015). Graphene coated with alumina and its utilization as a thermal conductivity enhancer for alumina sphere/thermoplastic polyurethane composite. *Materials Chemistry & Physics*, 153, 291-300.

13. Ianoş, R., Lazău, I., & Păcurariu, C. (2009). The influence of combustion synthesis conditions on the α-Al_2O_3, powder preparation. *Journal of Materials Science*, 44(4), 1016-1023.

14. Seyed Ali Hosseini, Aligholi Niaei, & Dariush Salari. (2011). Production of γ-alofrom kaolin. Open Journal of Physical Chemistry, 01(2), 23-27.

15. Dabbagh, H. A., & Shahraki, M. (2013). Mesoporous nano rod-like γ-alumina synthesis using phenol–formaldehyde resin as a template. *Microporous & Mesoporous Materials*, 175, 8-15.

16. Feng, J. T., Lin, Y. J., Feng, L., Evans, D. G., & Li, D. Q. (2007). Preparation, structure and properties of micro-spherical alumina with magnetic spinel ferrite cores. *Applied Catalysis A General*, 329(10), 112-119.

17. Lv, Y., Li, D., Tang, P., & Feng, Y. (2015). A simple and promoter free way to synthesize spherical γ-Alumina with high hydrothermal stability. *Materials Letters*, 155, 75-77.

18. Wu, Q., Zhang, F., Yang, J., Li, Q., Tu, B., & Zhao, D. (2011). Synthesis of ordered mesoporous alumina with large pore sizes and hierarchical structure. *Microporous & Mesoporous Materials*, 143(2-3), 406-412.

19. Saúl, C., El, H. J., & Jaime, A. (1999). Surfactant - Assisted Synthesis of Mesoporous Alumina Showing Continuously Adjustable Pore Sizes. *Advanced Materials*, 11(5), 379-381.

20. Xin, Y., Jiang, P., Yu, M., Gu, H., Li, Q., & Zhang, Z. (2014). A universal route to fabricate hierarchically ordered macro/mesoporous oxides with enhanced intrinsic activity. *Journal of Materials Chemistry A*, 2(18), 6419-6425.

21. Viechnicki, D., & Schmid, F. (1974). Crystal growth using the heat exchanger method (hem). *Journal of Crystal Growth*, 26(1), 162-164.

22. Peters, R., Kränkel, C., Petermann, K., & Huber, G. (2008). Crystal growth by the heat exchanger method, spectroscopic characterization and laser operation of high-purity Yb:Lu_2O_3. *Journal of Crystal Growth*, 310(7-9), 1934-1938.

23. Lu, C. W., & Chen, J. C. (2001). Numerical computation of sapphire crystal growth using heat exchanger method. *Journal of Crystal Growth*, 225(2-4), 274-281.

24. Wu, M., Zhao, W., Liu, L., Yang, Y., Ma, W., & Wang, Y. (2014). Effects of crucible cover on heat transfer during sapphire crystal growth by heat exchanger method. *Journal of Crystal Growth*, 404(404), 130-135..

25. Schmid, F., Khattak, C. P., & Smith, M. B. (1984). Growth of bismuth germanate crystals by the heat exchanger method. *Journal of Crystal Growth*, 70(1), 466-470.

26. Digne, M., Sautet, P., Raybaud, P., Toulhoat, H., & Artacho, E. (2002). Structure and stability of aluminum hydroxides: a theoretical study. *Journal of Physical Chemistry B*, 106(20), 5155-5162.

27. Tang, G., Zhang, C., Sun, C., Yan, B., Yang, G., Dai, W., & Tian, B. (2011). Research progress of γ-Alumina support. *Chemical Industry & Engineering Progress*, (08), 1756-1765.

28. Li, W., Shi, E., & Yin, Z. (1999). Growth habit of crystal and the shape of coordination polyhedron. *Journal of Synthetic Crystal*, 28(4), 368-372.

29. Zheng, Y., Shi, E., Li, W., Wang, B., & Hu, X. (1998). Research and development of the theories of crystal growth. *Journal of Inorganic Materials*, 14(3), 321-332.

30. Zhang, Y., Wang, Y., & Yan, Y. (2002). Development and application of hydrothermal method in growing low-dimensional artificial crystal. *Bulletin of the Chinese Ceramic Society*, 21(3), 22-26.

31. Tian, M., Shi, E., Zhong, W., Pang, W., & Guo, J. (1998). Nano ceramics and nano ceramic powder. *Journal of Inorganic Materials*, 2, 129-137.

32. Shi, E., Xia, C., Wang, B., & Zhong, W. (1996). Application and development of hydrothermal method. *Journal of Inorganic Materials*, 2, 193-206.

33. Li, Y., Peng, C., Zhao, W., Bai, M., & Rao, P. (2014). Morphology evolution in hydrothermal synthesis of mesoporous alumina. *Journal of Inorganic Materials*, 29(10), 1115-1120.

34. Ray, J. C., You, K. S., Ahn, J. W., & Ahn, W. S. (2007). Synthesis of mesoporous alumina using anionic, nonionic and cationic surfactants. *Studies in Surface Science & Catalysis*, 165(07), 275-278.

35. Zhang, Z., Shen, Z., Ling, F., & Xia, C. (2013). Impacts of sodium nitrate additive on alumina morphology. *Petroleum Processing and Petrochemicals*, 44(9), 47-50.

36. Pramod. K. S., Jilavi, M. H., Burgard. D., & Nass, R. (2005). Hydrothermal synthesis of nanosize alpha-Al_2O_3 from seeded aluminum hydroxide. *Journal of the American Ceramic Society*, 81(10), 2732-2734.

37. Shi, E., Xia, C., Wang, B., & Zhong, W. (1996). Application and development of hydrothermal method. *Journal of Inorganic Materials*, 2, 193-206.

38. Mikhailov, V. I., Maslennikova, T. P., & Krivoshapkin, P. V. (2014). Materials based on aluminum and iron oxides obtained by the hydrothermal method. *Glass Physics & Chemistry*, 40(6), 650-656.

39. Hou, H., Xie, Y., Yang, Q., Guo, Q., & Tan, C. (2005). Preparation and characterization of γ-AlO(OH) nanotubes and nanorods. *Nanotechnology*, 16(6), 741.

40. Buining, P. A., Pathmamanoharan, C., Jansen, J. B. H., & Lekkerkerker, H. N. W. (1991). Preparation of colloidal boehmite needles by hydrothermal treatment of aluminum alkoxide precursors. *Journal of the American Ceramic Society*, 74(6), 1303-1307.

41. Wang, J., Zhang, B., & Xu, X. (2007). Influence of hydrothermal temperature on structural and microstructural properties of boehmite. *Nonferrous Metals: Extractive Metallurgy*, 5, 23-26.

42. Varma, H. K., Mani, T. V., Damodaran, A. D., Warrier, K. G. K., & Balachandran, U. (1994). Sol–spray preparation, particulate characteristics, and sintering of alumina powders. *Advanced Materials I*, 11-14.

43. Li, J., Pan, Y., Xiang, C., Ge, Q., & Guo, J. (2006). Low temperature synthesis of ultrafine α-Al2O3 powder by a simple aqueous sol–gel process. *Ceramics International*, 32(5), 587-591.

44. Ning, G. L., Chang, Y. F., Liu, Y. L., Fei, T., & Yuan, L. (2002). Shape-controlled synthesis of alumina nanoparticles by carboxy-containing organic molecules. *Chemical Research in Chinese Universities*, 23(3), 345-348.

45. Masouleh, N. S. G., Taghizadeh, M., & Yaripour, F. (2014). Optimization of effective sol-gel parameters for the synthesis of mesoporous γ-Al_2O_3, using experimental design. *Chemical Engineering & Technology*, 37(9), 1475-1482.

46. Ji, X., Tang, S., Gu, L., Liu, T., & Zhang, X. (2015).Synthesis of rod-like mesoporous γ-Al_2O_3 by an ionic liquid-assisted sol–gel method. *Materials Letters*, 151, 20-23.

47. Kim, T. W., Kleitz, F., Paul, B., & Ryoo, R. (2005). Mcm-48-like large mesoporous silicas with tailored pore structure: facile synthesis domain in a ternary triblock copolymer-butanol-water system. *Journal of the American Chemical Society*, 127(20), 7601-7610.

48. Moriguchi, I., Ozono, A., Mikuriya, K., Teraoka, Y., Kagawa, S., & Kodama, M. (1999). Micelle-templated mesophases of phenol-formaldehyde polymer. *Chemistry Letters*, 11, 1171-1172.

49. Dong, A., Ren, N., Tang, Y., Wang, Y., Zhang, Y., & Weiming Hua, A. (2003). General synthesis of mesoporous spheres of metal oxides and phosphates. *Journal of the American Chemical Society*, 125(17), 4976-4977.

50. Firouzi, A., Kumar, D., Bull, L. M., Besier, T., Sieger, P., & Huo, Q., et al. (1995). Cooperative organization of inorganic-surfactant and biomimetic assemblies. *Science*, 267(5201), 1138-43.

51. Huo, Q., Margolese, D. I., Ciesla, U., Feng, P., Gier, T. E., & Sieger, P. (1994). Generalized synthesis of periodic surfactant/inorganic composite materials. *Nature*, 368(6469), 317-321.

52. Zhou, M., Wei, Z., Qiao, H., Zhu, L., Yang, H., & Xia, T. (2009). Particle size and pore structure characterization of silver nanoparticles prepared by confined arc plasma. *Journal of Nanomaterials*, (4), 3.

53. Johansson, E. M., Córdoba, J. M., & Odén, M. (2010). Effect of heptane addition on pore size and particle morphology of mesoporous silica SBA-15. *Microporous & Mesoporous Materials*, 133(1-3), 66-74.

54. Innocenzi, P., & Malfatti, L. (2013). Mesoporous thin films: properties and applications. *Chemical Society Reviews*, 42(9), 4198-4216.

55. Boissiere, C., Grosso, D., Lepoutre, S., Nicole, L., Bruneau, A. B., & Sanchez, C. (2005). Porosity and mechanical properties of mesoporous thin films assessed by environmental ellipsometric porosimetry. *Langmuir the Acs Journal of Surfaces & Colloids*, 21(26), 12362-12371.

56. Nielsch, K., Choi, J., Schwirn, K., And, R. B. W., & Gösele, U. (2002). Self-ordering regimes of porous alumina: the 10 porosity rule. *Nano Letters*, 2(7), 677.

57. Tamon, H., Ishizaka, H., Yamamoto, T., & Suzuki, T. (1999). Preparation of mesoporous carbon by freeze drying. *Carbon*, 37(12), 2049-2055.

58. Nan, R., & Yi, T. (2005). Template-induced assembly of hierarchically ordered zeolite materials. *Petrochemical Technology*, 34(4), 405-411.

59. Masuda, H., & Fukuda, K. (1995). Ordered metal nanohole arrays made by a two-step replication of honeycomb structures of anodic alumina. *Science*, 268(5216), 1466.

60. Jie, S., Liu, L. L., Yang, R. M., & Zhang, P. X. (2008). Anodic aluminum oxide template with large area and small holes prepared by gradual voltage-rising method. *Nanotechnology & Precision Engineering*, 6(5), 322-326.

61. Liu, K., Du, K., Chen, J., Zhou, L., Zhang, L., & Fang, Y. (2010). Fabrication of high quality ordered porous anodic aluminum oxide templates. *Qiangjiguang Yu Lizishu/high Power Laser & Particle Beams*, 22(7), 1531-1534.

62. Fu, J., Cherevko, S., & Chung, C. H. (2008). Electroplating of metal nanotubes and nanowires in a high aspect-ratio nanotemplate. *Electrochemistry Communications*, 10(4), 514-518.

63. Zhuo, H., Peng, F., Lin, L., Qu, Y., & Lai, F. (2011). Optical properties of porous anodic aluminum oxide thin films on quartz substrates. *Thin Solid Films*, 519(7), 2308-2312.

64. Ren, X., Senapati, K., Jiang, W. T., & Jiang, C. H. (2010). Formation of ordered TiO_2 nanostructural arrays with tunable shapes by magnetron sputtering method. *Materials Chemistry & Physics*, 126(1), 1-5.

65. Öztürk, S., Kılınç, N., Taşaltın, N., & Öztürk, Z. Z. (2012). Fabrication of ZnO nanowires and nanorods. *Physica E: Low-dimensional Systems and Nanostructures*, 44(6), 1062-1065.

66. Wu, J. T., Chang, W. Y., & Yang, S. Y. (2010). Fabrication of a nano/micro hybrid lens using gas-assisted hot embossing with an anodic aluminum oxide (AAO) template. *Journal of Micromechanics & Microengineering*, 20(7), 669-672.

67. Cui, J., Wu, Y., Wang, Y., Zheng, H., Xu, G., & Zhang, X. (2012). A facile and efficient approach for pore-opening detection of anodic aluminum oxide membranes. *Applied Surface Science*, 258(14), 5305-5311.

68. Loh, P. Y., Lee, K. K., Ng, Y., Sow, C. H., & Chin, W. S. (2014). Co/Al layered double hydroxides nanostructures: a binderless electrode for electrochemical capacitor. *Electrochemistry Communications*, 43, 9-12.

69. Maleak, N., Potpattanapol, P., Bao, N. N., Ding, J., Wongkokuo, W., & Tang, I. M. (2014). Fabrication and magnetic properties of electrodeposited ni/cu nanowires using the double bath method. J*ournal of Magnetism & Magnetic Materials*, 354(3), 262-266.

70. Li, F., Zhang, L., & Metzger, R. (1998). On the growth of highly ordered pores in anodized aluminum oxide. *Chemistry of materials*, 9(10), 2470-2480.

71. Sun, L., Zong, R. L., & Zhou, J. (2005). Synthesis of ZnS nanowires by DC electrodeposition in AAO template. *Journal of Sichuan University*, 42(2), 435-437.

72. Lu, Q., Feng, G., Komarneni, S., & Mallouk, T. (2004). Ordered SBA-15 nanorod arrays inside a porous alumina membrane. *Journal of the American Chemical Society*, 126(28), 8650-8651,

73. Forrer, P., Schlottig, F., Siegenthaler, H., & Textor, M. (2000). Electrochemical preparation and surface properties of gold nanowire arrays formed by the template technique. *Journal of Applied Electrochemistry*, 30(5), 533-541.

74. Li, H. Q., Luo, J. Y., Zhou, X. F., Yu, C. Z., & Xia, Y. Y. (2007). An ordered mesoporous carbon with short pore length and its electrochemical performances in supercapacitor applications. *Journal of the Electrochemical Society*, 154(154), A731-A736.

75. Liu, X., Zhou, L., Li, J., Sun, Y., Su, W., & Zhou, Y. (2006). Methane sorption on ordered mesoporous carbon in the presence of water. *Carbon*, 44(8), 1386-1392.

76. Vinu, A., Hossain, K. Z., Kumar, G. S., & Ariga, K. (2006). Adsorption of l - histidine over mesoporous carbon molecular sieves. *Carbon*, 44(3), 530-536.

77. Wen, Z., Liu, J., & Li, J. (2008). Core/Shell Pt/C nanoparticles embedded in mesoporous carbon as a methanol-tolerant cathode catalyst in direct methanol fuel cells. *Advanced Materials*, 20(4), 743-747.

78. Su, F., Zeng, J., & Bao, X. (2005). Preparation and characterization of highly ordered graphitic mesoporous carbon as a Pt catalyst support for direct methanol fuel cells. *Chemistry of Materials*, 17(15), 3960-3967.

79. Zhou, Y., Ko, S., Lee, C. W., Pyo, S. G., Kim, S. K., & Yoon, S. (2013). Enhanced charge storage by optimization of pore structure in nanocomposite between ordered mesoporous carbon and nanosized WO_{3-x}. *Journal of Power Sources*, 244(4), 777-782.

80. Liu, L., Deng, Q. F., Bao, A., Ren, T. Z., Liu, Y. P., & Bao, Z. (2012). Synthesis of ordered mesoporous carbon materials and their catalytic performance in dehydrogenation of propane to propylene. *Catalysis Today*, 186(1), 35-41.

81. Vinu, A., Ariga, K., Mori, T., Nakanishi, T., Hishita, S., & Golberg, D., et al. (2005). Preparation and characterization of well-ordered hexagonal mesoporous carbon nitride . *Advanced Materials*, 17(13), 1648-1652.

82. Tang, C., Bombalski, L., Kruk, M., Jaroniec, M., Matyjaszewski, K., & Kowalewski, T. (2010). Nanoporous carbon films from “hairy” polyacrylonitrile-grafted colloidal silica nanoparticles. *Advanced Materials*, 20(8), 1516-1522.

83. Tamai, H., Kakii, T., Hirota, Y., Kumamoto, T., & Yasuda, H. (1996). Synthesis of extremely large mesoporous activated carbon and its unique adsorption for giant molecules. *Chemistry of Materials*, 8(2), 454-462.

84. Pekala, R. W., & Schaefer, D. W. (1993). Structure of organic aerogels. 1. Morphology and scaling. *Macromolecules*, 26(20), 5487-5493.

85. Rui, Z., Lu, Y., Liang, Z., Liang, X., Wu, G., & Ling, L. (2003). Monolithic carbon aerogels from sol-gel polymerization of phenolic resoles and methylolated melamine. *Carbon*, 41(8), 1660-1663.

86. Zhang, R., Li, W., Li, K., Lu, C., Zhan, L., & Ling, L. (2004). Effect of concentration of reactants on porosity of hydrogels, organic and carbon aerogels. *Microporous & Mesoporous Materials*, 72(1-3), 167-173.

87. Wang, H., Yin, X., Long, Y., & Kong, A. (2014). Discussion on one step synthesis of mesoporous carbon materials. *Experimental Technology & Management*, 31(6), 48-53.

88. Roggenbuck, J., & Tiemann, M. (2005). Ordered mesoporous magnesium oxide with high thermal stability synthesized by exotemplating using CMK-3 carbon. *Journal of the American Chemical Society*, 127(4), 1096-1097.

89. Roggenbuck, J., Günter Koch, A., & Tiemann, M. (2006). Synthesis of mesoporous magnesium oxide by CMK-3 carbon structure replication. *Chemistry of Materials*, 18(17), 4151-4156.

90. Sakthivel, A., Huang, S. J., Chen, W. H., Lan, Z. H., Chen, K. H., & Kim, T. W. (2004). Replication of mesoporous aluminosilicate molecular sieves (RMMS) with zeolite framework from mesoporous carbons (CMKS). *Chemistry of Materials*, 16(16), 3168-3175.

91. Yang, Z., Xia, Y., & Mokaya, R. (2004). Zeolite ZSM-5 with unique supermicropores synthesized using mesoporous carbon as a template. *Advanced Materials*, 16(16), 727-732.

92. Kai, Z. (2006). Study on preparation of monodisperse polystyrene microspheres with designable size. *Ion Exchange & Adsorption*, 22(2), 140-145.

93. Fu, X., Lin, L., Wang, D., Hu, Z., & Song, C. (2004). Preparation of CdS hollow spheres using poly-(styrene–acrylic acid) latex particles as template. *Colloids & Surfaces A Physicochemical & Engineering Aspects*, 262(1-3), 216-219.

94. Wan, Y., Shi, Y., & Zhao, D. (2007). Designed synthesis of mesoporous solids via nonionic-surfactant-templating approach. *Chemical Communications*, 38(9), 897.

95. Lu, A. H., & Schüth, F. (2006). Nanocasting: A versatile strategy for creating nanostructured porous materials. *Advanced Materials*, 18(14), 1793-1805.

96. Lee, J., Kim, J., & Hyeon, T. (2011). Recent progress in the synthesis of porous carbon materials. *Advanced Materials*, 18(16), 2073-2094.

97. Lu, Y. (2006). Surfactant-templated mesoporous materials: from inorganic to hybrid to organic. *Angewandte Chemie International Edition*, 7(45), 7664-7667.

98. Wan, Y., Haifeng Yang, A., & Zhao, D. (2006). "Host−Guest" chemistry in the synthesis of ordered nonsiliceous mesoporous materials. *Accounts of Chemical Research*, 39(7), 423-432.

99. Huo, Q., Margolese, D. I., Ciesla, U., Feng, P., Gier, T. E., & Sieger, P. (1994). Generalized synthesis of periodic surfactant/inorganic composite materials. *Nature*, 368(6469), 317-321.

100. Islam, M. F., Rojas, E., Bergey, D. M., Johnson, A. T., & Yodh, A. G. (2003). High weight fraction surfactant solubilization of single-wall carbon nanotubes in water. *Nano Letters*, 3(2), 269-273.

101. Zhao, D., Yang, P., Huo, Q., Chmelka, B. F., & Stucky, G. D. (1998). Topological construction of mesoporous materials. *Current Opinion in Solid State & Materials Science*, 3(1), 111-121.

102. Lin, H. P., & Mou, C. Y. (2002). Structural and morphological control of cationic surfactant-templated mesoporous silica. *Accounts of Chemical Research*, 35(11), 927.

103. Wang, L., & Liao, S. (1998). Liquid crystal chemistry. *Science Press*, 138-149.

104. Zhang, X., Zhu, W., Cai, Q., Cao, M., Liu, Y., & Long, Y. (2011). A size-controllable preparation of monodispers emesoporous SiO_2 microspheres. *Journal of Functional Materials*, 42, 803-808.

105. Wang, X., Zhou, B., & Xu, Z. (2006). Preparation and TiO_2 assembly of high ordered mesoporous carbon films. *Atomic Energy Science and Technology*, 40, 55-60.

106. Chao, M. C., Wang, D. S., Lin, H. P., & Mou, C. Y. (2003). Control of single crystal morphology of SBA-1 mesoporous silica. *Journal of Materials Chemistry*, 13(12), 2853-2854.

107. Hwang, Y. K., Chang, J. S., Kwon, Y. U., & Park, S. E. (2004). Microwave synthesis of cubic mesoporous silica SBA-16. *Microporous & Mesoporous Materials*, 68(1), 21-27.

108. Li, R., Yu, L., & Jia, L. (2013). Biomimetic synthesis of different morphology Cu_2O induced by using polymer as template. *Chinese Journal of Inorganic Chemistry*, 2(29), 265-270.

109. Yu, C. Z., Fan, J., & Zhao, D. Y. (2002). Block copolymer synthesis of high-quality cubic, large pore mesoporous millimeter spheres in the presence of inorganic salts. *Acta Chimica Sinica*, 60(8), 1357-1360.

110. Wang, Z., Zhang, J., Ekman, J. M., Kenis, P. J., & Lu, Y. (2010). DNA-mediated control of metal nanoparticle shape: one-pot synthesis and cellular uptake of highly stable and functional gold nanoflowers. *Nano Letters*, 10(5), 1886-1891.

111. Zhang, C., Wang, J., & Hu, R. (2015). Biotemplated systhesis of porous and hierarchy SnO_2 and sensitivity property for ethanol. *New Chemical Materials*, 1(43), 99-101.

112. Li, W., & Zhao, D. (2013). An overview of the synthesis of ordered mesoporous materials. *Chemical Communications*, 49(10), 943.

113. Jana, N. R., Gearheart, L., & Murphy, C. J. (2001). Seed-Mediated growth approach for shape-controlled synthesis of spheroidal and rod-like gold nanoparticles using a surfactant template. *Advanced Materials*, 13(13), 1389-1393.

114. Zhao, D., Huo, Q., Feng, J., Chmelka, B. F., & Stucky, G. D. (1998). Nonionic Triblock and Star Diblock Copolymer and Oligomeric Surfactant Syntheses of Highly Ordered, Hydrothermally Stable, Mesoporous Silica Structures. *Journal of the American Chemical Society*, 120(24), 6024-6036.

115. Kao, H. C., & Wei, W. C. (2000). Kinetics and microstructural evolution of heterogeneous transformation of θ-Alumina to α-Alumina. *Journal of the American Ceramic Society*, 83(2), 362-368.

116. Sarikaya, Y., İsmet Sevinç, & Akinç, M. (2001). The effect of calcination temperature on some of the adsorptive properties of fine alumina powders obtained by emulsion evaporation technique. *Powder Technology*, 116(1), 109-114.

117. Ceresa, E. M., Gennaro, A., & Cortesi, P. (1989). Alpha-alumina in the form of spherical non-aggregated particles having a narrow size distribution and sizes below 2 microns and process for preparing same. US, US4818515.

118. Kass, M. D., & Cecala, D. M. (1997). Enhanced sinterability of alumina particles by pretreating in liquid ammonia. *Materials Letters*, 32(2-3), 55-58.

119. Bousquet, C., Elissalde, C., Aymonier, C., Maglione, M., Cansell, F., & Heintz, J. M. (2007). Tuning Al_2O_3 crystallinity under supercritical fluid conditions: effect on sintering. *Journal of the European Ceramic Society*, 28(1), 223-228.

120. Shek, C. H., Lai, J. K. L., Gu, T. S., & Lin, G. M. (1997). Transformation evolution and infrared absorption spectra of amorphous and crystalline nano-Al_2O_3 powders. *Nanostructures Materials*, 8(5), 605-610.

121. Xie, Z. P., Lu, J. W., Gao, L. C., Li, W. C., Xu, L. H., & Wang, X. D. (2003). Influence of different seeds on transformation of aluminum hydroxides and morphology of alumina grains by hot-pressing. *Materials & Design*, 24(3), 209-214.

122. Li, J.G., & Sun, X. (2000). Synthesis and sintering behavior of a nanocrystalline α-Al_2O_3 powder. *Acta Materialia*, 48(12), 3103-3112.

123. Karagedov, G.R., & Lyakhov, N. Z. (1999). Preparation and sintering of nano-sized α-Al_2O_3 powder. *Nanostruetured Materials*, 11(99), 559-572.

124. Strekopytov, S., & Exley, C. (2006). Thermal analyses of aluminum hydroxide and hydroxyaluminosilieates. *Polyhedron*, 25(8), 1707-1713.

125. Liu, H., Ning, G., Gan, Z., & Lin, Y. (2008). Emulsion-based synthesis of unaggregated, spherical alpha alumina. *Materials Letters*, 62(10), 1685-1688.

126. Bagwell, R.B., Messing, G.L., & Howell, P.R. (2001). The formation of α- Al_2O_3 from θ-Al_2O_3: The relevance of a "critical size" and: Diffusional nucleation of "synchro-shear". *Journal of Materials Science*, 36(7), 1833-1841.

127. Cheng, J., Agrawal, D., Zhang, Y., & Roy, R. (2002). Microwave sintering of transparent alumina. *Materials Letters*, 56(4), 587-592.

128. Anderson, J. M., Czigány, Z., Jin, P., & Halverson, U. (2004). Microstructure of α-alumina thin films deposited at low temperatures on chromia template layers. *Journal of Vacuum Science & Technology A: Vacuum, Surfaces, and Films*, 22(1), 117-121.

PUBLICATIONS

1. **Xie, Y.**, Kocaefe, D., Kocaefe, Y., Chen, C., & Cheng, S. (2016). Double Templating Synthesis of Nanoscale - Spherical Mesoporous Alumina. *Journal of Materials Chemistry A*, manuscript no TA-ART-08-2016-007466 (Submitted)

2. **Xie, Y**., Duygu, K., Yasar, K., Cheng, J., & Wei, L. (2016). The effect of novel synthetic methods and parameters control on morphology of nano-alumina particles. *Nanoscale Research Letters*, 11(1), 1-11.

3. **Xie, Y.**, Kocaefe, Y., Kocaefe, Y., & Kocaefe, Y. (2016). Review of research on template methods in preparation of nanomaterials. *Journal of Nanomaterials*, 8, 11.

4. Wang, J †., **Xie, Y. †**, Wang, L., Tang, J., Li, J., Kocaefe, D., Kocaefe, Y., Zhang, Z., Li, Y., & Chen, C. (2015). In vivo pharmacokinetic features and biodistribution of star and rod shaped gold nanoparticles by multispectral optoacoustic tomography. Rsc Advances, 5(10), 7529-7538.

APPENDIX I

Xie et al. Nanoscale Research Letters (2016) 11:259
DOI 10.1186/s11671-016-1472-z

Nanoscale Research Letters

NANO REVIEW Open Access

The Effect of Novel Synthetic Methods and Parameters Control on Morphology of Nano-alumina Particles

Yadian Xie[1,2], Duygu Kocaefe[1*], Yasar Kocaefe[1], Johnathan Cheng[2] and Wei Liu[3*]

Abstract

Alumina is an inorganic material, which is widely used in ceramics, catalysts, catalyst supports, ion exchange and other fields. The micromorphology of alumina determines its application in high tech and value-added industry and its development prospects. This paper gives an overview of the liquid phase synthetic method of alumina preparation, combined with the mechanism of its action. The present work focuses on the effects of various factors such as concentration, temperature, pH, additives, reaction system and methods of calcination on the morphology of alumina during its preparation.

Keyword: Alumina, Particle morphology, Reaction mechanism, Calcination method

Review

Introduction

Different materials are essential for the social development. Generally, certain material structure and morphology are required for their applications in a specific field. Inorganic materials are an important branch of materials, which promote development of science and technology. Alumina is an inexpensive and widely used inorganic material. It has a complex structure and many crystalline polymorphic phases such as α-Al_2O_3, β-Al_2O_3, γ-Al_2O_3, δ-Al_2O_3, θ-Al_2O_3, η-Al_2O_3, κ-Al_2O_3, χ-Al_2O_3 and ρ-Al_2O_3. The phase transition temperatures are different for different precursors during their calcination as shown in Fig. 1 [1].

Among the numerous crystal forms of alumina, α-Al_2O_3 and γ-Al_2O_3 are the two most common kinds. α-Al_2O_3 has some excellent physical and chemical properties such as good acid, alkali and heat resistances and high hardness and strength. It is widely used in different fields such as ceramics, surface protective layer materials, refractory materials, catalysts and catalyst supports and optical materials [2–5]. γ-Al_2O_3, which is also called activated alumina, has a large surface area, strong adsorption capacity, good catalytic activity and wear resistance. It is also widely applied in various fields such as adsorbents [6], ceramics [7], catalysts and catalyst supports [8].

The application performance of alumina depends on not only the size of ultra-fine particles but also the particle shape [9–11]. Alumina has a variety of shapes such as rod [12], fibrous structure [13], flake [14] and sphere [15]. Different shapes of alumina have different physical and chemical properties and applications. For example, the fibrous nano-alumina has a very strong anti-sintering property [16], which is often used as an additive for epoxy resin to improve its tensile strength and rigidity. The flake-like alumina is generally used as a seed crystal added to ceramics, which significantly enhances the toughness of ceramics [17].

Alumina is a common catalyst support, whose pore structure is closely related to the activity, selectivity and lifetime of the catalyst. Alumina is divided into different categories such as microporous alumina, mesoporous alumina and macroporous alumina according to its pore size. The pore size of mesoporous alumina is between 2 and 50 nm. It is a rigid porous material with a mutually interconnected or isolated network structure. It has not only the characteristics of a crystalline phase of alumina but also the characteristics of a porous material.

* Correspondence: duygu_kocaefe@uqac.ca; cjlw@gznu.edu.cn
[1]Department of Applied Science, University of Quebec at Chicoutimi (UQAC), Chicoutimi, Quebec G7H2B1, Canada
[3]School of Architectural & Material Engineering, Guizhou Normal University, Guiyang, Guizhou 550001, China
Full list of author information is available at the end of the article

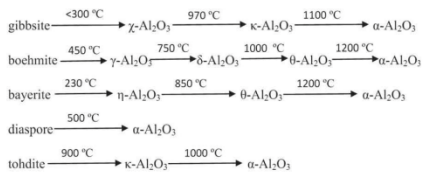

Fig. 1 Phase transformation of alumina

Mesoporous alumina is widely used in the catalysis [18], adsorption [19] and other fields due to its adjustable pore structure, relatively large internal and external surface area and pore volume.

The morphology, purity, surface acidity and hydrothermal stability, the pore structure and other properties restrict the application of alumina. The research is ongoing on the pore structure, surface acidity and hydrothermal stability [20]. Morphology, as one of the important parameters of particle characterization, has a substantial effect on the properties and applications of the products. The morphology of particles is influenced and controlled by its crystallization habit during the preparation using liquid-phase method [21, 22], which is restricted by the environment and the growth conditions. This article reviews the research carried out on the preparation of alumina starting from the liquid-phase method for its synthesis including its mechanism and discusses the effect of different factors such as reactant concentration, temperature, pH, additives, system environment and calcination methods on the micromorphology of particles.

Liquid-Phase Method for Synthesis of Alumina

There are some common liquid-phase methods for synthesis of alumina, such as sol-gel method, hydrothermal method, template method, precipitation method, emulsion method or microemulsion method and electrolysis method. Alumina with different morphologies can be obtained by using different synthesis methods and optimizing the reaction conditions.

Hydrothermal Method Hydrothermal method is an approach where the mixed solution is poured into a sealed reactor. Utilization of the relatively high temperature in the reactor and the high-pressure growth environment promotes the dissolution and recrystallization of poorly soluble or insoluble material. Hydrothermal methods include hydrothermal synthesis, hydrothermal treatment and hydrothermal reactions. During the hydrothermal process, the crystal grows to its largest possible size under the non-restricted conditions and its characteristics (various shapes, high degree of crystallinity, small size, uniform distribution, lighter particle agglomeration, etc.) form [23, 24]. The development of crystal face and the morphology of the crystal formed by hydrothermal synthesis are closely related to the hydrothermal conditions such as water temperature, pressure and the permittivity and viscosity and diffusion coefficient of the solution. The same type of crystal can be produced with different morphology under different hydrothermal conditions [25].

Li et al. [26] let ammonium aluminum sulfate, dispersant PEG2000 and urea disperse in deionized (DI) water and stirred them vigorously to form a solution. Then, the mixed solution was poured into a stainless steel pressure reactor with a teflon-lining. By changing the temperature of the water, mesoporous alumina with different morphologies was obtained. In the course of the reaction, the following reactions take place:

$$\mathrm{CO(NH_2)_2 + H_2O \rightarrow CO_2 + 2NH_3} \quad (1)$$

$$\mathrm{NH_3 + H_2O \rightarrow NH_4 + OH^-} \quad (2)$$

$$\mathrm{Al^{3+} + 3OH^- \rightarrow AlOOH + H_2O} \quad (3)$$

As Fig. 2a shows, when the temperature is 90 °C, the particles obtained are different size spheres. As it is shown in Fig. 2b, at the temperature of 120 °C, the particles are superfine fiber-shaped. As Fig. 2c shows, massive fiber-shaped particles are obtained at the temperature of 150 °C. The crystal orientation is dependent on the temperature which affects the growth rate of the crystal face; consequently, the morphology can be controlled by regulating the temperature. These results indicate that the morphology of the particles substantially changes with the increasing water temperature [27].

Zhao et al. [28] prepared flat hexagonal-shaped nano-alumina by hydrothermal synthesis, using aluminum nitrate as aluminum source and sodium nitrate as additive. During the reaction, the Na^+ of sodium nitrate was adsorbed onto the surface, which hindered the accumulation of Al^{3+} and OH^- ions. This affected the appearance of the particles. By changing the amount of sodium nitrate additive to control the growth of certain crystal face of alumina, hexagon-shaped alumina with different parameters was obtained. When the amount of sodium nitrate was 0.2 mol, the width of the particle was reduced and its length and thickness remained unchanged. When sodium nitrite was 0.4 and 0.6 mol, the thickness increased and the length and width remained unchanged. The hexagon-shaped particles were gradually transformed into thicker particles as the sodium nitrate concentration increased as shown in Fig. 3.

Depending on different reaction systems, particles have accordingly different crystal habits. Pramod K. Sharma's group and Shi's group [29, 30] synthesized needle-like and plate-like α-Al_2O_3, respectively, in water

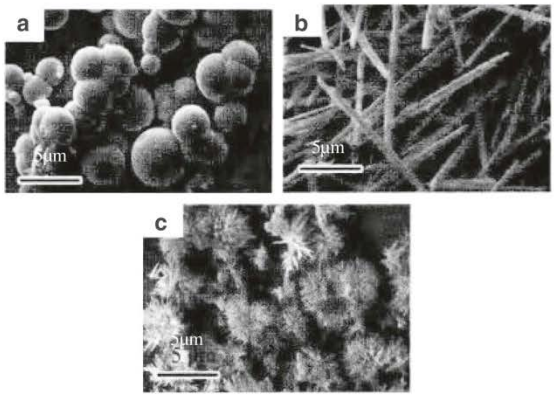

Fig. 2 TEM image of alumina prepared under different synthetic temperatures. **a** 90 °C. **b** 120 °C. **c** 150 °C

and alcohol-water reaction systems by hydrothermal treatment method using $Al(OH)_3$ colloid as precursor, as shown in Fig. 4.

Mikhailov et al. [31] prepared hexagonal flake-shaped γ-Al_2O_3 by hydrothermal method with $Al_2(SO_4)_3{\cdot}18H_2O$ and ammonia as raw materials. This study has shown that pH of solution has a significant impact on the morphology of precursor. Under acidic conditions, the H^+ in solution will bind with the hydroxyl, which is on the surface of the γ-AlOOH layered structure, thereby destroying this structure, eventually forming a rod-like nanostructure by rolling growth mechanism [32]. On the contrary, under alkaline conditions, it retains its layered structure, forming plate-shaped nanostructure. Figure 5 shows that when pH is 5, the product is rod-like; when pH is 7, the product is transformed from rod-like to plate-shaped nanostructure; when pH is 9, the product has hexagonal shape. Boehmite converts into a γ-Al_2O_3 in the firing process, but its shape and size do not change [33, 34]. Calcining the plate-like precursor at 600 °C for 4 h resulted in the original hexagonal γ-Al_2O_3 with basically same size.

Sol-Gel Method The sol-gel method refers to inorganic or organic alkoxide dispersed in solution. Using the transparent sol formed by hydrolysis and condensation of the precursor, a gel with certain structure is formed during the aging process by the aggregation between the gel particles. During the sol-gel process, the microstructure of the material is controlled and cut at the

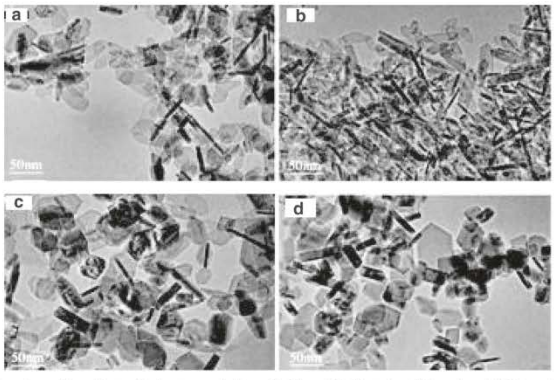

Fig. 3 TEM image of nano-alumina with sodium nitrate concentration of **a** 0 mol, **b** 0.2 mol, **c** 0.4 mol and **d** 0.6 mol

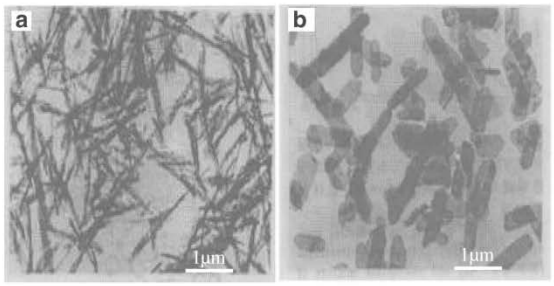

Fig. 4 TEM image of α-Al_2O_3. **a** Needle-like α-Al_2O_3. **b** Plate-like α-Al_2O_3

mesoscopic level by means of low-temperature chemical method, which changes the morphology and structure of the particles [35, 36].

Ning et al. [37], using AcOH as additive and adopting two-step alkoxide hydrolysis sol-gel method, synthesized spherical and fibrillar Al_2O_3 nano-powder in organic phase. The results showed that the amount of AcOH has a decisive effect on the morphology of the particles. As the amount of AcOH increased, the shape of the particles gradually shifted from the fibrillar to the spherical shape, as shown in Fig. 6. During the reaction, AcOH and other organic molecules containing functional groups N, O and S (ethylacetoacetate, polyamide carboxylic acid salt) as additives coordinate with inorganic ion or are adsorbed onto the surface of crystal nucleus, which changes the growth rate of crystal face. This leads to the change in the morphology of particles.

Masouleh's group and Ji' group [38, 39], using aluminum isopropoxide as aluminum source, [Bmim] PF6 as ionic liquid and adopting sol-gel method to change the molar ratio of [Bmim] PF6 and aluminum isopropoxide, successfully synthesized uniform rod-like mesoporous γ-Al_2O_3. This study has shown that ionic liquid plays a very important role in the morphology of products. As it is shown in Fig. 7, with the molar ratio of [Bmim]PF6, aluminum isopropoxide increases from 0 to 0.18; the morphology of the products shows a highly homogeneous rod shape. When the molar ratio of [Bmim]PF6 and aluminum isopropoxide is 0.18, the morphology of the products with rod shape has the best homogeneity. If this ratio exceeds 0.18, it is not conducive enough to form the rod shape.

Template Method Template method is a cutting-edge technology developed in the 1990s. It is widely applied in recent years, and it is an effective synthetic method for controlling the structure, particle size and morphology of materials through a utilization of template. Depending on the differences in template structure, template method can be divided into two groups called hard and soft template methods.

Hard Template In hard template method, precursor is uniformly dispersed in the pore of the hard template or

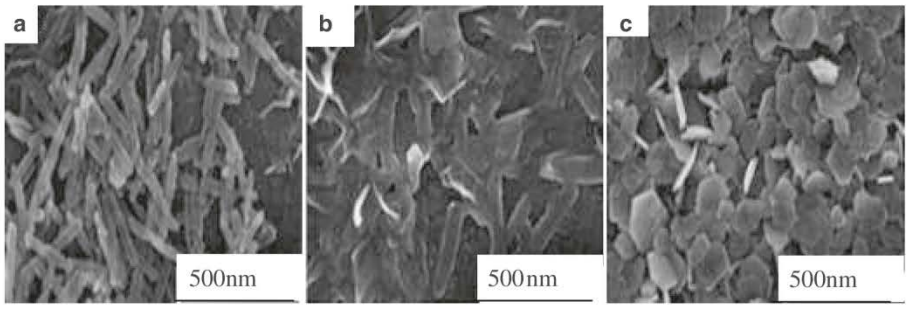

Fig. 5 TEM image of γ-AlOOH. **a** pH = 5. **b** pH = 7. **c** pH = 9

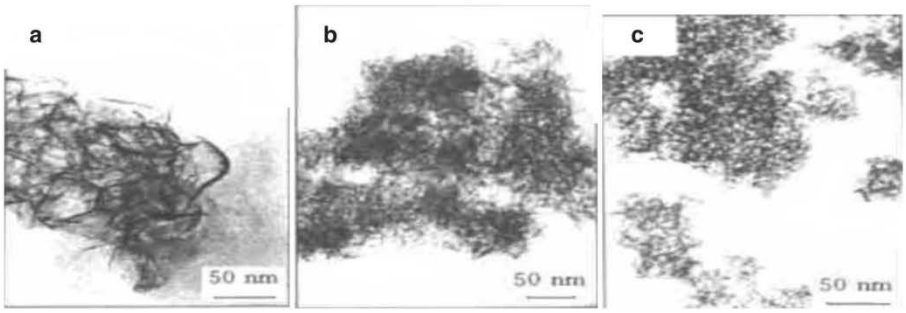

Fig. 6 TEM image of alumina nanoparticles with different amount of AcOH. **a** No AcOH. **b** m(AcOH)/m[Al(Opri)$_3$] < 0.05. **c** m(AcOH)/m[Al(Opri)$_3$]≈0.1

absorbed onto its surface, thereby converting it into a complex product. Then, by choosing an appropriate method (dissolution, sintering, etching, etc.), the target product can be obtained. The special structure of hard template restricts the crystallization or polymerization of the precursor during the process of synthesis, which leads to formation of a mesoscopic phase with an opposite-phase structure of the template.

The hard template is often used as a microreactor during the synthesis. The type of hard template and the reaction conditions such as concentration of reactants, time of immersion, temperature of immersion and the

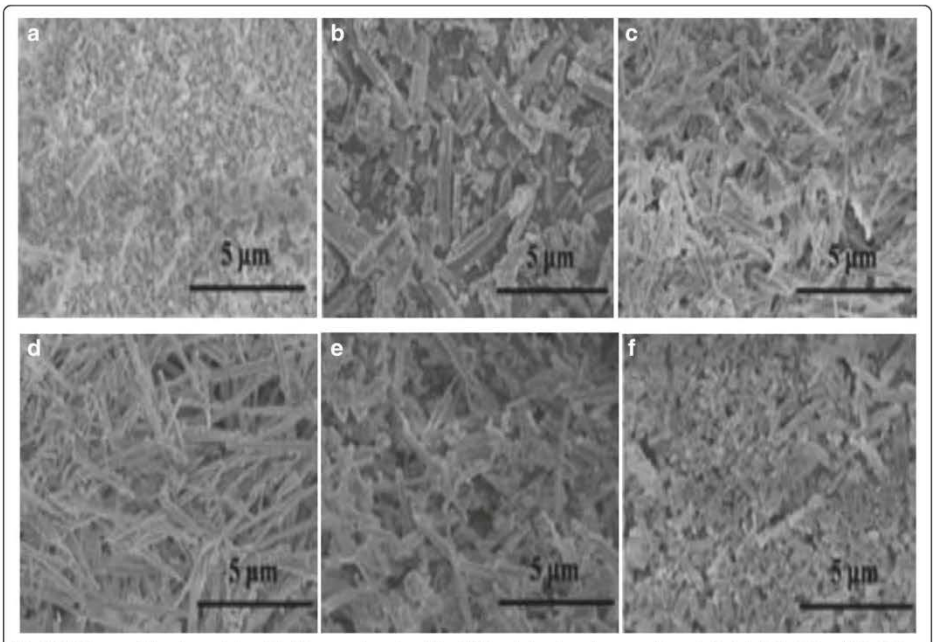

Fig. 7 SEM image of alumina particles with different molar ratio of [Bmin]PF_6 and aluminum isopropoxide. **a** Al_2O_3-0. **b** Al_2O_3-0.03. **c** Al_2O_3-0.12. **d** Al_2O_3-0.18. **e** Al_2O_3-0.24. **f** Al_2O_3-0.30

temperature of heat treatment affect the structure and morphology of the product. Especially, the temperature of heat treatment has a great impact on product. The excessively high temperature causes microscopic particles to gather together which in turn affects the order of the micromorphology and its structure [40].

Pang et al. [41] successfully prepared alumina bubble with tunable pore size using colloidal carbon spheres as template and aluminum nitrate as the aluminum source as shown in Fig. 8a. This study has shown that the concentration of aluminum nitrate has no significant effect on the morphology and pore size of alumina. Also, the adsorption time does not affect the morphology; however, the pore diameter increases gradually with increasing time. The adsorption temperature as well has an effect on the morphology. The surface of the particles becomes smooth, and the wall thickness increases with increasing temperature as shown in Fig. 8b, c.

Soft Template Method Soft template utilizes the intermolecular or intramolecular interaction forces, such as hydrogen bonds and bond and static electricity, to form aggregates with certain structural characteristics (liquid crystal, vesicles, micelle, microemulsion, self-assembled film, etc.) during the reaction. The reactants use these aggregates as template to generate a particle with certain morphology and structural features.

In the synthesis by soft template method, it is usually thought that the interaction between liquid crystalline phase and organic/inorganic interface plays a decisive role in the morphology of mesoporous materials [42, 43]. The liquid crystalline phase formed by the surfactant in solution has a rich structure such as lamellar phase, cubic phase and hexagonal phase and is easy to construct and adjust [44]. The interaction of the organic/inorganic interface is a weak hydrogen bond force in the strong acid environment while it is a strong electrostatic attraction force in the strong alkaline environment [45].

Gu et al. [46] successfully synthesized plate-like and rod-like mesoporous alumina, using F127 as soft template and aluminum isopropoxide as alumina source, and changing the mole ratio of aluminum isopropoxide and F127, as shown in Fig. 9. This study showed that the molar ratio of aluminum isopropoxide and F127 has an obvious effect on the morphology of the product. It is gradually transformed from square to plate and rod, and eventually, all become rod-like as the molar ratio increases. The result of crystalline phase analysis showed the diffraction peaks that are indexed at (311), (222), (400) and (440) associated with γ-alumina which become wider from curve a to f (Fig. 10). This XRD results suggest that the crystallite size can be smaller by increasing of F127 amount. Soft template F127 gives a good performance to weaken the crystallization process.

Groenewolt et al. [47] synthesized the ordered mesoporous γ-Al_2O_3 by using the soft template method. They have systematically studied the effects of various factors such as the type of aluminum source, the type of surfactant, the type of the acidity regulator and the reaction temperature on the structure and morphology of the products.

Precipitation Method Precipitation method produces the target products by adding the precipitant agent to the metal solution and heat treating the precipitate. The particles with different morphology can be obtained by adjusting the reaction temperature, the concentration of the reaction, pH, etc.

Zhou et al. [48] synthesized fibrillar nano-Al_2O_3, using $Al_2(SO_4)_3{\cdot}18H_2O$ and NaOH as raw materials with direct precipitation method. They discussed, respectively, the effect of reaction temperature and the concentration of $Al_2(SO_4)_3$ on the morphology (Fig. 11). The results showed that the fibrillar nano-Al_2O_3 with good dispersion was obtained at 65 °C.

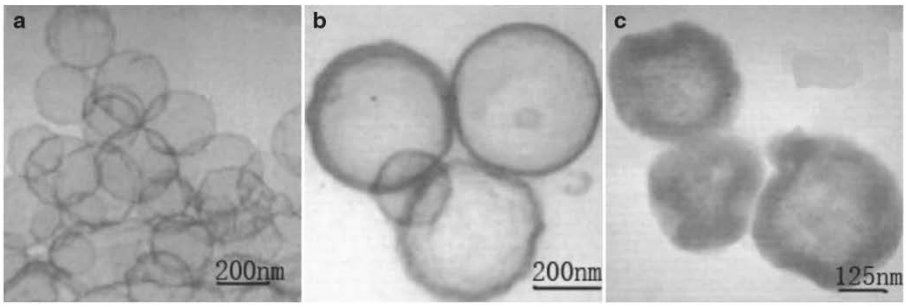

Fig. 8 TEM image of alumina bubble with different synthetic temperatures. **a** 25 °C **b** 45 °C and **c** 55 °C

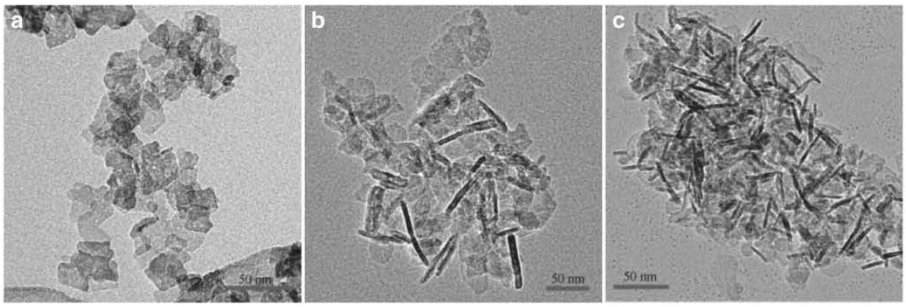

Fig. 9 TEM image of alumina with different morphology. **a** Al_2O_3-∞. **b** Al_2O_3-60. **c** Al_2O_3-30

The concentration of reactants is also one of the important factors which control the morphology and dispersion of the product. It has an effect on the formation and the growth rates of the crystal grain, and the effect on the formation rate of the grain is greater than that on the growth rate. As shown in Fig. 12, when the concentration of Al^{3+} is 1 mol L^{-1}, the granular product can be obtained. When the concentration of Al^{3+} is 0.8 mol L^{-1}, the fibrillar product of poor dispersion is formed. When the concentration of Al^{3+} is 0.3 and 0.5 mol L^{-1}, the reticular and fibrillar products of good dispersion are formed, respectively.

The Effect of Calcination System on the Morphology of Alumina

The alumina calcination system is very important for obtaining nanoparticle powder with monodispersity and uniform morphology. Nano-Al_2O_3 powder, which is composed of widely used α-Al_2O_3, γ-Al_2O_3 and amorphous Al_2O_3, is generally obtained by alumina precursor calcined at different temperatures. Therefore, the compaction among alumina particles of high activity is inevitable at high temperature, which results in severe particle agglomeration and resintering of individual particles with surrounding ones after melting with a formation of dendritic structure called "neckformation" of particle [49]. The result of the experiments showed that the calcination temperature, holding time and heating rate have a significant effect on the morphology of alumina. While the temperature is less than 800 °C, alumina particles can continue to maintain their original morphology. If the temperature becomes higher than 800 °C, the activity of alumina particles is enhanced, and agglomeration begins to occur [50]. Ceresa et al. [51] first presented the relationship between temperature and phase transformation of alumina during the calcination process.

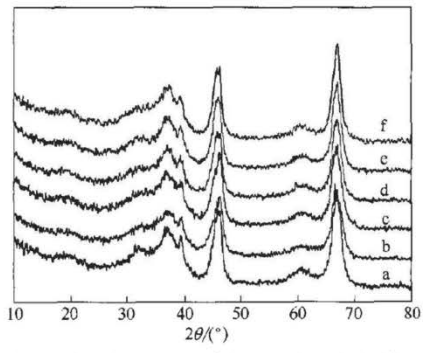

Fig. 10 Wide-angle XRD patterns of alumina synthesized with different F127 molar ratio. *a* Al_2O_3-∞, *b* Al_2O_3-1500, *c* Al_2O_3-1000, *d* Al_2O_3-500, *e* Al_2O_3-60, *f* Al_2O_3-30

It can be seen from Fig. 13 that the calcination temperature and time have a significant influence on the transformation of alumina (crystal type). When alumina particles calcined at the desired temperature in order to obtain certain crystal types, the calcination time depends on the size of the precursor. The smaller the particle size of precursor is, the shorter the time required for the calcination is, and the higher the temperature of the heat treatment is, the shorter the time required for the calcination is. The method of controlling the temperature and time during the calcination of Al_2O_3 is well-known. This method ensures that while the Al_2O_3 particles go through a complete phase change, their morphology remains unaffected and the dispersion of particles is reduced [52].

A significant amount of research is carried out in this area, and effective methods are proposed to control the morphology of alumina particles such as using DI water, alcohol and organic solvent mixtures to wash precursor before calcination in order to prevent agglomeration, enhance the dispersion, and increase the specific surface

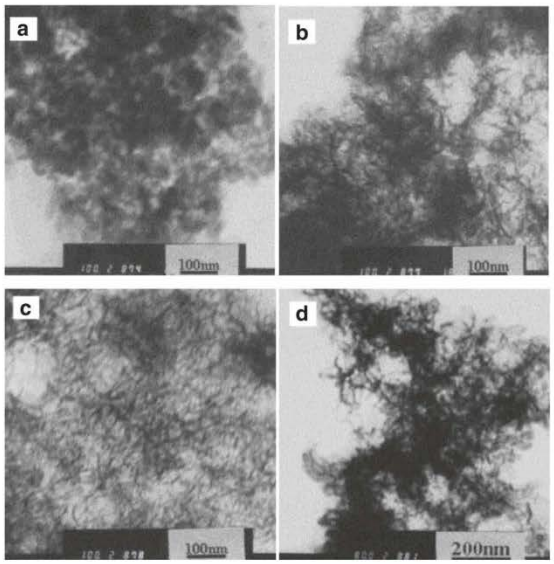

Fig. 11 TEM image of alumina with different synthetic temperatures. **a** 40 °C. **b** 55 °C. **c** 65 °C. **d** 80 °C

area of alumina [53]. In addition, the sintering properties of the powder can be improved with ultrasonic pretreatment, so that the neckformation created by agglomeration of the particles will not occur until 1400 °C [54]. The phase transformation temperature of γ-Al_2O_3 to α-Al_2O_3 can be decreased if sintering is carried out under the CO_2 or ethanol atmosphere; consequently, the well-crystalline spherical α-Al_2O_3 is eventually obtained [55].

Dispersants and surfactants also play an effective role in dispersion of particles and control of agglomeration. For example, using poly(methacrylic acid), organic acid, glucose, sucrose, inorganic salts, trimethylsilane and other additives [56], which results in a strong electrostatic repulsion among particles, eventually change the polarity of the particle surface from hydrophilic to hydrophobic (water-repellent). Polyacrylamide, silica gel and lignin and other polymer dispersants can form a protective layer with certain strength and thickness on the particle surface and prevents the agglomeration of the particles [57]. Surfactants can form a coating layer of several nanometers on the surface of the particles, which can reduce the surface energy and effectively hinder the interactions among the particles [58].

Besides, by adding 5 wt.% α-Al_2O_3 seed and 44 % NH_4NO_3 during the calcination process, the phase transition temperature can be decreased from 1200 to 900 °C [59]. Table 1 summarizes the effects of different calcination temperatures on the grain size of Al_2O_3 in the presence of various additives mentioned above.

As shown in Table 1, the amorphous Al_2O_3 particles obtained at 600 °C are light yellow while the additive is still present on the surface of the particles. This coating gradually disappears while 800 °C is reached. In addition, some additives can decrease the phase transition temperature of α-Al_2O_3 to 1000 °C. As the temperature increases, the grain size of Al_2O_3 will inevitably increase, meanwhile the agglomeration will start to occur. This is due to the fact that when Al_2O_3 completely transformed to α phase, the spatial arrangement of the O_2 in α-Al_2O_3 occurs, which is the reconstruction of phase transition from face-centered cubic to hexagonal close-packed lattice [60].

Conclusions

The morphology of Al_2O_3 can be influenced by various factors such as raw materials, concentrations, different synthesis methods, additives and heat treatment system. During the preparation of Al_2O_3, the morphology of the precursors and the protection of the particles during heat treatment play a decisive role in the final morphology of alumina. The morphology will not change

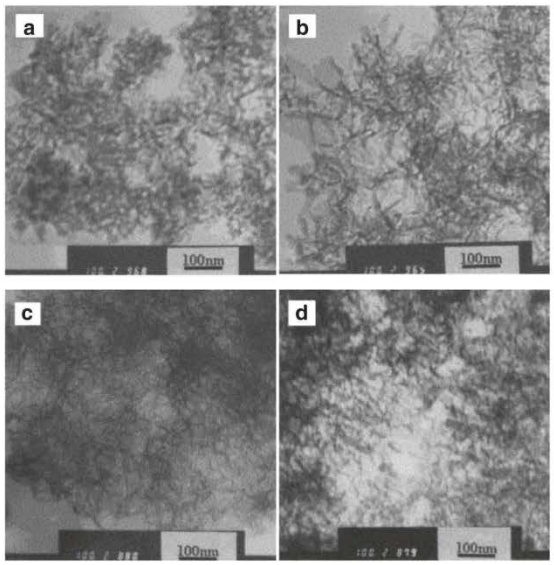

Fig. 12 TEM image of alumina of different concentration. **a** 1.0 mol L^{-1}. **b** 0.8 mol L^{-1}. **c** 0.5 mol L^{-1}. **d** 0.3 mol L^{-1}

during the low-temperature heat treatment. However, when high temperature is reached, the diffusion of the powder particles accelerates. Thus, the particles diffuse from the inside to the surface of the crystal lattice and spread to the surrounding resulting in the neckformation as well as the agglomeration of surrounded particles. Accordingly, the morphology of the particles changes. The use of various additives effectively reduces the calcination temperature; consequently, the problem of particle agglomeration can be solved. The

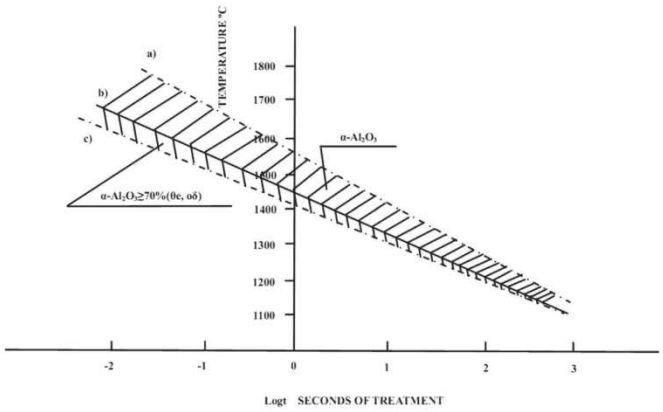

Fig. 13 The relationship between temperature and phase transformation of alumina

Table 1 Effect of calcination temperature on the size of alumina in the presence of additives

Calcination temperature (°C)	600	800	1050	1200
Al_2O_3 crystal type	Amorphous Al_2O_3	γ-Al_2O_3	α-Al_2O_3	α-Al_2O_3
Grain size (nm)	–	5~50	10~100	≥100
Color of Al_2O_3	Light yellow	White	White	White

utilization of template is a new research hotspot with the objective of improving the dispersibility of Al_2O_3 powder and controlling the shape of the sample particles.

Prospects

In the research field of the morphology of Al_2O_3 and its application performance, more work is needed to obtain nano-Al_2O_3 powder with different shapes, single morphology and good dispersion. There is also a need to expand the application range of this type of nano-Al_2O_3 powder and improve its application prospect in high tech and value-added product development fields.

Competing Interests

The authors declare that they have no competing interests.

Authors Contributions

YDX collected and reviewed the data and drafted the manuscript under the instruction of DK. DK and YK helped in modifying the draft. JC and WL suggested many helpful issues for improving the review paper. All authors read and approved the final manuscript.

Acknowledgements

This work was supported by the Natural Sciences and Engineering Research Council of Canada (NSERC). Technical support of the University Research Centre on Aluminum (CURAL) of the University of Quebec at Chicoutimi, Canada, and Civil, Architectural & Environmental Engineering (CAEE) of Drexel University, Philadelphia, PA, the United States of America.

Author details

[1]Department of Applied Science, University of Quebec at Chicoutimi (UQAC), Chicoutimi, Quebec G7H2B1, Canada. [2]Civil, Architectural & Environmental Engineering (CAEE), Drexel University, Philadelphia, PA 19104, USA. [3]School of Architectural & Material Engineering, Guizhou Normal University, Guiyang, Guizhou 550001, China.

Received: 3 February 2016 Accepted: 9 May 2016
Published online: 21 May 2016

References

1. Digne M, Sautet P, Raybaud P, Toulhoat H, Artacho E (2002) Structure and stability of aluminum hydroxides: a theoretical study. J Phys Chem B 106(20):5155–5162
2. Xu PK, Dong YB (1999) Corundum refractories. Metallurgical Industry Press, Beijing, pp 56–61
3. Wang LS (1994) Special ceramics. Central South University Press, Changsha, pp 133–138
4. Lu XJ, Cui XQ, Song MN (2003) Study on the alteration of chemical composition and structure parameters of modified montmorillonite. Miner Eng 16:1303–1306
5. Khatib K, Pons CH, Bottero JY, François M, Baudin I (1995) Study of the structure of dimet hyldioctadecylammonium-montmorillonite by small angle X-ray scattering. J Colloid Interface Sci 172(2):317–323
6. Zhang HY, Shan GB, Xing JM, Zhang HY (2007) Preparation of (Ni/W)-γ-$A1_2O_3$ microspheres and their application in adsorption desulfurization for model gasoline. Chem Eng Commun 194(7):938–945
7. Bartsch M, Saruhan B, Schmuecker M, Schneider H (2004) Novel low-temperature processing route of dense mullite ceramics by reaction sintering of amorphous SiO_2-coated γ-Al_2O_3 particle nanocomposites. J Am Ceram Soc 82(6):1388–1392
8. Lietti L, Forzatti P, Nova I, Tronconi E (2001) NO_x storage reduction over Pt-Ba/γ-Al_2O_3 catalyst. J Catal 204:175–191
9. Meijere AD, Meyer LU (2000) Shape control of CdSe nanocrystals. Nature 404(6773):59–61
10. Kolosnjaj J, Szwarc H, Moussa F (2007) Toxicity studies of fullerenes and derivatives. Bio-applications of nanoparticles. Springer, New York, pp 168–180
11. Ahmadi TS, Wang ZL, Green TC, Henglein A, El-Sayed MA (1996) Shape-controlled synthesis of colloidal platinum nanoparticles. Science 272(5270):1924–1925
12. Kim SM, Lee YJ, Bae JW, Potdar HS, Jun KW (2008) Synthesis and characterization of a highly active alumina catalyst for methanol dehydration to dimethyl ether. Appl Catal A Gen 348(1):113–120
13. Glemza R. High pore volume and pore diameter aluminum phosphate: US, US RE34911 E[P]. 1995.
14. Seri O, Kamazawa R (2012) Preparation of flake alumina by corrosion of aluminum in methanol. J Jpn Soc Matellurgy 59(6):307–310
15. Kim KT, Dao TD, Han MJ, Anjanapura RV, Aminabhavi TM (2015) Graphene coated with alumina and its utilization as a thermal conductivity enhancer for alumina sphere/thermoplastic polyurethane composite. Mater Chem Phys 153:291–300
16. Zhu HY, Riches JD, Barry JC (2002) γ-alumina nanofibers prepared from aluminum hydrate with poly(ethylene oxide) surfactant. Chem Mater 14(5): 2086–2093
17. Yu JW, Liao QL (2011) Effect of plate-like alumina seed on the fracture toughness of alumina ceramics. J Funct Mater 42(10):1833–1835
18. Kim P, Kim Y, Kim H, Song IK, Yi JH (2004) Synthesis and characterization of mesoporous alumina for use as a catalyst support in the hydrodechlorination of 1,2-dichloropropane: effect of preparation condition of mesoporous alumina. J Mol Catal A Chem 219(1):87–95
19. Thomas F, Schouller E, Bottero JY (1995) Adsorption of salicylate and polyacrylate on mesoporous aluminas. Colloids Surf A Physicochem Eng Asp 95(2):271–279
20. Tang GQ, Zhang CF, Sun CS, Yan B, Yang GX, Dai W et al (2011) Research progress of γ-Al_2O_3 support. Chem Ind Eng Prog 8:1756–1765
21. Li WJ, Shi EW, Yin ZW (1999) Growth habit of crystal and the shape of coordination polyhedron. J Synth Cryst 28(4):368–372
22. Zheng YQ, Shi EW, Li WJ, Wang BG, Hu XF (1998) Research and development of the theories of crystal growth. J Inorg Mater 14(3):321–332
23. Zhang Y, Wang YF, Yan YH (2002) Development and application of hydrothermal method in growing low-dimensional artificial crystal. Bull Chin Ceram Soc 21(3):22–26
24. Tian MY, Shi EW, Zhong WZ, Pang WQ, Guo JK (1998) Nano ceramics and nano ceramic powder. J Inorg Mater 2:129–137
25. Hu C C, Wu Y T, Chang K H. Low-Temperature Hydrothermal Synthesis of Mn_3O_4 and MnOOH Single Crystals: Determinant Influence of Oxidants[J]. Chemistry of Materials. 2008; 20(9):2890-894.
26. Li YH, Peng C, Zhao W, Bai MM, Rao PG (2014) Morphology evolution in hydrothermal synthesis of mesoporous alumina. J Inorg Mater 29(10):1115–1120
27. Ray JC, You KS, Ahn JW, Ahn WS (2007) Synthesis of mesoporous alumina using anionic, nonionic and cationic surfactants. Stud Surf Sci Catal 165(07):275–278
28. Zhang ZX, Shen ZQ, Ling FX, Xia CH (2013) Impacts of sodium nitrate additive on alumina morphology. Pet Process Petrochem 44(9):47–50
29. Pramod KS, Jilavi MH, Burgard D, Nass R (2005) Hydrothermal synthesis of nanosize alpha-al2o3 from seeded aluminum hydroxide. J Am Ceram Soc 81(10):2732–2734
30. Shi EW, Xia CT, Wang BG, Zhong WZ (1996) Application and development of hydrothermal method. J Inorg Mater 2:193–206
31. Mikhailov VI, Maslennikova TP, Krivoshapkin PV (2014) Materials based on aluminum and iron oxides obtained by the hydrothermal method. Glass Phys Chem 40(6):650–656
32. Hou HW, Xie Y, Yang Q, Guo QX, Tan CR (2005) Preparation and characterization of γ-AlOOH nanotubes and nanorods. Nanotechnology 16(6):741
33. Buining PA, Pathmamanoharan C, Jansen JBH, Lekkerkerker HNW (1991) Preparation of colloidal boehmite needles by hydrothermal treatment of aluminum alkoxide precursors. J Am Ceram Soc 74(6):1303–1307
34. Wang J, Zhang B, Xu XL (2007) Influence of hydrothermal temperature on structural and microstructural properties of boehmite. Nonferrous Metals Extractive Metallurgy 5:23–26

35. Varma HK, Mani TV, Damodaran AD, Warrier KGK, Balachandran U (1994) Sol–spray preparation, particulate characteristics, and sintering of alumina powders. Advanced materials l., pp 11–14
36. Li J, Pan YB, Xiang CS, Ge QM, Guo JK (2006) Low temperature synthesis of ultrafine α-Al_2O_3 powder by a simple aqueous sol–gel process. Ceram Int 32(5):587–591
37. Ning GL, Chang YF (2004) Shape-controlled synthesis of alumina nanoparticles by carboxy-containing organic molecules. Chem Res Chin Univ 23(3):345–348
38. Masouleh NSG, Taghizadeh M, Yaripour F (2014) Optimization of effective sol-gel parameters for the synthesis of mesoporous γ-Al_2O_3, using experimental design. Chem Eng Technol 37(9):1475–1482
39. Ji XW, Tang SK, Gu L, Liu TC, Zhang XW (2015) Synthesis of rod-like mesoporous γ-Al_2O_3 by an ionic liquid-assisted sol–gel method. Mater Lett 151:20–23
40. Roggenbuck J, Koch G, Tiemann M (2006) Synthesis of mesoporous magnesium oxide by CMK-3 carbon structure replication. Chem Mater 18(17):4151–4156
41. Pang LP, Zhao RH, Guo F, Chen JF, Cui WG (2008) Preparation and characterization of novel alumina hollow spheres. Acta Phys -Chim Sin 24(6):1115–1119
42. Zhao DY, Yang PD, Huo QS, Chmelka BF, Stucky GD (1998) Topological construction of mesoporous materials. Curr Opin Solid State Mater Sci 3(1):111–121
43. Brinker CJ, Dunphy DR (2006) Morphological control of surfactant-templated metal oxide films. Curr Opin Colloid Interface Sci 11(2–3):126–132
44. Anderson MT, Martin JE, Odinek JG, Newcomer PP (1998) Surfactant-templated silica mesophases formed in water: cosolvent mixtures. Chem Mater 10(1):311–321
45. Materna KL, Grant SM, Jaroniec M (2012) Poly(ethylene oxide)-poly(butylene oxide)-poly(ethylene oxide)-templated synthesis of mesoporous alumina: effect of triblock copolymer and acid concentration. ACS Appl Mater Interfaces 4(7):3738–3744
46. Gu L, Cui XL, Tang SK, Zhang XW (2015) Morphology-controlled synthesis of mesoporous alumina dependent on triblock copolymer. J Chem Ind Eng 66(9):3782–3787
47. Groenewolt M, Brezesinski T, Schlaad H, Antonietti M, Groh P, Iván B (2005) Polyisobutylene-block-poly(ethylene oxide) for robust templating of highly ordered mesoporous materials. Adv Mater 17(17):1158–1162
48. Zhou KG, Li YP, Li JC, He WW, Yang XJ (2009) Preparation of fibrous nano-alumina by direct precipitation. J Hunan Univ 36(8):59–63
49. Kao HC, Wei WC (2000) Kinetics and microstructural evolution of heterogeneous transformation of θ-alumina to α-alumina. J Am Ceram Soc 83(2):362–368
50. Sarikaya Y, Sevinç İ, Akinç M (2001) The effect of calcinations temperature on some of the adsorptive properties of fine alumina powders obtained by emulsion evaporation technique. Powder Technol 116(1):109–114
51. Ceresa EM, Gennaro A, Cortesi P (1987) α-alumina in the form of spherical non-aggregation particles having a narrow size distribution and size below 2 μm and process for preparing same. US Pat: 4818515
52. Kass MD, Cecala DM (1997) Enhanced sinter ability of alumina particles by pretreating in liquid ammonia. Mater Lett 32(s2-3):55–58
53. Bousquet C, Elissalde C, Aymonier C, Maglione M, Cansell F, Heintz JM (2008) Tuning Al_2O_3 crystallinity under supercritical fluid conditions: effect on sintering. J Eur Ceram Soc 28(1):223–228
54. Shek CH, Lai JKL, Gu TS, Lin GM (1997) Transformation evolution and infrared absorption spectra of amorphous and crystalline nano-Al_2O_3 powders. Nanostruct Mater 8(5):605–610
55. Xie ZP, Lu JW, Gao LC, Li WC, Xu LH, Wang XD (2003) Influence of different seeds on transformation of aluminum hydroxides and morphology of alumina grains by hot pressing. Mater Des 24(3):209–214
56. Li JG, Sun X (2000) Synthesis and sintering behavior of a nanocrystalline α-Al_2O_3 powder. Acta Mater 48:3103–3112
57. Karagedov GR, Lyakhov NZ (1999) Preparation and sintering of nano-sized α-Al_2O_3 powder. Nanostruct Mater 11(99):559–572
58. Strekopytov S, Exley C (2006) Thermal analyses of aluminum hydroxide and hydroxyaluminosilieates. Polyhedron 25(8):1707–1713
59. Liu HY, Ning GL, Gan ZH, Lin Y (2008) Emulsion-based synthesis of unaggregated, spherical α-alumina. Mater Lett 62(10):1685–1688
60. Bagwell RB, Messing GL, Howell PR (2001) The formation of α-Al_2O_3 from θ-Al_2O_3: the relevance of a "critical size" and: diffusional nucleation of "synchro-shear". J Mater Sci 36(7):1833–1841

APPENDIX II

RSC Advances

PAPER

View Article Online
View Journal | View Issue

Cite this: *RSC Adv.*, 2015, **5**, 7529

In vivo pharmacokinetic features and biodistribution of star and rod shaped gold nanoparticles by multispectral optoacoustic tomography

Jing Wang,†[a] Yadian Xie,†[ab] Liming Wang,[a] Jinglong Tang,[a] Jiayang Li,*[a] Duygu Kocaefe,[b] Yasar Kocaefe,[b] Zhiwen Zhang,[c] Yaping Li[c] and Chunying Chen*[a]

Received 27th October 2014
Accepted 22nd December 2014

DOI: 10.1039/c4ra13228a

www.rsc.org/advances

Metallic nanomaterials, especially gold nanoparticles, which have low toxicity and high photothermal conversion efficiency, exhibit promising theranostic applications in biomedical fields. However, detailed preclinical studies of these nanomaterials, such as pharmacokinetics, metabolism, long-term stability and toxicity potential should still be performed. Photoacoustic imaging as a novel non-invasive imaging technique provides convenience for studying real-time semiquantitative pharmacokinetic and biodistribution profiles of drugs or probes to determine whether they can reach the target areas and their metabolic pathways. In this article, we prepared chitosan-capped star shaped gold nanoparticles (AuNSs) and used multispectral optoacoustic tomography (MSOT) to visualize AuNSs in the blood vessels, liver, spleen and kidneys in real time. We also compared these results with chitosan-capped rod shaped gold nanoparticles (AuNRs). The results show that both AuNSs and AuNRs experience rapid blood clearance and have fast and long-term accumulation in the liver and spleen (reaching the peak value within 10 min). The pharmacokinetic data of the two gold nanoparticles fitted to the two-compartment model. The important pharmacokinetic parameters were calculated. The results from MSOT were qualitatively validated by inductively coupled plasma mass spectrometery (ICP-MS). Our results demonstrate that MSOT can serve as an effective tool to monitor gold nanoparticles' pharmacokinetics and biodistribution in specific organs.

Introduction

With the rapid development of nanotechnology, the application of nanomaterials in medicine shows potent improvements in early diagnosis and therapies of many diseases of global concern, such as cardiovascular disease, Alzheimer disease, and cancer.[1–4] Due to their unique physicochemical properties, metallic nanomaterials responsive to near-infrared (NIR, 650–900 nm) light have generated significant interests for biomedical applications in recent years.[5,6] Since NIR light is minimally absorbed by skin and tissue, it has deeper tissue penetration and less tissue invasion.[7] Thus these metallic nanomaterials, especially gold nanoparticles, which have high-absorption cross section for conversion of NIR light to heat, exhibit diverse and promising theranostic applications in multimodal imaging, local hyperthermia, and drug delivery.[8–12] Our recent studies exhibit an innovative and effective strategy for targeted cancer therapy in nanomedicine by developing a NIR light-triggered nanoplatform of thermoresponsive polymer encapsulated mesoporous silica coated-gold nanorod for site-specific hyperthermia and light-controllable drug delivery.[13] In spite of having a vast application prospect, reports on clinical applications of these metallic nanoparticles are still far from satisfactory. Widely as gold nanoparticles have been recognized for their low toxicity, good biocompatibility and chemical inertness,[14] detailed preclinical studies, such as pharmacodynamics, pharmacokinetics (absorption, distribution, metabolism and excretion), long-term stability, and toxicity evaluation, should be performed which are important and essential for these new potential nanomedicine candidates before their clinical trials.[15]

The traditional methods of studying *in vivo* pharmacokinetic and biodistribution need to collect the blood at different time points or to remove some part of the viscera for *in vitro* physicochemical analysis, which are time-consuming and high-cost. Multiple imaging techniques, such as optical imaging, positron

[a]*CAS Key Laboratory for Biomedical Effects of Nanomaterials and Nanosafety, National Center for Nanoscience and Technology, Beijing 100190, China. E-mail: chenchy@nanoctr.cn; lijiayang@nanoctr.cn; Fax: +86-10-6265-6765; Tel: +86-10-8254-5560*

[b]*Department of Applied Sciences, University of Quebec at Chicoutimi (UQAC), Canada*

[c]*Shanghai Institute of Materia Medica, Chinese Academy of Sciences, Shanghai, 201203, China*

† These authors contributed equally.

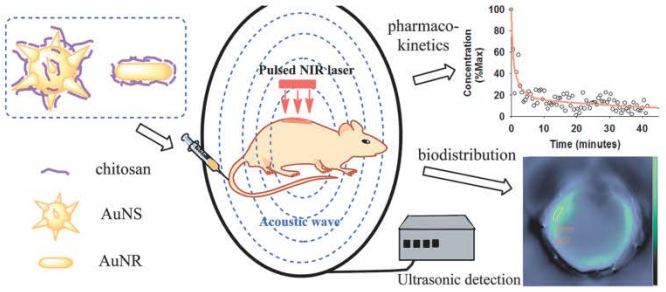

Scheme 1 Schematic illustration of pharmacokinetic and biodistribution analysis of chitosan-capped star or rod shaped gold nanoparticles by multispectral optoacoustic tomography.

emission tomography (PET), X-ray computed tomography (CT), magnetic resonance imaging (MRI) and photoacoustic imaging, have provided non-invasive pharmacokinetic and biodistribution analysis of drugs or probes.[16] Conventional optical imaging suffers from low spatial resolution and shallow penetration depth (~1 mm) which limits its application.[17,18] PET requires radioactive-labeling materials that may have potential hazards to patients.[19] CT and MRI have higher spatial resolution (CT: ~10–50 μm; MRI: 100 μm) than optical imaging and PET (~1 mm), but it cannot achieve dynamic pharmacokinetic and biodistribution analysis in real time.[20,21] Furthermore, the cost of MRI is very expensive. Photoacoustic imaging as a novel biomedical imaging technique has recently attracted significant attention and research interests.[22–25] It takes advantage of both optical and acoustic imaging with deeper tissue penetration (up to 40 mm), higher spatial resolution (150 μm for whole body; 20–50 μm for local imaging), and higher contrast. In photoacoustic imaging technology, multispectral optoacoustic tomography (MSOT) is a convenient and efficient tool. By using multiple excitation wavelengths and multispectral unmixing, images of both tissue-intrinsic (*e.g.* hemoglobin, melanin) and extrinsic (*e.g.* fluorescent dyes, probes and gold nanoparticles) absorbers can be acquired at the same time, supplying rich information for disease diagnosis and analysis. Moreover, as a complementary tool with other imaging techniques, MSOT provides a real-time monitoring method to evaluate photothermal-responsive gold nanomaterials' pharmacokinetics and biodistribution. Especially for those gold nanoparticles with short blood circulation time and fast distribution *in vivo*, MSOT will present more detailed information for their early changes of pharmacokinetic features and biodistribution, which helps guide their clinical applications.

The biological effects of gold nanoparticles with various surface modifications, sizes and shapes have drawn an increased interest both *in vitro* and *in vivo*.[26–33] For example, our group found that poly(diallyldimethylammonium chloride) (PDDAC) coated gold nanoparticles have exhibited more than 10 folds cellular uptake than cetyltrimethylammonium bromide (CTAB) coated gold nanoparticles with almost no cytotoxicity.[26] Jong *et al.* indicated that 10 nm gold nanoparticles showing the most widespread organ distribution than other larger particles which are only detected in the blood, liver and spleen.[30] Arnida *et al.* reported that poly(ethylene glycol) (PEG) functionalized gold nanorods are taken up to a lesser extent by the liver and had longer circulation time in the blood compared with their spherical counterparts.[32] Huang *et al.* found that short-rod mesoporous silica nanoparticles (short-rod MSNs, aspect ratios: 1.5) are easily trapped in the liver while long-rod mesoporous silica nanoparticles (long-rod MSNs, aspect ratios: 5) are more distributed in the spleen at 2 h post injection, and short-rod MSNs have a more rapid clearance rate than long-rod MSNs by urine and feces.[33] Recently, star shaped gold nanoparticles (AuNSs) have been rapidly developed for biomedical applications as a novel photothermal platform due to the fact that elongated or sharp nanoparticles appear to be more efficient heaters than other nanostructures.[34,35] AuNSs can also be used as carriers for drugs or photosensitizers with high loading efficiency by taking advantage of their high surface-to-volume ratio.[36,37] However, data on pharmacodynamics and pharmacokinetics studies of AuNSs are limited in the literature. This study aims to evaluate the pharmacokinetic and biodistribution of AuNSs as new MSOT contrast agents, and to compare their results with rod shaped gold nanoparticles (AuNRs), which has been widely used in biomedical applications. Chitosan was chosen as the surface stabilizer of AuNSs and AuNRs which has favourable properties such as biocompatibility, non-toxicity and biodegradability and has been widely applied in drug delivery.[38,39] In this article, we present a MSOT method for real-time visualization of chitosan-capped AuNSs in blood vessels, liver, spleen and kidney, respectively, compared to AuNRs with the same surface coating (Scheme 1).

Materials and methods

Chemicals and materials

Hydrogen tetrachloroaurate(III) trihydrate ($HAuCl_4 \cdot 3H_2O$, 99.9%), silver nitrate ($AgNO_3$, 99%), ascorbic acid (AA, 99%), glucose (99%), sodium borohydride ($NaBH_4$), cetyltrimethylammonium bromide (CTAB) were purchased from Alfa Aesar, United States. Chitosan (low molecular weight, 99%)

was purchased from Aldrich Chemical, United States. HNO_3 (MOS), H_2O_2 (MOS), ethylic acid, hydrochloric acid (HCl, GR 36.0–38.0%) were purchased from Beijing Chemical Reagent Institute, China. Isoflurane was purchased from Hebei Jiuzhi Pharmaceutical Limited Company, China. All the chemicals and materials used were of analytical grade unless otherwise stated. Stock standard solutions for gold and bismuth were obtained as 1000 mg L^{-1} from the National Research Centre for CRMs, China. Ultrapure Milli-Q water with resistivity of 18.2 MΩ was used for all solution preparations.

Apparatus

Transmission electron microscope (TEM) images were acquired on a FEI Tecnai G2 F20 U-TWIN transmission electron microscope (FEI Company, USA). Scanning electron microscope (SEM) measurements were performed on a Hitachi S-4800 field emission scanning electron microscope (Hitachi Ltd., Japan). Hydrodynamic diameter and zeta-potential measurements were taken using a Malvern zeta sizer Nano ZS instrument (Malvern Instruments, United Kingdom). Extinction spectrum was obtained using a UV-3600 spectrophotometer (Shimadzu Corporation, Japan). Photoacoustic imaging was performed on MSOT inVision 128 (iThera Medical, Germany). The amount of Au was accurately measured by an Elan DRC II inductively coupled plasma mass spectrometer (ICP-MS, Perkin-Elmer, USA).

Synthesis of AuNSs and AuNRs

AuNSs were synthesized as described in the literature.[40] Briefly, AuNSs were obtained by mixing 2 mL 10 mM $HAuCl_4$ aqueous solution with 100 mL H_2O and 0.2 mL 10 mM $AgNO_3$ aqueous solution. Then 0.4 mL 100 mM AA aqueous solution was rapidly added to the mixed solution with stirring at 400 rpm for 10 s. After one minute at rest, 100 mL 1 wt% chitosan and 1 wt% ethylic acid aqueous solution was added to the above solution to stabilize AuNSs. The color of the solution change from yellow to colorless after the reducing agent was added, and finally became light blue.

CTAB-capped AuNRs were synthesized by the seed-mediated growth method in our previous work.[12] Chitosan-coated AuNRs were prepared by using 1 wt% chitosan and 1 wt% ethylic acid aqueous solution to resuspend CTAB-capped AuNRs' precipitation after centrifugation. Then the solution was stirred overnight.

Characterizations

The size and morphology of gold nanoparticles were observed by TEM and SEM. Hydrodynamic diameter and zeta-potential were measured in water solution at 25 °C. The NIR extinction spectra were obtained with a 1 cm wide quartz cell at 25 °C by UV spectrometer. The MSOT-derived spectra were measured by agar phantom (1.2 wt% agar concentration in aqueous solution) as a container and acquired by PCA/ICA method of multispectral unmixing.

Sensitivity study

The linearity of photoacoustic signal across concentration of AuNSs and AuNRs were tested by MSOT with agar phantom. Six gold nanoparticles' aqueous solutions with different concentrations were prepared. The concentrations of the solutions were 1.56, 3.13, 6.25, 12.5, 25 and 50 μg mL^{-1}, which the corresponding value of maximum optical density (OD_{max}) was 0.025, 0.05, 0.1, 0.2, 0.4 and 0.7, respectively, according to the NIR extinction spectra results. The photoacoustic signals of the corresponding solutions were measured by MSOT with excitation wavelengths from 680 nm to 900 nm in 10 nm steps. The quantitative analysis of the spectra was unmixed by linear regression.

Real-time MSOT imaging for *in vivo* pharmacokinetic and biodistribution study

Procedures involving animals were approved by the Institutional Animal Care and Use Committee (IACUC). The male Balb/c nude mouse (6–8 weeks, 20 g body weight) was narcotized by isoflurane and placed on a holder with thin polyethylene membrane and ultrasonic coupling agent. Then its tail vein was connected to a syringe through syringe needle (30 G syringes) and a long polythene tubing (internal diameter: 0.28 mm, external diameter: 0.61 mm). After the mouse was put into the chamber of MSOT, the scan section was chosen according to the specific position of the organ or tissue and experimental parameters were set up. Then 2 mg kg^{-1} AuNS–chitosan or AuNR–chitosan glucose solution (10 g glucose in 20 mL water) was injected into the mouse through tail vein and then photoacoustic signal was collected immediately. Jugular vein, liver, spleen and kidneys were monitored by four mice respectively for *in vivo* pharmacokinetic study. The cumulative time of each *in vivo* study was around 45 min. The main experimental parameters were 10 excitation wavelength steps for each slice from 680 nm to 930 nm, and 25 frames per wavelength. The MSOT signals were collected by one per 30 s without delay.

Image reconstruction and multispectral processing

The tomographic images from MSOT were reconstructed using a linear model-based inversion. Size and resolution presets were 25 mm ROI (region of interest) with 100μ resolution. The low and high filter cut-off frequencies were 50 kHz and 7 MHz, respectively. The injected gold nanoparticles were resolved within tissues or organs by using multispectral unmixing of linear regression. The data of pharmacokinetic and biodistribution were treated by Winnonlin 5.2 software. The temporal evolution of the signal in individual pixels fitted into classical two-compartment pharmacokinetic model, allowing the analysis of important kinetic parameters, such as absorption half-life ($t_{1/2\alpha}$), elimination half-life ($t_{1/2\beta}$), areas under the curve (AUC), plasma clearance (Cl) and apparent volume of distribution (V_d).

Blood circulation time and biodistribution study by ICP-MS

To further validate the quantitative accuracy of MSOT, 200 μL suspensions with Au content of 0.1 mg mL^{-1} was intravenously

injected in male Balb/c mice (6–8 weeks, ~20 g body weight). Blood samples were collected at 3 min, 10 min, 30 min, 2 h, 5 h and 24 h post administration. The mice at 3 min, 10 min, 30 min and 24 h were sacrificed and organs including heart, liver, spleen, lung and kidneys were dissected and weighted. Each group has three mice as replicates. All the samples were stored at −80 °C before ICP-MS analysis. For ICP-MS measurement, the above samples were pre-digested overnight with 5.0 mL concentrated HNO_3. Then they were mixed with 3.0 mL 30% H_2O_2 and digested for 2 h in open vessels on a hot plate at 50–150 °C by gradually warming. When the residual volume decreased to about 1 mL, 2–3 mL aqua regia (HNO_3–HCl = 1 : 3) was added to continue the digestion till the solution volume decreased to about 0.5 mL. Finally, the remaining solution was cooled and diluted to 3.0 g on the balance with a mixed acid solution containing 2% HNO_3 and 1% HCl. For quantitative analysis, a series of Au standard solutions (0.5, 1, 5, 10, 50 ppb) were prepared with the mixed acid solution to obtain the standard curve. Bismuth (20 ppb) in the mixed acid solution was used as an internal standard. Quantification was carried out by external five-point calibration with internal standard correction. Both the standard solutions and the samples were measured three times by ICP-MS. The amount of Au element was expressed as percentage of the injected dose (% ID).

Results and discussion

Characterizations

Fig. 1 shows TEM and SEM images of chitosan-capped AuNSs and AuNRs, respectively. TEM image of AuNSs show that their outer diameter was around 90 nm with 50 nm core and 20 nm tips (Fig. 1a). TEM image of AuNRs show that they had an aspect ratio of 3.2 with 18 nm width and 58 nm length (Fig. 1b). The shape of AuNSs was further confirmed by SEM image (Fig. 1c) with protruding tips on the surface of AuNSs. SEM image of AuNRs (Fig. 1d) was consistent with TEM result (Fig. 1b). Both AuNSs and AuNRs had uniform size and morphology from electron microscope results. As shown in Fig. 2a, chitosan-capped AuNSs showed an average hydrodynamic diameter of 112.5 nm with a good polydispersity index of 0.211. The size of AuNSs measured by the dynamic light scattering method was larger than that observed by TEM, because of the existence of hydration layer. Due to the rod-shaped structure, chitosan-capped AuNRs have two diffusion modes in aqueous solution, thus showed two peaks of size distribution (Fig. 2b). Zeta-potentials of AuNSs and AuNRs were measured to be +36.6 mV and +32.3 mV, respectively, due to the protonated chitosan layers (Fig. 2c and d). The surface plasmon resonance (SPR) absorbance peak of AuNSs was at ~800 nm with a broader absorption band than AuNRs in the NIR region (Fig. 3a). AuNRs had a narrower absorption peak at 720 nm (Fig. 3a). Both absorbance curves (AuNSs and AuNRs) derived from MSOT by PCA/ICA method of multispectral unmixing were in good agreement with the UV-visible spectrometer results (Fig. 3b). The obvious NIR absorption made both AuNSs and AuNRs as a sort of very suitable NIR probes for testing by MOST.

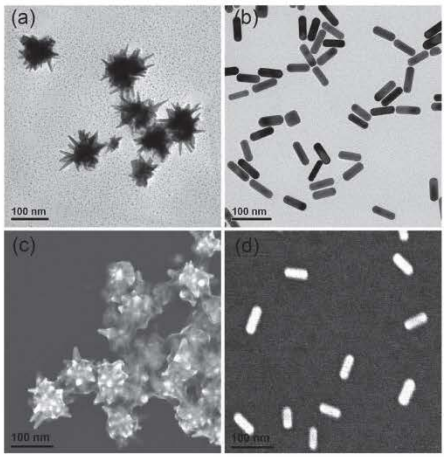

Fig. 1 TEM images of chitosan-capped AuNSs (a) and AuNRs (b) and SEM images of chitosan-capped AuNSs (c) and AuNRs (d).

Sensitivity study

Phantom measurement results showed excellent linearity (AuNSs: $R^2 = 0.9982$; AuNRs: $R^2 = 0.9822$) and high sensitivity (lowest limit concentration: ~3.1 μg mL^{-1} Au) for both AuNSs and AuNRs probes. Six solutions of different concentrations were prepared and filled in the left hole of the phantom, while the glucose solution was as a control in the right hole (Fig. 3c and d). When the OD_{max} was reduced from 0.7 to 0.025, the intensity of the photoacoustic signals were decreased gradually for both AuNSs and AuNRs, showing excellent linearity of photoacoustic signal across concentration (Fig. 3e and f). Since there was no signal appearance at $OD_{max} = 0.025$ (Fig. 3c and d), the lowest detection limits for both gold nanoparticles were ~3.1 μg mL^{-1} of Au (OD_{max} at 0.05). Besides, the intensity of photoacoustic signals at each OD_{max} of AuNSs was higher than that of AuNRs (Fig. 3c and d). By comparing the slope of the equation of the line, the signal intensity under the same concentration of AuNSs (equation: $y = 3.63x + 0.78$) was higher than AuNRs (equation: $y = 3.34x + 0.67$) as well (Fig. 3e and f). According to the lowest detection limit, mice were injected with 1 mg kg^{-1} (30 times multiplied by concentration at $OD_{max} = 0.05$) of gold nanoparticles' solution and it was found that the *in vivo* photoacoustic signal was very weak and unstable (data are not shown). Then dosage of 2 mg kg^{-1} (60 times multiplied by concentration at $OD_{max} = 0.05$) was chosen for *in vivo* pharmacokinetic and biodistribution study, because there was strong and stable photoacoustic signal *in vivo* when the mice were injected 2 mg kg^{-1} gold nanoparticles' solution.

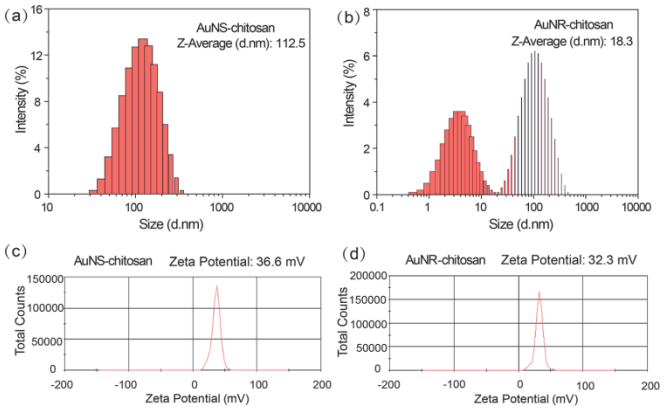

Fig. 2 Hydrodynamic diameters and zeta-potentials of chitosan-capped AuNSs and AuNRs by a Malvern particle analyzer. Hydrodynamic diameters of chitosan-capped AuNSs (a) and AuNRs (b). Zeta-potentials of chitosan-capped AuNSs (c) and AuNRs (d).

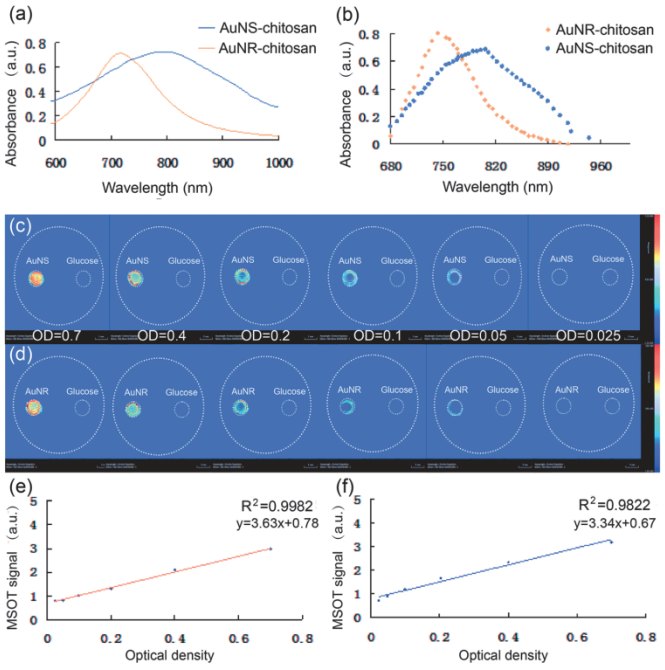

Fig. 3 Absorption spectra, sensitivity and linearity measurements of chitosan-capped AuNSs and AuNRs. NIR absorption spectra of AuNSs and AuNRs by UV-visible spectrometer (a) and MSOT (b). Sensitivity measurements of AuNSs (c) and AuNRs (d) solutions with different OD_{max} by phantom. Linearity relationships of optoacoustic signals of AuNSs (e) and AuNRs (f) across concentrations.

Real-time MSOT imaging for *in vivo* pharmacokinetic and biodistribution study

It is vital to understand the pharmacokinetics, drug distribution *in vivo* and drug accumulation and metabolism in specific organs in the new drug development process. MSOT as a non-invasive imaging technology can acquire quantitative information with real-time and dynamic imaging of drug distribution in mice with high temporal and spatial resolution. Of note, MSOT has a prominent advantage to monitor short-time and real-time accumulation and metabolism in specific organs than any other *in vivo* imaging technique.

The pharmacokinetic analysis of gold nanoparticles was carried out by monitoring of jugular vein in the bloodstream after intravenous injection (Fig. 4). The plasma drug concentration *versus* time profiles of chitosan-capped AuNSs and AuNRs revealed a rapid initial concentration drop followed by more gradual decline (Fig. 4a and b). At 3 min, the percentage concentration of AuNSs remained in blood was 28% and then dropped to 8% after 40 min post administration, while the percentage concentration of AuNRs at 3 min was 20% and dropped to 3% after 40 min post administration. These pharmacokinetic characteristics are in agreement with previous reports indicating that positively charged nanoparticles possessed relatively short half-lives than neutral and zwitterionic nanoparticles.[41] The pharmacokinetic data of the two gold nanoparticles fit to classical two-compartment model. The pharmacokinetic equations are $C(t) = 20.11e^{-0.577t} + 5.94e^{-0.018t}$ for AuNSs and $C(t) = 24.69e^{-0.871t} + 4.12e^{-0.020t}$ for AuNRs, respectively. The main pharmacokinetic parameters were listed in Table 1. It can be clearly seen that AuNSs has a longer circulation time ($t_{1/2\alpha} \sim 1.2$ min) than AuNRs ($t_{1/2\alpha} \sim 48$ s) in the bloodstream. Besides, AuNSs ($t_{1/2\beta} \sim 38.5$ min, Cl = 0.11 mL min^{-1}) also eliminated more slowly from blood than AuNRs ($t_{1/2\beta} \sim 34.7$ min, Cl = 0.17 mL min^{-1}) due to the longer elimination half-life and slower plasma clearance. Meanwhile, the value of AUC of AuNSs (AUC: 365 μg min mL^{-1}) markedly increased by about 1.6-fold in comparison to that of AuNRs (AUC: 234 μg min mL^{-1}). This also illustrates that the blood circulation time of AuNSs is obviously longer than AuNRs. The large values of V_d were far beyond the volume of the mouse's body fluid, which implies that the two gold nanoparticles may have a wide distribution or accumulation in the body. The smaller V_d value of AuNSs (V_d: 6.16 mL) means that more AuNSs were in the blood than AuNRs (V_d: 8.55 mL) in accord with their longer plasma half-life.

Table 1 Pharmacokinetic parameters of AuNSs and AuNRs in mice following intravenous administration

	Chitosan-capped AuNSs	Chitosan-capped AuNRs
$t_{1/2\alpha}$	1.2 min	48 s
$t_{1/2\beta}$	38.5 min	34.7 min
AUC	365 μg mL^{-1} min^{-1}	234 μg mL^{-1} min^{-1}
Cl	0.11 mL min^{-1}	0.17 mL min^{-1}
V_d	6.16 mL	8.55 mL

Then we used MSOT to monitor the accumulation and metabolism of gold nanoparticles in the liver, spleen and kidney in real time. The region of interest (ROI) was chosen at the position of the liver or spleen and highlighted in yellow color circle (Fig. 5f and g). By monitoring the signal strength of ROI, the concentration–time curve of the liver after the injection of AuNSs was obtained (Fig. 5a). Both AuNSs and AuNRs have similar accumulation results in the liver. The MSOT signals showed increased accumulation in the liver as time elapsed and the concentration in the liver went up to 80% in just 5 min (Fig. 5a and b). Then the percentage concentrations of AuNSs and

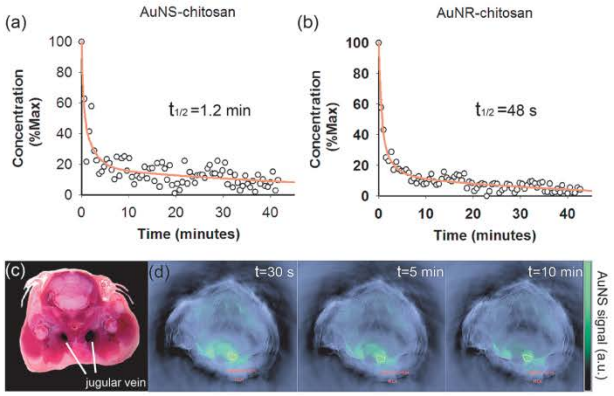

Fig. 4 *In vivo* real-time pharmacokinetic study by MSOT. Monitoring of jugular vein after chitosan-capped AuNSs (a) and AuNRs (b) injection. Image of a frozen section of mice (c). Optoacoustic images after AuNSs injection with the region of interest (ROI, highlighted in yellow circle) of jugular vein (d).

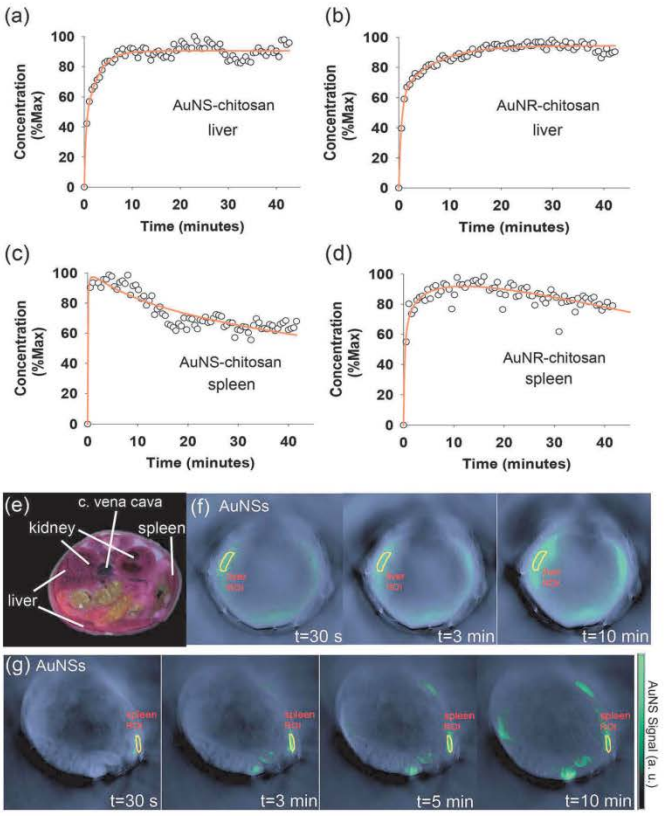

Fig. 5 *In vivo* biodistribution study by MSOT. Monitoring of photoacoustic signal in the liver after intravenous injection of chitosan-capped AuNSs (a) and AuNRs (b). Monitoring of photoacoustic signal in the spleen after intravenous injection of AuNSs (c) and AuNRs (d). Image of a frozen section of mice (e). Photoacoustic images with region of interest (ROI, highlighted in yellow circle) in the liver (f) and spleen (g) after AuNSs injection.

AuNRs reached a plateau at about 20 min and became stable in the rest of time (Fig. 5a and b). There was certain difference of accumulation between AuNSs and AuNRs in the spleen (Fig. 5c and d). The concentration of AuNSs accumulated in the spleen rapidly reached 90% within 2 min, and began to decline to about 70% in the next 15 minutes and then became stable. Meanwhile, the concentration of AuNRs in spleen rose up to 90% after 10 minutes and had a slight decline in the next 30 min. It may be attributed to the differences of shape and size or more AuNSs in the bloodstream which caused the concentration change in the spleen in the first few minutes, due to the fact that AuNSs had longer blood circulation time than AuNRs. There were no clear optoacoustic signals observed in kidneys for both AuNSs and AuNRs due to their lower concentrations (<3% of % ID, Fig. 6d) compared to liver (~60% of % ID, Fig. 6b) and spleen (~6% of % ID, Fig. 6c).

Validating blood circulation time and biodistribution data from MSOT by ICP-MS

To validate the quantitative accuracy of MSOT, we employed ICP-MS to measure Au element contents in the blood and organs. The results of ICP-MS were in accord with MSOT's data. Both AuNSs and AuNRs had fast clearance in the bloodstream (half-life less than 3 min). From 3 min to 10 min, the content of AuNSs in the bloodstream dropped from 20.9% ± 1.0% to 15.2% ± 1.3%, while the content of AuNRs dropped from 15.2% ± 0.7% to 7.0% ± 0.9%, which means the blood circulation time of AuNSs was longer than AuNRs with significant difference ($P < 0.01$) at the first 3 min and 10 min (Fig. 6a). The

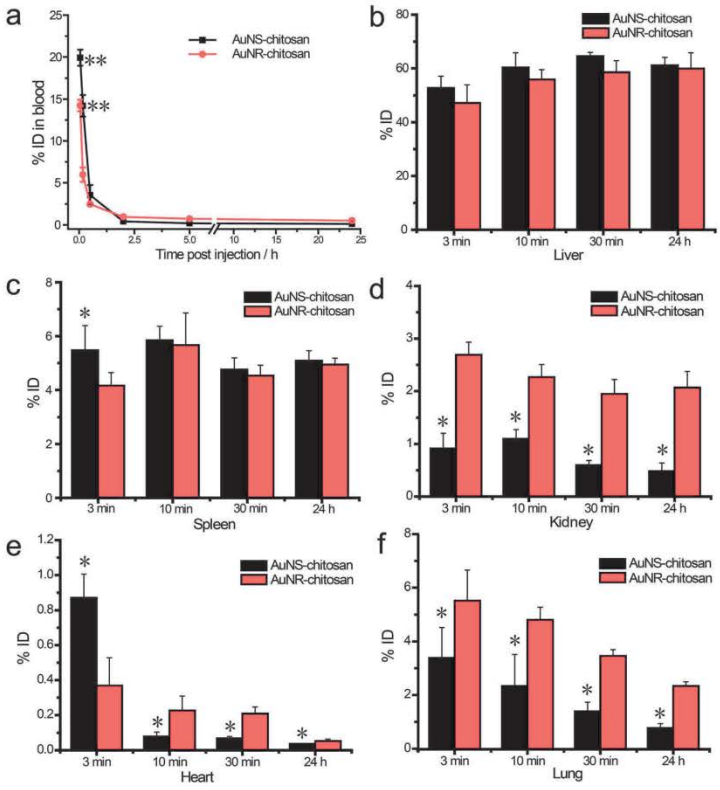

Fig. 6 Blood circulation time and biodistribution study by ICP-MS. (a) Blood circulation time measurement of AuNSs and AuNRs (data expressed as percentage of the injected dose (% ID)). Blood samples were collected at 3 min, 10 min, 30 min, 2 h, 5 h and 24 h post administration. Biodistribution of AuNSs and AuNRs in the liver (b), spleen (c), kidney (d), heart (e) and lung (f) at 3 min, 10 min, 30 min and 24 h after systemic administration (**P < 0.01, significant differences between AuNS–chitosan and AuNR–chitosan in 3 min and 10 min of blood circulation. *P < 0.05, significant differences between AuNS–chitosan and AuNR–chitosan in the spleen, kidney, heart and lung).

biodistribution results show that both of gold nanoparticles were mainly captured by reticuloendothelial system and accumulated in the liver and spleen after tail intravenous injection and slightly accumulated in the kidney, heart and lung with low absolute content (Fig. 6b–f). Both AuNSs and AuNRs rapidly accumulated in the liver and spleen at the first 3 min, and then remained stable after 30 min (Fig. 6b and c). There was no significant difference between AuNSs and AuNRs in the liver (Fig. 6b). At the first 3 min, more AuNSs were accumulated in the spleen than AuNRs (Fig. 6c, P < 0.05) in accordance with MSOT results (Fig. 5c and d). Besides, AuNRs had more accumulation in the lung and kidney than AuNSs with significant difference (P < 0.05) which may be attributed to their differences of size and shape (Fig. 6d and f). Although the absolute contents of gold nanoparticles in the heart were very low, there were significant difference (P < 0.05) between AuNSs and AuNRs (Fig. 6e).

It is worth nothing that MSOT provides structural and functional information of only one transverse section of a mouse at one time, while ICP-MS provides quantitative elementary information of all the tissues or organs of a mouse at the same time. Thus it is less convenient for MSOT to provide quantitative information of multiple organs or tissues with statistical analysis than ICP-MS. Besides, the limit detection of MSOT (~3.1 μg mL^{-1} Au) is much higher than ICP-MS (<0.1 ng mL^{-1}).[42] Thus, it is hard to detect the gold nanoparticles in the kidney and heart by MSOT at the 2 mg kg^{-1} injection dose due to their much lower contents compared to the liver and spleen. However, it is a big challenge for the ICP-MS method to collect samples in such a short time to monitor the early pharmacokinetic changes of drugs or probes with very fast

clearance from the bloodstream. ICP-MS also needs to sacrifice animals and requires complicated sample preparation procedures compared to MSOT. Therefore, ICP-MS can be used as the confirmation and supplementary for MSOT, which provides accurate quantitative information with very low detection limit.

Conclusion

Size, shape, surface coating and surface charge are key factors that determine the distribution, translocation, long-term stability and toxicity potential of nanomaterials.[10,43,44] Although many studies had been carried out, the relations between these factors were still complicated, which attracted more detailed investigations. In this article, we had prepared chitosan-capped gold nanoparticles in two different shapes (star and rod) and studied their pharmacokinetics and biodistribution in mice by MSOT. Both AuNSs and AuNRs had accurate and strong signal detections by spectral unmixing function of MOST. The intensity of photoacoustic signals of AuNSs was higher than that of AuNRs at the same OD_{max}. In pharmacokinetic experiments, AuNSs showed longer circulation time in the bloodstream than AuNRs. Both AuNSs and AuNRs experienced rapid clearance in blood-levels followed by a more gradual decrease and had fast and long-time accumulation in the liver and spleen. ICP-MS results verified and supplemented the quantitative results of pharmacokinetic and biodistribution by MSOT, which provides not only the absolute contents of Au element in multiple tissues and organs but also their statistical analysis. The difference between AuNSs and AuNRs was that more AuNSs were accumulated in the spleen than AuNRs at the first 3 min. Besides, AuNRs had more accumulation in the lung and kidney and less accumulation in the heart than AuNSs with significant difference. Although the shape of nanoparticles could affect their *in vivo* biological effects, this study has shown that both gold nanoparticles in star shape and rod shape undergo similar pharmacokinetic and biodistribution pathway (rapid clearance from the bloodstream and major accumulation in the liver and spleen). Therefore, AuNSs, as a novel photothermal platform, appears to be a potent candidate for diverse biomedical applications as AuNRs does. Finally, our experiments also demonstrate that MSOT can serve as an effective and convenient tool to study gold nanoparticles' pharmacokinetic, biodistribution and specific organs' accumulation and metabolism, especially as a rapid screening method for assessing organ-related distribution and acute toxicity of nanomedicines.

Acknowledgements

This work was financially supported by the Ministry of Science and Technology of China (National Basic Research Programs: 2011CB933401 and 2012CB934003), International Science & Technology Cooperation Program of China, Ministry of Science Technology of China (2013DFG32340 and 2014DFG52500), National Major Scientific Instruments Development Project (2011YQ03013406), the National Science Foundation of China (21320102003, 11205166), the National Science Fund for Distinguished Young Scholars (11425520) and State Scholarship Fund of China Scholarship Council (201307970002).

References

1 M. A. McAteer and R. P. Choudhury, *Vasc. Pharmacol.*, 2013, **58**, 31.
2 D. Brambilla, R. Verpillot, B. Le Droumaguet, J. Nicolas, M. Taverna, J. Kona, B. Lettiero, S. H. Hashemi, L. De Kimpe, M. Canovi, M. Gobbi, V. Nicolas, W. Scheper, S. M. Moghimi, I. Tvaroska, P. Couvreur and K. Andrieux, *ACS Nano*, 2012, **6**, 5897.
3 L. Wang, X. Lin, J. Wang, Z. Hu, Y. Ji, S. Hou, Y. Zhao, X. Wu and C. Chen, *Adv. Funct. Mater.*, 2014, **24**, 4229.
4 Y. Xu, J. Wang, X. Li, Y. Liu, L. Dai, X. Wu and C. Chen, *Biomaterials*, 2014, **35**, 4667.
5 Z. Zhang, J. Wang and C. Chen, *Adv. Mater.*, 2013, **25**, 3869.
6 L. G. Xu, Y. Liu, Z. Y. Chen, W. Li, Y. Liu, L. M. Wang, Y. Liu, X. C. Wu, Y. L. Ji, Y. L. Zhao, L. Y. Ma, Y. M. Shao and C. Y. Chen, *Nano Lett.*, 2012, **12**, 2003.
7 G. Wu, A. Mikhailovsky, H. A. Khant and J. A. Zasadzinski, *Methods Enzymol.*, 2009, **464**, 279.
8 K. Cheng, S. R. Kothapalli, H. Liu, A. L. Koh, J. V. Jokerst, H. Jiang, M. Yang, J. Li, J. Levi, J. C. Wu, S. S. Gambhir and Z. Cheng, *J. Am. Chem. Soc.*, 2014, **136**, 3560.
9 Y. Xia, W. Li, C. M. Cobley, J. Chen, X. Xia, Q. Zhang, M. Yang, E. C. Cho and P. K. Brown, *Acc. Chem. Res.*, 2011, **44**, 914.
10 E. Boisselier and D. Astruc, *Chem. Soc. Rev.*, 2009, **38**, 1759.
11 X. Huang, S. Neretina and M. A. El-Sayed, *Adv. Mater.*, 2009, **21**, 4880.
12 Z. Zhang, L. Wang, J. Wang, X. Jiang, X. Li, Z. Hu, Y. Ji, X. Wu and C. Chen, *Adv. Mater.*, 2012, **24**, 1418.
13 Z. Zhang, J. Wang, X. Nie, T. Wen, Y. Ji, X. Wu, Y. Zhao and C. Chen, *J. Am. Chem. Soc.*, 2014, **136**, 7317.
14 L. Wang, Y.-F. Li, L. Zhou, Y. Liu, L. Meng, K. Zhang, X. Wu, L. Zhang, B. Li and C. Chen, *Anal. Bioanal. Chem.*, 2010, **396**, 1105.
15 A. Taruttis, S. Morscher, N. C. Burton, D. Razansky and V. Ntziachristos, *PLoS One*, 2012, **7**, e30941.
16 M. A. Hahn, A. K. Singh, P. Sharma, S. C. Brown and B. M. Moudgil, *Anal. Bioanal. Chem.*, 2011, **399**, 3.
17 J. P. Culver, V. Ntziachristos, M. J. Holboke and A. G. Yodh, *Opt. Lett.*, 2001, **26**, 701.
18 C. Kim, E. C. Cho, J. Chen, K. H. Song, L. Au, C. Favazza, Q. Zhang, C. M. Cobley, F. Gao, Y. Xia and L. V. Wang, *ACS Nano*, 2010, **4**, 4559.
19 S. S. Gambhir, *Nat. Rev. Cancer*, 2002, **2**, 683.
20 D. Kim, S. Park, J. H. Lee, Y. Y. Jeong and S. Jon, *J. Am. Chem. Soc.*, 2007, **129**, 7661.
21 J. Kurhanewicz, D. B. Vigneron, R. G. Males, M. G. Swanson, K. K. Yu and H. Hricak, *Radiol. Clin.*, 2000, **38**, 115.
22 L. V. Wang and S. Hu, *Science*, 2012, **335**, 1458.
23 C. Kim, C. Favazza and L. V. Wang, *Chem. Rev.*, 2010, **110**, 2756.
24 L. Nie, S. Wang, X. Wang, P. Rong, A. Bhirde, Y. Ma, G. Liu, P. Huang, G. Lu and X. Chen, *Small*, 2014, **10**, 1585.

25 W. Li, X. Sun, Y. Wang, G. Niu, X. Chen, Z. Qian and L. Nie, *Biomed. Opt. Express*, 2014, **5**, 2679.
26 Y. Qiu, Y. Liu, L. Wang, L. Xu, R. Bai, Y. Ji, X. Wu, Y. Zhao, Y. Li and C. Chen, *Biomaterials*, 2010, **31**, 7606.
27 L. Wang, Y. Liu, W. Li, X. Jiang, Y. Ji, X. Wu, L. Xu, Y. Qiu, K. Zhao, T. Wei, Y. Li, Y. Zhao and C. Chen, *Nano Lett.*, 2011, **11**, 772.
28 J. Zhang, X. Nie, Y. Ji, Y. Liu, X. Wu, C. Chen and X. Fang, *J. Nanosci. Nanotechnol.*, 2014, **14**, 4124.
29 S. Zhen, F. L. Guo, Y. Li and C. Huang, *Sci. China: Chem.*, 2013, **56**, 387.
30 W. H. De Jong, W. I. Hagens, P. Krystek, M. C. Burger, A. J. A. M. Sips and R. E. Geertsma, *Biomaterials*, 2008, **29**, 1912.
31 W. Jiang, B. Y. S. Kim, J. T. Rutka and W. C. W. Chan, *Nat. Nanotechnol.*, 2008, **3**, 145.
32 Arnida, M. M. Janat-Amsbury, A. Ray, C. M. Peterson and H. Ghandehari, *Eur. J. Pharm. Biopharm.*, 2011, **77**, 417.
33 X. Huang, L. Li, T. Liu, N. Hao, H. Liu, D. Chen and F. Tang, *ACS Nano*, 2011, **5**, 5390.
34 H. Yuan, A. M. Fales and T. Vo-Dinh, *J. Am. Chem. Soc.*, 2012, **134**, 11358.
35 B. Van de Broek, N. Devoogdt, A. D'Hollander, H.-L. Gijs, K. Jans, L. Lagae, S. Muyldermans, G. Maes and G. Borghs, *ACS Nano*, 2011, **5**, 4319.
36 S. Wang, P. Huang, L. Nie, R. Xing, D. Liu, Z. Wang, J. Lin, S. Chen, G. Niu, G. Lu and X. Chen, *Adv. Mater.*, 2013, **25**, 3055.
37 H. Chen, X. Zhang, S. Dai, Y. Ma, S. Cui, S. Achilefu and Y. Gu, *Theranostics*, 2013, **3**, 633.
38 M. L. Tan, P. F. M. Choong and C. R. Dass, *J. Pharm. Pharmacol.*, 2009, **61**, 131.
39 C. Magnetto, M. Prato, A. Khadjavi, G. Giribaldi, I. Fenoglio, J. Jose, G. R. Gulino, F. Cavallo, E. Quaglino, E. Benintende, G. Varetto, A. Troia, R. Cavalli and C. Guiot, *RSC Adv.*, 2014, **4**, 38433.
40 L.-C. Cheng, H. M. Chen, T.-C. Lai, Y.-C. Chan, R.-S. Liu, J. C. Sung, M. Hsiao, C.-H. Chen, L.-J. Her and D. P. Tsai, *Nanoscale*, 2013, **5**, 3931.
41 R. R. Arvizo, O. R. Miranda, D. F. Moyano, C. A. Walden, K. Giri, R. Bhattacharya, J. D. Robertson, V. M. Rotello, J. M. Reid and P. Mukherjee, *PLoS One*, 2011, **6**, e24374.
42 B. Meermann and M. Sperling, *Anal. Bioanal. Chem.*, 2012, **403**, 1501.
43 Z. Zhang, J. Wang and C. Chen, *Theranostics*, 2013, **3**, 223.
44 Y. Liu, Y. Zhao, B. Sun and C. Chen, *Acc. Chem. Res.*, 2013, **46**, 702.

APPENDIX III : Patent 1

UNITED STATES PATENT AND TRADEMARK OFFICE

UNITED STATES DEPARTMENT OF COMMERCE
United States Patent and Trademark Office
Address: COMMISSIONER FOR PATENTS
P.O. Box 1450
Alexandria, Virginia 22313-1450
www.uspto.gov

APPLICATION NUMBER	FILING or 371(c) DATE	GRP ART UNIT	FIL FEE REC'D	ATTY.DOCKET.NO	TOT CLAIMS	IND CLAIMS
15/136,931	04/24/2016	1736	400	WK16-211-XYD-US-211	10	1

CONFIRMATION NO. 1087

126361
Wayne & King LLC
PO Box 439
Painted Post, NY 14870

FILING RECEIPT

Date Mailed: 05/09/2016

Receipt is acknowledged of this non-provisional patent application. The application will be taken up for examination in due course. Applicant will be notified as to the results of the examination. Any correspondence concerning the application must include the following identification information: the U.S. APPLICATION NUMBER, FILING DATE, NAME OF APPLICANT, and TITLE OF INVENTION. Fees transmitted by check or draft are subject to collection. Please verify the accuracy of the data presented on this receipt. **If an error is noted on this Filing Receipt, please submit a written request for a Filing Receipt Correction. Please provide a copy of this Filing Receipt with the changes noted thereon. If you received a "Notice to File Missing Parts" for this application, please submit any corrections to this Filing Receipt with your reply to the Notice. When the USPTO processes the reply to the Notice, the USPTO will generate another Filing Receipt incorporating the requested corrections**

Inventor(s) Yadian Xie, Painted Post, NY;
Duygu Kocaefe, Chicoutimi, CANADA;
Wei Liu, Guiyang, CHINA;
Yasar Kocaefe, Chicoutimi, CANADA;

Applicant(s) University of Quebec at Chicoutimi

Assignment For Published Patent Application
Yadian Xie

Power of Attorney: The patent practitioners associated with Customer Number 126361

Domestic Applications for which benefit is claimed - None.
A proper domestic benefit claim must be provided in an Application Data Sheet in order to constitute a claim for domestic benefit. See 37 CFR 1.76 and 1.78.

Foreign Applications for which priority is claimed (You may be eligible to benefit from the **Patent Prosecution Highway** program at the USPTO. Please see http://www.uspto.gov for more information.) - None.
Foreign application information must be provided in an Application Data Sheet in order to constitute a claim to foreign priority. See 37 CFR 1.55 and 1.76.

Permission to Access Application via Priority Document Exchange: No

Permission to Access Search Results: No

Applicant may provide or rescind an authorization for access using Form PTO/SB/39 or Form PTO/SB/69 as appropriate.

If Required, Foreign Filing License Granted: 05/06/2016

The country code and number of your priority application, to be used for filing abroad under the Paris Convention, is **US 15/136,931**

Projected Publication Date: 10/26/2017

Non-Publication Request: No

Early Publication Request: No
**** MICRO ENTITY ****
Title

Novel Method for Extracting Ultra High Purity Alumina from Wastewater

Preliminary Class

423

Statement under 37 CFR 1.55 or 1.78 for AIA (First Inventor to File) Transition Applications: No

PROTECTING YOUR INVENTION OUTSIDE THE UNITED STATES

Since the rights granted by a U.S. patent extend only throughout the territory of the United States and have no effect in a foreign country, an inventor who wishes patent protection in another country must apply for a patent in a specific country or in regional patent offices. Applicants may wish to consider the filing of an international application under the Patent Cooperation Treaty (PCT). An international (PCT) application generally has the same effect as a regular national patent application in each PCT-member country. The PCT process **simplifies** the filing of patent applications on the same invention in member countries, but **does not result** in a grant of "an international patent" and does not eliminate the need of applicants to file additional documents and fees in countries where patent protection is desired.

Almost every country has its own patent law, and a person desiring a patent in a particular country must make an application for patent in that country in accordance with its particular laws. Since the laws of many countries differ in various respects from the patent law of the United States, applicants are advised to seek guidance from specific foreign countries to ensure that patent rights are not lost prematurely.

Applicants also are advised that in the case of inventions made in the United States, the Director of the USPTO must issue a license before applicants can apply for a patent in a foreign country. The filing of a U.S. patent application serves as a request for a foreign filing license. The application's filing receipt contains further information and guidance as to the status of applicant's license for foreign filing.

Applicants may wish to consult the USPTO booklet, "General Information Concerning Patents" (specifically, the section entitled "Treaties and Foreign Patents") for more information on timeframes and deadlines for filing foreign patent applications. The guide is available either by contacting the USPTO Contact Center at 800-786-9199, or it can be viewed on the USPTO website at http://www.uspto.gov/web/offices/pac/doc/general/index.html.

For information on preventing theft of your intellectual property (patents, trademarks and copyrights), you may wish to consult the U.S. Government website, http://www.stopfakes.gov. Part of a Department of Commerce initiative, this website includes self-help "toolkits" giving innovators guidance on how to protect intellectual property in specific countries such as China, Korea and Mexico. For questions regarding patent enforcement issues, applicants may call the U.S. Government hotline at 1-866-999-HALT (1-866-999-4258).

APPENDIX III : Patent 2

Chinese patent NO.1:

Name: Measurement method of α-alumina trace elements and its digestion solvent

Inventor: Yadian Xie, Duygu Kocaefe, Yasar Kocaefe, Wei Liu

Application NO: 201510323036.8

中华人民共和国国家知识产权局

550001

贵州省贵阳市中华北路 78 号贵银大厦 14 楼 6、7 号
贵阳中新专利商标事务所 刘楠,李余江

发文日：

2015 年 06 月 15 日

申请号或专利号：201510323036.8　　发文序号：2015061500600580

专 利 申 请 受 理 通 知 书

根据专利法第 28 条及其实施细则第 38 条、第 39 条的规定，申请人提出的专利申请已由国家知识产权局受理。现将确定的申请号、申请日、申请人和发明创造名称通知如下：

申请号：201510323036.8

申请日：2015 年 06 月 12 日

申请人：贵州师范大学

发明创造名称：α-氧化铝中微量元素测定方法及其所用的消解剂

经核实，国家知识产权局确认收到文件如下：

发明专利请求书 每份页数:5 页 文件份数:1 份

权利要求书 每份页数:1 页 文件份数:1 份 权利要求项数： 2 项

说明书 每份页数:3 页 文件份数:1 份

说明书摘要 每份页数:1 页 文件份数:1 份

专利代理委托书 每份页数:2 页 文件份数:1 份

费用减缓请求书 每份页数:1 页 文件份数:1 份

费用减缓证明 每份页数:1 页 文件份数:1 份

提示：

1. 申请人收到专利申请受理通知书之后，认为其记载的内容与申请人所提交的相应内容不一致时，可以向国家知识产权局请求更正。

2. 申请人收到专利申请受理通知书之后，再向国家知识产权局办理各种手续时，均应当准确、清晰地写明申请号。

审 查 员：张力(电子申请)　　审查部门：专利局初审及流程管理部 18

200101 2010.2　纸件申请，回函请寄：100088 北京市海淀区蓟门桥西土城路 6 号 国家知识产权局受理处收
电子申请，应当通过电子专利申请系统以电子文件形式提交相关文件。除另有规定外，以纸件等其他形式提交的文件视为未提交。